National Technical University of Athens

School of Chemical Engineering

Doctoral Dissertation

Design and development of an apparatus for microencapsulation of pancreatic cell islets

By

Nikolaos G. Dimitrioglou

Supervisor:

Professor Dimitrios T. Hatziavramidis

January 20, 2020

This research is co-financed by Greece and the European Union (European Social Fund- ESF) through the Operational Programme «Human Resources Development, Education and Lifelong Learning» in the context of the project "Strengthening Human Resources Research Potential via Doctorate Research" (MIS-5000432), implemented by the State Scholarships Foundation (IKY).

“ Όταν μας έρχουνται ανάποδα όλα,

τι χαρά να δοκιμάζουμε την ψυχή μας αν έχει αντοχή κι αξία! ”

Ν. Καζαντζάκης

Στους ανθρώπους μου.

Στους φίλους και στην οικογένεια μου.

Και ιδιαίτερα στον αγαπημένο ανιψιό μου.

Examination Committee

- **Dr. Dimitrios T. Hatziavramidis**, Professor, National Technical University of Athens (NTUA)
- **Dr. Andreas G. Boudouvis**, Professor, NTUA
- **Dr. Constantinos A. Charitidis**, Professor, NTUA
- **Dr. Hamid Arastoopour**, Professor, Illinois Institute of Technology
- **Dr. Dimitrios M. Rekkas**, Associate Professor, National and Kapodistrian University of Athens
- **Dr. Evangelos N. Topakas**, Associate Professor, NTUA
- **Dr. Michail E. Kavousanakis**, Assistant Professor, NTUA

Abstract

Transplantation of encapsulated islets of Langerhans is a therapeutic modality for treatment of Type 1 diabetes mellitus. Conventional microencapsulation technologies fail to prevail, as they produce single-sized microcapsules and attain low efficiencies. Given the fact of polydispersity in islets, a different manipulation is required in every occasion, in order to fabricate microcapsules of proper size efficiently. Efficiency here is defined as the ratio of the number of properly encapsulated islets to the total number of islets fed. By proper encapsulation it is meant one in which the encapsulated islets are viable and functional. In this Dissertation, we propose a novel isletτ microencapsulation apparatus designed by the principles of Mechanics and Cytotechnology. The fundamental idea of our approach is that encapsulation is driven by islet motion and capsule size and shape are determined by the individual islet size and shape, respectively. We focus on two requirements; the accurate separation of loaded islets to encapsulate one islet per capsule and the uniform thickness of the capsule membrane to accommodate the heterogeneous morphology of islets. The first requirement is met by the utilization of hydrodynamic focusing as a feeding system in our device. The second requirement is met by the employment of selective withdrawal as an encapsulation method.

With the intent to shed light to the physical mechanisms occurring in the apparatus, we develop two computation models. The first model simulates the hydrodynamic focusing of islets that are modeled as spherical and elliptical particles. To our knowledge, this is the first time that a numerical model can predict the motion of particles in a hydrodynamic focusing system. This consideration allows us to estimate the trajectory of a particle in order to accomplish the focusing and separation of two or more particles. In addition, the flow generated by selective withdrawal in the encapsulation chamber is numerically simulated. Contrary to previous numerical studies, the model presented here employs a detailed geometry including an inlet and a withdrawal tube. The aim of the study is to identify the effect of design and function parameters on selective withdrawal.

By employing three-dimensional printing technology, an apparatus including a hydraulic pumping system is developed. Despite the rapid expansion of 3D-printing, there is a limited number of reports in the literature demonstrating the potential contribution to encapsulation technology. In our apparatus, spherical particles serving as islet models are encapsulated by employing the hydrodynamics of selective withdrawal. The phenomenon of

the breakthrough of a particle through a dynamic steady-state cusp during is studied. This Dissertation brought us closer to understanding and fulfilling the requirements of an efficient apparatus for islet microencapsulation.

Περίληψη

Η μεταμόσχευση ενθυλακωμένων νησιδίων του Langerhans είναι μία εναλλακτική θεραπεία του σακχαρώδη διαβήτη Τύπου 1. Οι συμβατικές τεχνολογίες μικρο-ενθυλάκωσης παράγουν συγκεκριμένου μεγέθους κάψουλες για νησίδια διαφορετικού μεγέθους και αδυνατούν να επιτύχουν υψηλούς ρυθμούς απόδοσης Η απόδοση ορίζεται ως η αναλογία του αριθμού των κατάλληλα ενθυλακωμένων νησιδίων σε σχέση με τον συνολικό αριθμό τροφοδοτούμενων νησιδίων. Κατάλληλη ενθυλάκωση χαρακτηρίζεται η περίπτωση όπου εξασφαλίζεται η βιωσιμότητα και η λειτουργικότητα των νησιδίων πριν και μετά την μεταμόσχευση. Στη παρούσα Διατριβή προτείνεται μία καινοτόμα συσκευή μικρο-ενθυλάκωσης, σχεδιασμένη σύμφωνα με τις αρχές της Μηχανικής και της Κυτταρομετρίας. Η θεμελιώδης ιδέα της προτεινόμενης τεχνολογίας είναι ότι η ενθυλάκωση προκαλείται από την κίνηση των νησιδίων και το σχήμα και το μέγεθος της κάψουλας καθορίζεται από το σχήμα και το μέγεθος των νησιδίων, αντίστοιχα. Δύο σημαντικές απαιτήσεις για την αποτελεσματική λειτουργία της συσκευής αποτέλεσαν αντικείμενο έρευνας. Η τροφοδοσία κάθε νησιδίου ξεχωριστά και ευθυγραμμισμένα στην περιοχή ενθυλάκωσης και το ομοιόμορφο πάχος της μεμβράνης της κάψουλας που θα προσαρμόζεται στην ετερογενή μορφολογία των νησιδίων. Η πρώτη απαίτηση ικανοποιείται με τη χρήση της υδροδυναμικής εστίασης ως συστήματος τροφοδοσίας. Η δεύτερη απαίτηση ικανοποιείται με την εφαρμογή της επιλεκτικής απόσυρσης ως μεθόδου ενθυλάκωσης.

Αναπτύχθηκαν δύο υπολογιστικά μοντέλα για την κατανόηση των φυσικών φαινομένων εντός της συσκευής. Το πρώτο μοντέλο προσομοιώνει τον υδροδυναμικό εστιασμό των νησιδίων, τα οποία μοντελοποιούνται ως κυκλικά και ελλειπτικά σωματίδια. Η προσέγγιση αυτή επιτρέπει τον επακριβή υπολογισμό των τροχιών των σωματιδίων, την μελέτη αλληλεπιδράσεων μεταξύ σωματιδίων καθώς και τον υπολογισμό των μεταξύ τους αποστάσεων. Στο δεύτερο μοντέλο, προσομοιώνεται αριθμητικά το υδροδυναμικό φαινόμενο της επιλεκτική απόσυρσης σε έναν θάλαμο ενθυλάκωσης. Το προτεινόμενο μοντέλο περιλαμβάνει έναν σωλήνα τροφοδοσίας και ένα σωλήνα απόσυρσης. Σκοπός της είναι η μελέτη και ο προσδιορισμός της επίδρασης των σχεδιαστικών και λειτουργικών παραμέτρων στην επιλεκτική απόσυρση και συγκεκριμένα στο σχήμα της διεπιφάνειας δύο μη αναμίξιμων υγρών. Με τη χρήση της τρισδιάστατης εκτύπωσης αναπτύχθηκε μία συσκευή μικρο-ενθυλάκωσης και ένα υδραυλικό σύστημα για τον έλεγχο των ροών τροφοδοσίας, απόσυρσης και ανακύκλωσης. Πραγματοποιήθηκαν πειράματα με σκοπό την ενθυλάκωση σφαιρικών

σωματιδίων με μεγέθη αντίστοιχα του ανθρώπινου νησιδίου. Συγκεκριμένα, ερευνήθηκε το φαινόμενο της διαπέρασης ενός σωματιδίου από μία διεπιφάνεια δύο υγρών που βρίσκεται σε δυναμικά σταθερή κατάσταση. Τα αποτελέσματα της Διατριβής μας έφεραν ένα βήμα πιο κοντά στην κατανόηση φυσικών φαινομένων σχετικών με την αποτελεσματική λειτουργία μίας συσκευής για μικρο-ενθυλάκωση νησιδίων παγκρεατικών κυττάρων.

Contents

PART II – Computational and Experimental Research

PART III – Conclusions

APPENDICES

Preface

Publications

The results in this Dissertation have been presented in the following publications and conferences:

In peer-reviewed journals

Dimitrioglou, N., Dometios, A., Rekkas, D., & Hatziavramidis, D. (2020). Design strategy and development of a 3D-printed apparatus for particle encapsulation. (*ongoing research*)

Dimitrioglou, N., Mantzanas, A., & Hatziavramidis, D. (2020). Modeling the motion of particles in a hydrodynamic focusing domain. (*to be submitted*)

Dimitrioglou, N., Kanelli, M., Papageorgiou, E., Karatzas, T., & Hatziavramidis, D. (2019). Paving the way for successful islet encapsulation. *Drug Discovery Today*, 23(3), 737-748.

Dimitrioglou, N.G., & Hatziavramidis, D.T. (2018). Numerical investigation of selective withdrawal in a pancreatic cell islet encapsulation apparatus. *Computers & Chemical Engineering*, 119, 293-301.

In conference proceedings

Mantzanas, A., Dimitrioglou, N., & Hatziavramidis, D.T. (September 2019, Rhodes). Modeling the motion of biological particles in a hydrodynamic focusing domain. In American Institute of Physics Conference Proceedings of 17th International Conference of Numerical Analysis and Applied Mathematics (ICNAAM). (*to be published*)

Mantzanas, A., Dimitrioglou, N.G., & Hatziavramidis, D.T. (April 2019, Bahrain). Two-Dimensional Numerical Study of Particle Motion for Continuous Focusing and Separation. In *2019 8th International Conference on Modeling Simulation and Applied Optimization (ICMSAO)* (pp. 1-5). IEEE.

Dimitrioglou, N. G., & Hatziavramidis, D. T. (May 2018, Prague). Numerical Simulation of Selective Withdrawal Pertinent to Efficient Cell Encapsulation. In *World Congress on Medical Physics and Biomedical Engineering 2018* (pp. 547-552). Springer, Singapore.

Dimitrioglou N., Psihogios J., & Hatziavramidis D. (May 2017, Thessaloniki). Hydrodynamic Focusing of Particles in a microfluidic device. In Proceedings of 11th Panhellenic Scientific Conference in Chemical Engineering.

Acknowledgments

The completion of this Dissertation would not have been accomplished without the contribution of the following people.

I would like to express my deepest gratitude to my supervisor, Prof. Dimitris Hatziavramidis for his guidance and wholeheartedly support all these years. I could not have imagined having a better mentor for my PhD study.

I would like to thank Prof. Andreas Boudouvis and Prof. Costas Charitidis, members of the Examination Committee, for our constructive discussions and their valuable advice.

I would like to thank Associate Prof. Dimitris Rekkas from National and Kapodistrian University of Athens for giving me access to the Pharmaceutical Technology Laboratory and its facilities.

I would like to thank Dr John Psyhogios and Dr Nikolaos Chamakos for introducing me to computational analysis at the beginning of my PhD studies. In addition, many thanks to Dr Maria Kanelli for our fruitful collaboration.

Special thanks to PhD student Athanasios Dometios for his invaluable contribution to the development of the apparatus. I also wish to thank PhD students Eleni Tsintavi and Vlasia Aroni and the undergraduate student Alexandros Mantzanas for the excellent collaboration.

The contribution of the administrative staff and the laboratory teaching staff of the School of Chemical Engineering is highly appreciated. Particularly, I would like to thank Dr Lazaros Karaoglanoglou and Dr Dimitris Koullas from the Organic Chemical Technology Laboratory for their assistance.

I kindly acknowledge the funding by the State Scholarships Foundation.

N. Dimitrioglou
January 20, 2020

Nomenclature

Roman letters

a	major particle axis
b	minor particle axis
$D(t)$, D_0, Dx, Dy, $D_{(i, i+1)}$	distance between particles
d_s	spout diameter
$\mathbf{f}$	body force per unit mass
$\mathbf{F}$	hydrodynamic force acting on the particle
$f(r)$	axisymmetric fluid-fluid interface shape
$\mathbf{G}$	body force exerted by external fields
$\mathbf{g}$	gravitational acceleration
g	gravitational constant
h_c	critical height
H_c	distance of the lower tube inlet from the bottom of the container
h_{max}	height of the steady-state disturbed interface
h_{mesh}	mesh size
H_t	tube height
$\mathbf{I_i}$	moment of inertia matrix of the i^{th} particle
k	sample-to-sheath-flow rate ratio
L	channel length in Chapter 2 and chamber radius in Chapter 3
m	mass
N	number of particles
$\mathbf{n}$	unit normal vector
p	pressure
q, Q_j, Qc	flow rate
R	inner tube radius
r, z	cylindrical coordinates
R_f	fillet radius
S	distance of the upper tube outlet from the unperturbed interface
s	initial distance of a particle from a wall
t	time
T	time needed for a particle to reach the outlet
t^*	nondimensional time
T_h	triangular mesh
$\mathbf{u}$	fluid velocity field
$\mathbf{u_{mesh}}$	mesh velocity
$\mathbf{V}$	particle translational velocity
W	channel width
w	wall tube thickness
$\mathbf{X}$	particle centroid

Greek letters

α	aspect ratio
β	blockage ratio
γ	surface tension
$\Delta\rho$	density difference between two fluids

θ	orientation angle
Θ_i	particle orientation
λ	density ratio
μ	fluid viscosity
π	3.141592…
ρ_f	fluid density
σ	total stress tensor in chapter 2
T	total stress tensor in chapter 3
τ	viscous stress tensor
ω	angular particle velocity
Ω	domain

Named dimensionless groups designated with two letters

Bo	Bond number
Ca	Capillary number
Re	Reynolds number

Mathematical operations and special symbols

·	dot product operator
×	vector product operator
k^e	inverse of the local element volume
∇	gradient operator
∇_t	tangential gradient operator
∇^2	Laplacian operator
*	dimensionless quantity
$\mathcal{H}$	mean curvature

Abbreviations

2D	Two-dimensional
3D	Three-dimensional
3DP	Three-dimensional printing
ALE	Arbitrary Lagrangian – Eulerian
BW	Body weight
CAD	Computer-aided design
CSF1R	Colony stimulating factor-1 receptor
DLM	Distributed Lagrange Multiplier
DNS	Direct Numerical Simulation
DOPA	3,4–dihydroxyl– l–phenylalanine
ECM	Extracellular matrix
EFP	Epididymal fat pad

ESC	Embryonic stem cell
FD	Fictitious domain
FDA	Food and Drug Administration
FDM	Fused Deposition Modeling
FE	Finite Element
FFI	Fluid-fluid interface
GIP	Glucose-dependent insulinotropic peptide
GLP-1	Glucagon-like peptide 1
GSIS	Glucose induced insulin secretion
HF	Hydrodynamic focusing
HFM	Hollow fiber membrane
IBMIR	Instant blood-mediated inflammatory reactions
IEQ	Islet Equivalents
INS-1	Rat pancreatic beta cell line
iPSC	Induced pluripotent stem cell
LbL	Layer-by-layer
LBM	Lattice-Boltzmann method
LCT	Living Cell Technologies
LFA-1	Anti-Lymphocyte function-associated antigen 1
MSC	Mesenchymal stem cell
NCT	National clinical trial
NHP	Non-human primate
NHS	N-hydroxysuccinimide
NPCC	Porcine neonatal pancreatic cell cluster
OCR	Oxygen consumption rate
PAN	Polyacrylonitrile
PDMS	Poly(dimethylsiloxane)
PEG	Poly(ethylene glycol)
PEGDA	Poly(ethylene glycol) diacrylate
PEG-MAL	Polyethylene glycol maleimide
PFD	Perfluorodecalin
PLGA	Poly(lactide–co–glycolide)
PS	Polystyrene
PSC	Pluripotent stem cell
PSU	Polysulfone
PTFE	Polytetrafluoroethylene
PVPON/TA	Poly(N-vinylpyrrolidone)/ tannic acid
ROS	Reactive oxygen species
T1DM	Type 1 diabetes mellitus
TGF-b1	Recombinant transforming growth factor-beta 1
TMTD	Triazole-thiomorpholine dioxide
TPCL	Three-phase contact line
VEGF	Vascular endothelial growth factor

PART I

Introduction

Chapter

1 Paving the way for successful islet encapsulation

Synopsis

In this chapter, we firstly summarize the last five years' accomplishments in islet encapsulation technology for treatment of Type 1 diabetes mellitus (T1DM). T1DM is an autoimmune disorder where the immune system decimates pancreatic cell islets that produce insulin. Direct pancreatic islet transplantation cannot serve as a widespread therapeutic modality due to the need for lifelong immunosuppression and donor shortage. Therefore, several encapsulation techniques have been developed in order to enclose the islets in semipermeable vehicles that will allow oxygen and nutrients input as well as insulin, other metabolites and waste output, while also accomplishing immunoisolation at the same time. We propose a microencapsulation islet apparatus aimed at efficiently encapsulating a high number of islets within a reasonable time. Finally, we present the scope of this Dissertation.

1.1 Introduction

1.1.1 The endocrine pancreas

The endocrine and nervous systems allow information to be communicated in the human body through chemical and electrical signals respectively. The endocrine system consists of comparatively small, circumscribed organs called glands and regulates cells and organs using organic substances (hormones). Hormones are mostly released into the blood at low concentrations and travel through the circulation to a remote target tissue where it evokes systemic adjustments by engaging specific responses. Thus, glands are mainly located close to a rich blood supply. Typical glands are the hypothalamus and the pituitary in the brain, the thyroid gland on front of trachea, gonads (ovaries for females and testes for males) and the pancreatic islets in the pancreas.

Pancreas is a glandular organ located in the upper left abdomen and is surrounded by major blood vessels. It has lobules, which are formed by a mixture of ductuli and well-vascularized epithelial cell clusters that reflect the two main functions of the pancreas: digestion and glucose homeostasis. Exocrine cells, which are the big majority of the parenchyma, release a mixture of digestive enzymes (trypsin, amylase, lipase among others) into the duodenum. The remaining 1-2% of the pancreatic mass consists of endocrine cells, which form glands and are called islets of Langerhans (Figure 1.1). Each islet comprises around 50-3000 cells of five types; β-cells, α-cells, δ-cells, ε-cells and pancreatic polypeptide (or F) cells. The most important cell type in regulating glucose metabolism during times of nutrient abundance is the β-cell, which represents about 60% of the total islet population. Insulin stimulation occurs in the event of high plasma glucose, glucagon, parasympathetic stimulation, glucagon-like peptide 1 (GLP-1), glucose-dependent insulinotropic peptide (GIP) and other peptides secretion [1].

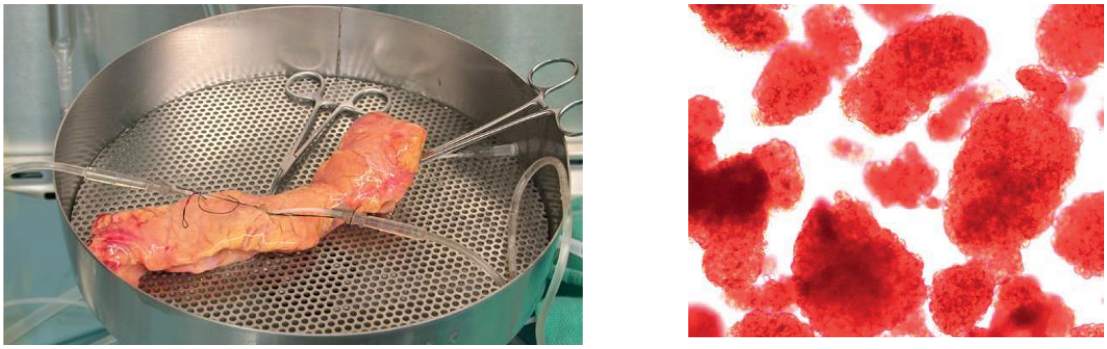

Figure 1.1 Pancreas and Islets of Langerhans. Reprinted from [2].

1.1.2 Pathogenesis of Type 1 diabetes mellitus

Due to certain factors, in one class of people no insulin is produced. In this event, a malady called type 1 diabetes mellitus (T1DM) occurs, and patients who develop the condition are called insulin dependent. T1DM mainly results from complete autoimmune destruction of endocrine pancreatic β-cells. Destruction of β-cells precedes the onset of symptoms by several months or years when the patients are asymptomatic and euglycemic but show positively the presence of relevant antibodies. In this regard, diabetes occurs after a long latency period, correlated with the high percentage of β-cells, which must be destroyed in order to manifest the disease.

The etiology of T1DM's pathogenesis is not yet fully established. More than 50 genetic regions have been identified that impact the risk of developing T1DM [3]. The main genes predisposing of T1DM are within two regions: the major histocompatibility complex (40-60%) and the insulin gene promoter (10%) [4]. Although, genetic predisposing seems to be related to T1DM, the disease is polygenic and there is evidence that it can be triggered due to exposure of genetically susceptible individuals to environmental factors [4]. Environmental factors include viruses, such as rubella and enteroviruses, diet (nutrients and toxins), as well as gut microbiota.

1.1.3 Current approaches for treatment

T1DM is heretofore an incurable disease and thus requires life-long treatment. Currently, the main treatment is insulin replacement therapy where insulin is exogenously administrated via subcutaneous injections or by insulin pumps. However, lifelong dependency on exogenous insulin is a treatment that has serious disadvantages including severe episodes of hypoglycemia, mild obesity, and psychiatric conditions [5]. Recently, close-loop systems (also known as artificial pancreas) have been developed adjusting the insulin secretion by continuously monitoring glucose concentration. However, serious concerns have been raised as tissue scars due to repeated micro-needle insertion and premature sensor failure occurs [5].

Islet transplantation with immunosuppression, known as Edmonton protocol, has been proposed as a therapeutic modality for T1DM treatment. Transplanting pancreatic islets has important advantages over transplanting the whole organ, as the former involves a minor surgical procedure with low morbidity and mortality. In clinical islet transplantation, the required amount of Islet Equivalents (IEQ), i.e., islets with mass equal to that of an islet of average size, 150 μm, is associated with the recipient's body weight (BW). Most clinical protocols determine the lower threshold for human islet transplantation as 5,000 IEQ/kg BW, while trials with larger cohorts of patients raise the number up to 10,000 IEQ/kg BW [6]. In allotransplantation there is a limited supply of human pancreata, however, recent progress in the stem cell field can potentially eliminate this donor shortage barrier [7].

Immunoisolation is proposed for obviation of immunosuppressive drugs that are associated with recurrent side effects. Islets are encapsulated in a barrier vehicle, which protects the islets against host immune responses, while simultaneously facilitates the exchange of vital molecules, such as oxygen, nutrients and insulin. The material needs to be biocompatible, yet not biodegradable, to facilitate neovascularization and exchange of vital molecules, and to prevent invasion of toxic chemical and cellular moieties (antibodies, cytokines, etc.).

1.2 Islet encapsulation strategies

Strategies for the encapsulation of pancreatic islets can be categorized into three main categories: (i) nanoencapsulation, (ii) microencapsulation (iii) macroencapsulation (Figure 1.2 i-ii). This classification is based on the mean distance of the islets from the host environment, as the most significant parameter of cell viability and function.

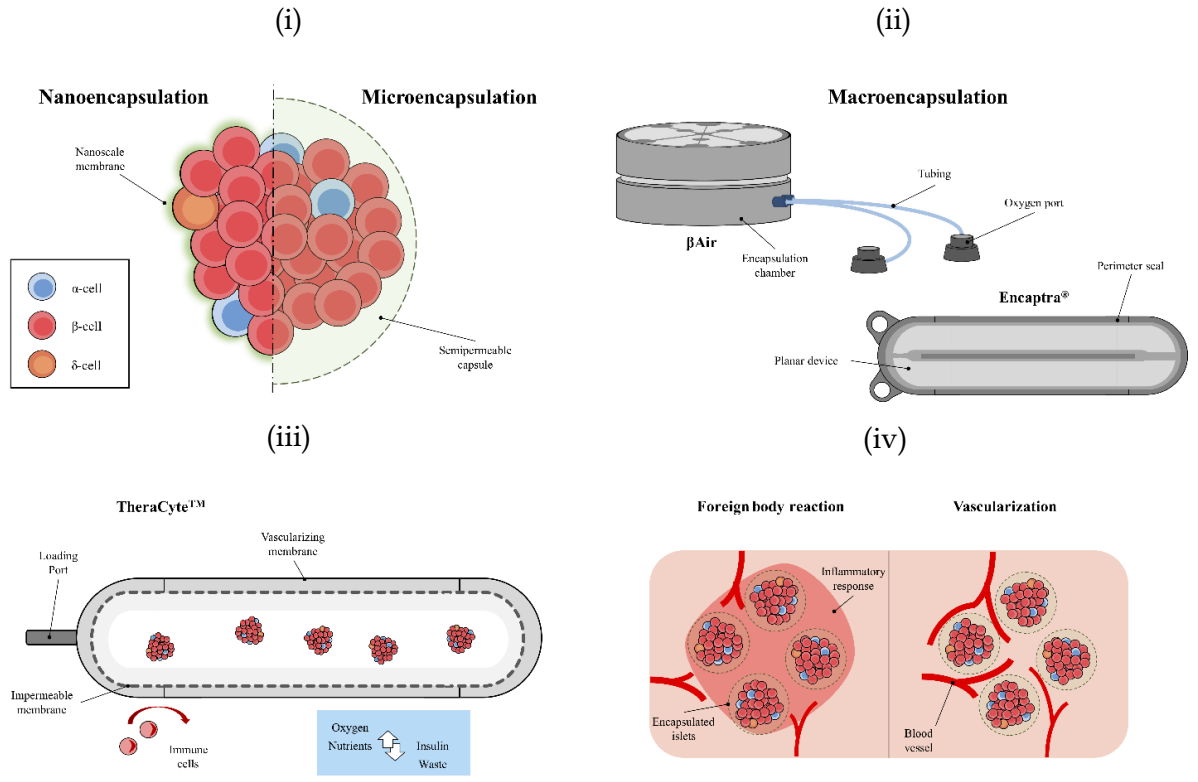

Figure 1.2 Schematic illustration of pancreatic islet encapsulation. (i) Nanoencapsulation and microencapsulation of an islet. (ii) Macroencapsulation devices house a large mass of islets. Encaptra1 is a planar device containing a semipermeable barrier, whereas bAir is a device with ports for recharging oxygen. (iii) Immunosuppression using TheraCyteTM, a thin biocompatible membrane-bound polymeric chamber. (iv) Shortly after the transplantation a host response occurs. Over time, a vascular network forms providing the supply of oxygen and nutrients for the encapsulated islets.

1.2.1 Nanoencapsulation

Layer-by-layer (LbL) deposition of oppositely charged biomaterials is the most used method for islet nanoencapsulation. Nanoscale LbL coatings were developed expressing bio-orthogonal functionality and tailored physicochemical properties. A recent study established an encapsulation method based on LbL assembly that facilitates the cell surface to be coated by extracellular matrix. This technique enabled the rapid fabrication of well-structured beta cell spheroids, enhancing intracellular interaction, and its effectiveness was tested in a mice model [8]. A xenotransplantation of LbL non-human primate (NHP) islets was conducted by Haque et al [9] to test a three polymer LbL encapsulation of NHP islets in mice with immunosuppression. They claimed that the LbL encapsulation showed a uniform nano-shielding on islets without the loss of viability and function. Recently, Park and coworkers [10] transplanted heparin nano-shielded islets (10-20000 IEQ/kg BW) into NHP with immunosuppressive drugs that reduced instant blood-mediated inflammatory reactions (IBMIR). Additionally, an ultrathin heparin-polymer nanofilm was proposed by another group, which provides an open platform which enables incorporation of biological mediators for islet surface bioengineering [11].

1.2.2 Microencapsulation

The microencapsulation approach indicates the encapsulation of individual or small clusters of islets. Microcapsules are the most common microencapsulation vehicles and have been broadly investigated and tested in several animal models. Ma and coworkers [12] encapsulated cells in alginate-based hydrogel microcapsules with core-shell structures using a two-fluid coaxial electro-jetting that provided better treatment than conventional capsules in a mouse model. Furthermore, Teramura and coworkers [13] proposed a microencapsulation method within an ultra-thin polymer membrane (~10 μm) that is thicker than conventional LbL membranes and thus more stable. Tomei and coworkers developed a strategy to minimize the distance from islet to the host tissue by exploiting an optimized hydrodynamic focusing technique [14]. The so-called conformal coating allows complete microencapsulation with a thin layer (10-50 μm) of hydrogel that secures islet function in a rodent model. The same group later produced polyethylene glycol-maleimide matrigel (islet-

like extracellular matrix) that encapsulated islets via conformal coating and presented long term survival after allotransplantation in the epididymal fat pad (EFP) site (750-1000 IEQ / mouse) in the absence of immunosuppression, while no T cell activation was observed [15]. Furthermore, an encapsulation platform based on pancreatic extracellular matrix (ECM) was developed by Chaimov and coworkers [16] and was assessed in a proof-of-concept study using a mouse model. Specifically, ECM-encapsulated cells were shown to be non-immunogenic and the glycemic control was improved.

1.2.3 Macroencapsulation

The main distinction of macroencapsulation devices is the housing of a large mass of islets. Depending on the transplantation site, macrodevices can be divided into two categories: extravascular and intravascular. The encapsulation devices are transplanted extra-hepatically, however, in this case the rapid angiogenesis is of crucial importance for graft survival. Subcutaneous transplantation facilitates the graft retrieval and monitoring [17], [18]. Extravascular macrocapsules, due to lower surface to volume ratio compared to microcapsules, need more space and transplantation site with established vascular beds. Therefore, such devices are often placed in the peritoneal cavity from which the device can later be explanted/retrieved.

Macroencapsulation devices have already been commercialized, such as Theracyte™, βAir of Beta-O2 Technologies, Ltd. and Encaptra® of ViaCyte. The βAir device consists of three major compartments: (1) an islet compartment with islets embedded in a 500-600 μm thick alginate slab (2) a gas chamber pO2 with inlet and outlet ports and (3) a 25 μm polytetrafluoroethylene (PTFE) membrane segregating the islet module from the host tissue. A newly successful and safe xenotransplantation of porcine islets in a diabetic NHP without immunosuppression has been accomplished with favorable results [19]. Moreover, Evron and coworkers [20] recently determined a supraphysiological level of the gas chamber pO2 in order to substantially increase islet surface density. Another macrnoencapsulated system, the TheraCyte™, device, is a thin biocompatible membrane-bound polymeric chamber that has been tested in many animal studies preventing hyperglycemia [21] and allograft rejection [22]. Encaptra is a planar macroencapsulation device containing a semipermeable barrier that can be engineered properly and loaded with hESCs [23]. A newly published study determines the

biologic characteristics at which this combination product, named VC-01, establishes metabolic control in mice models [24].

1.3 New pathways to successful encapsulation

1.3.1 Material design considerations

The material used for encapsulation of islets or drugs could cause a host fibrotic response resulting in impaired mass transport inwards and outwards through the semipermeable membrane. Therefore, the choice of the material is of great importance in order to modulate the host response and avoid graft rejection. This material should meet certain criteria such as biocompatibility, immunoisolation and semipermeability for nutrients and secreted metabolites or drug exchange. In general, natural polymers are preferred due to the mild, non-destructive to mammalian cells conditions of gelling, with alginate as the most predominantly used due to its production at neutral pH and mild temperatures [25], [26]. Nevertheless, the batch to batch variability and composition divergence of β-D-mannuronic to α-L-guluronic acid ratio as well as the residual components that the natural polymer may contain, such as endotoxins, polyphenols or proteins [27], elicit the host immune response and, thus compromising the islet viability. Furthermore, the cross-linking ions and the presence or absence of additional polymer coating layers influences the success of cell encapsulation [25]. The increase of the guluronic acid to mannuronic acid ratio resulted in more stable and biocompatible alginate structures as pointed in the literature [28]. Alginate hydrogels prepared via ion crosslinking, such as Ca^{+2}, present chemical instability after long-term application because of ion exchange between the divalent crosslinking ions and the monovalent ions, such as Na^{+} existing in the surrounding environment. Somo and coworkers fabricated microbeads from methacrylated alginate which enabled covalent crosslinking under exposure to ultraviolet light in addition to ionic interactions with divalent cations. Methacrylated alginate microbeads presented stability after 1 and 3 weeks in inflammatory response tests performed *in vivo,* using an omentum pouch model [26]. An alternative crosslinking procedure through "click" chemistry has been also proposed [29]. Alginate was functionalized to obtain pendant alkyne or azide functional groups, and subsequently "click" gel capsules were formed with superior stability in ionic media and enhanced permeability to

small size diffusates. Another group introduced tetrazine and norbornene groups to alginate backbone. They proceeded to "click" cross-linking, resulting in more stable structures that provided higher cell viability after encapsulation and minimal inflammatory response, after implantation in mice, in comparison to ionically cross-linked gels. These gels lost structural integrity and were infiltrated by fibroblasts and immune cells in a one-month study [30].

In addition, combining alginate with other natural or synthetic materials has been studied for improved performance. Chitosan-coated alginate capsules were utilized for xenotransplantation of porcine islets in mice demonstrating a trend for graft survival with decreased pericapsular fibrosis. The capsules were also utilized for allotransplantation of canine islets in beagles and normoglycemia was maintained for 1 year [31]. Encapsulation of porcine islets was achieved in alginate capsules coated with methacrylated glycol chitosan via photo-polymerization [32]. Silk macrocapsules combined with alginate or agarose have also been synthesized, with promising results of glucose induced insulin secretion (GSIS) and immunomodulation, when tested *in vitro* [33]. Other natural materials that have been tested recently for cell encapsulation are ursodeoxycholic acid, agarose and hyaluronic acid/collagen [41,42].

Over the years many researchers have focused on the use of synthetic polymers with reactive end groups that facilitate cross-linked configurations in mild conditions or combination of natural and synthetic materials, in order to avoid natural polymer limitations [34]. Poly(ethylene glycol) (PEG) is a synthetic polymer which can be functionalized with groups such as acrylates and methacrylates, enabling the formation of crosslinked bioinert hydrogel networks [34]. Marchioli and coworkers [35] suggested islet encapsulation with a non-adhesive layer of PEG diacrylate (PEGDA). The authors described the synthesis of a bi-layer with the combination of PEGDA with a second hydrogel based on thiolated-gelatin, thiolated-heparin and thiolated-hyaluronic acid that provided cues for endothelial cell adhesion. Alternatively, the same group supported the conformal coating of the islets with PEGDA and subsequent embedding in the pre-mentioned vascularization layer which is composed of thiolated glycosaminoglycans. This stable structure facilitates blood vessel ingrowth and maintains the round shape and functionality of the islets [35].

The conformal coating of islets has been shown to be an efficient strategy for islet immunoisolation, when the total size and volume of the encapsulation device is reduced [36]. In the literature a light-mediated interfacial thiol-norbornene photopolymerization procedure was developed for creating hydrogel conformal coating on pancreatic islets with controlled

coating thickness [37]. The LbL nano-coating of NHP islets with three layers of PEG (SH-6-arm-PEG-NHS, 6-arm-PEG-catechol and linear PEG-SH), combined with an immunosuppressive drug protocol is described, achieving successful xenograft survival for 150 days [9]. In another case, LbL coating of PAMAM-MDT/alginate-hN3 was applied onto alginate microbeads resulting in stable structures. Their permselectivity could be regulated by the charge density of PAMAM, the number of layers and the length of the functional end groups [38].

1.3.2 Ensuring cell supply

The limited donor availability renders human pancreatic cell supply scarce since usually more than two and a half human donors are required for a successful single transplantation. Thus, the search for cell replacement strategies is of primary importance. Over the years allogeneic and xenogeneic cells have been successfully encapsulated and transplanted into rodents, dogs, NHP and humans. Stem cell therapy of T1D represents a promising alternative strategy since stem cells have significant properties such as the ability to differentiate into glucose-responsive insulin-producing cells, along with their regenerative and immunomodulatory capacity. A variety of stem cells has been described in the literature for host normoglycemia restoration, including mesenchymal stem cells (MSCs), pluripotent stem cells (PSCs), including both embryonic stem cells (ESCs) and induced pluripotent stem cells (iPSCs).

MSCs present several advantages such as abundance and easy isolation from various tissues, including adipose tissue, bone marrow, menstrual blood, umbilical cord and dental pulp [39], [40]. In the past, bone marrow–derived MSCs differentiated into islet-like insulin-producing aggregates were encapsulated in a NanoGland device. Cells maintained viability and function for at least 4 weeks with steady insulin production *in vitro*, justifying the potential of this cell source for diabetes therapy [41]. Recently, MSC islet allografts where PEGylated using N-hydroxysuccinimide (NHS)- PEG-CH_3. The NHS group facilitated reactivity to free amines, while the methyl group provided an inert terminal end. Subsequently the islets were allotransplanted in mice and a synergistic relation was evaluated with the anti-Lymphocyte function-associated antigen 1 (LFA-1) antibody which was selected as a transient. Systemic immune monotherapy resulted in long term euglycemia [42]. Research on MSCs is thoroughly described in a review of Dang and coworkers [43].

Human ESCs can regenerate and differentiate into insulin-producing cells when cultured in the appropriate microenvironment. Encapsulation of ESCs has been studied extensively in the literature. Vegas and coworkers reported the first long term glycemic correction in diabetic, immune-competent mice, after encapsulation of hESC-β cells in triazole-thiomorpholine dioxide (TMTD) alginate and intraperitoneal implantation, without any immunosuppression. The encapsulated cells were removed after 174 days [44]. Kirk and coworkers [18] proceeded with the encapsulation of islet progenitors derived from CyT49 hESC in a PTFE bilaminar device (TheraCyte™) and proved immunoisolation in rodents for up to 150 days, until termination. Sufficient insulin levels were achieved by a 20 weeks post-transplant. There was no evidence of cell escape and during insulin secretion increase biomass remained constant.

Apart from the studies, there are ethical concerns relating to use of human embryos for generation of ESCs. iPSCs from somatic cells may be considered an appropriate source for large β-cells generation from a nonembryonic source [45]. Nevertheless, PSCs impose the possible threat of tumor formation and the need for differentiated cell purification is still an issue [46]. Overall, stem cells have proved to be a most promising cell source that could contribute to diabetes treatment. However, further studies must be performed in order to achieve sufficient β-cell production with large scale of cell differentiation, hoping that can be applied at the clinical level and become a functional improvement of such systems via encapsulation.

Xenotransplantation of porcine islets has been an attractive approach due to the close homology between porcine and human insulin and the similarities of the islets from the two species. Thus, porcine lines free of infectious porcine endogenous retrovirus have been identified. In the literature, the coencapsulation of pig islets with adipose or bone marrow MSCs has proven to improve implant oxygenation and neoangiogenesis, nonetheless, it does not seem to ameliorate the long-term function of the BAP in a primate model post subcutaneous implantation [47]. More recently, Teotia and coworkers [48] engineered a PSU/TPGS composite hollow fiber membrane (HFM) BAP and examined the xenotransplantation of encapsulated porcine islets and cell clusters derived from MSCs isolated from human umbilical cord Wharton's jelly. Normoglycemia was achieved for 30 days, while immune response was avoided [58]. Further studies should be conducted to ensure long term behavior of this system.

Adult acinar and duct cells from the exocrine pancreas have been investigated as for their reprogramming to β-cells [49], [50]. Gastrointestinal cells can also be reprogrammed into insulin-producing β-cells through expression or deletion of some transcription factors, such as FOXO1 inhibition [51]. It is noteworthy that cells from the gastrointestinal epithelium have a propensity for conversion into insulin-secreting cells. However, the encapsulation of such cells *in vitro* or *in vivo* has not yet been tested [52]. Advances in cell sources for generation of insulin-producing cells are extensively described in a retrospective work [53]. Although there are encouraging studies in literature, in terms of clinical application more research must be performed since reproducibility is an issue as no standard protocols have been designed [54]. Further study in the future may result in a new perspective in diabetes treatment with the aid of gene editing technologies.

1.3.3 Oxygenation until angiogenesis

Pancreatic β-cells consume a large amount of oxygen during GSIS, because of the high demand of mitochondrial respiration [55]. Nutrient and oxygen ingress to encapsulated islets is facilitated by capillary ingrowth within the capsule [35]. During the early post-transplantation period, oxygen feed takes place only via diffusion until neo-vascularization of the graft. Therefore, islet hypoxia may occur, inhibiting insulin secretion and leading to cell apoptosis. Several strategies have been investigated in order to prevent hypoxia damage.

The use of certain compounds, such as exendin-4, which can attenuate the hypoxia outcome, has been pursued. For instance, it has been demonstrated before that exendin-4 protects β-cells from oxidative stress, enhances GSIS and improves the survival of porcine or mouse islet grafts in mice, while it stimulates insulin release in hypoxic islets [56]. Subsequently, the co-encapsulation of porcine islets with exenatide-loaded poly(lactide–co–glycolide) (PLGA) microspheres in alginate microcapsules was studied and found to accomplish enhanced islet viability and GSIS function *in vitro* [57]. In addition, the vascular endothelial growth factor (VEGF) in encapsulation systems of polyethylene glycol maleimide (PEG–MAL) has been proven to augment vascularization [58]. Marchioli and coworkers [59] constructed a scaffold consisting of an alginate-islets core, surrounded by a PCL-heparinized ring. Heparin, which enabled VEGF binding and increased angiogenesis on and near the scaffold surface *in vitro* [59].

Furthermore, hypoxia and cell necrosis can be avoided with the use of oxygen affinity carriers. Perfluorocarbons are widely used for oxygen boost because of their high oxygen solubility [60]. Lee and coworkers [61] performed integration of perfluorodecalin (PFD) in alginate microcapsules and managed to ameliorate islet function and survival *in vitro* and *in vivo* by minimizing the hypoxic damage of mice islets transplanted intraperitoneally in mice. HIF-1α, which can induce cell apoptosis, was not observed in the nuclei of the PFD-alginate capsules as opposed to non-encapsulated islets and alginate groups, when exposed to hypoxia. The PFD-alginate capsules also demonstrated higher levels of GSIS under the hypoxic state. A hemoglobin, HEMOXCell®, has been verified to increase the cell viability and decrease hypoxia marker, when tested in BAP *in vitro* [62]. The fabrication of an oxygen-generating scaffold by mixing calcium peroxide (CaO_2) with poly(dimethylsiloxane) (PDMS) was performed and tested with porcine neonatal pancreatic cell clusters (NPCCs) *in vitro* where overall viability was improved. Encapsulated NPCCs showed lower caspase-3 and caspase-7 activity, hypoxic cell expression, reactive oxygen species (ROS) levels and higher oxygen consumption rate (OCR) and GSIS [72]. Recently, manganese oxide (MnO) nanoparticles have been examined for their cytoprotective and oxygen generating properties, with potential use in cell therapies [63].

1.3.4 Modulation of immune response

The transplantation of encapsulated islets may evoke the host immune response by releasing cytokines, chemokines, macrophages, free radicals and nitric oxide, which can, ultimately, redound to graft failure [64]. In T1D patients pro-inflammatory M1 macrophages are activated leading to the secretion of chemokines, such as CXCL10 and CCL5, while the synthesis of cytokines such as TNF-α, IL-1β, Type I interferons, and cell surface co-stimulatory molecules such as CD40 and CD80 is promoted. These components attack the sites of transplanted islets in diabetic patients provoking pancreatic β-cell necrosis [65]–[67]. Apart from that, fibrotic overgrowth around the microcapsule surface, because of foreign body response, hinders mass transfer and induces hypoxia.

The presence of cytokines and chemokines in encapsulation systems triggers a strong host immune response. Liu and co-workers investigated localized release of recombinant transforming growth factor-beta 1 (TGF-b1) from poly-lactide-co-glycolide (PLG) layered

scaffolds. TGF-b1 delivery dampened the expression of cytokines TNF-a, IL-12, and MCP-1 and the infiltration of leukocytes [80]. In addition, incorporated chemokine CXCL12 in alginate microcapsules ameliorated allo- and xeno-graft survival in murine specimen, by regulatory T cell (Tregs) recruitment that promote immunosuppression [68]. Pham and coworkers [69] suggested the localized release of an immunosuppressant around the xenograft field. FK506–loaded PLGA–PEG nanoparticles, conjugated with 3,4–dihydroxyl– l–phenylalanine (DOPA), formed a multi-layer nanocoating-camouflage around pancreatic islets from rats. The islets were xenotransplanted in diabetic mice and their survival time increased by 1.7-fold. FK506 seemed to hinder T cell activation and the production of cytotoxic cytokine IL–2 [69].

ECM components are reported to support islet function in alginate microcapsules. LLacua and coworkers [70] have reported that the entrapment of collagen type VI in alginate for microencapsulation of human islets improved cell viability and oxygen consumption without influencing the GSIS, in tests conducted in vitro. It has been previously stated that oxidative stress can contribute to an autoimmune response at an islet transplantation site [71]. It is also demonstrated that poly(N-vinylpyrrolidone)/ tannic acid (PVPON/TA) nanothin coatings can significantly decrease *in vitro* chemokine synthesis and T cell migration, while (PVPON/TA)-encapsulated islets restored euglycemia after transplantation into diabetic mice [71].

Furthermore, the encapsulation material itself as well as the shape, the porosity and the dimensions of the microcapsules play a predominant role in the graft survival [36], [72]. For instance, a foreign body response can cause pericapsular fibrosis in microencapsulation systems due to material impurities as in the case of alginate [73]. However, even clinical-grade commercially purified alginate has been reported to cause foreign body response. Doloff and co-workers [91] evaded macrophage-dependent biomaterial fibrosis by targeting colony stimulating factor-1 receptor (CSF1R), utilizing the ATP-competitive inhibitor GW2580, when alginate, ceramic glass and PS spheres of 500 μm were tested in mice.

1.4 Transition to clinical practice

Although full clinical translation of encapsulation strategy is not yet accomplished, a substantial number of clinical trials of encapsulated islet transplantation with auspicious results have been conducted. Currently, five clinical trials have successfully been completed, and seven are active or at the stage of recruiting. Over 1500 procedures have already been performed worldwide in forty international centers, whereas 864 were allogeneic and 480 were autologous [2]. Encapsulation material and design, as well as implantation sites, are the key aspects of clinical trials. However, none of the published results have been associated with clear evidence of fully function of any encapsulation strategy. Specifically, the attained normoglycemia was accomplished only in few cases, yet at an insufficient level.

In 2014, Uppsala University Hospital in collaboration with Beta-O2 Technologies Ltd. started an open label pilot investigation to assess the safety of Beta-Air and investigate the glycemic control in four patients (NCT02064309). One to two βAir devices, each containing 1800-4600 IEQ per kg of BW, were transplanted and monitored for three to six months [74]. However, although beta cells survived, their function was limited as only minute levels of circulating C-peptide were observed with no impact on metabolic control. An ongoing trial in the University of Miami investigates the allogeneic islet cells transplantation onto the omentum (NCT02213003). Islets are resuspended in autologous plasma and laparoscopically distributed on the omental surface. The omentum is a potential transplant site, as it has dense vascularized surface and is easily accessible. Moreover, clinical-grade recombinant human thrombin is used for cell adherence. Initial results on a 43-year-old female patient were recently reported by Rodolfo Alejandro's group indicating restored euclycemia and insulin independence [75]. Despite a functional decline in twelve months, the subject continued to have stable glycemic control. Although the trial occurred with constant immunosuppression, success with the transplantation at this extrahepatic site can lead to superior functional and clinical outcomes for encapsulated islet transplantation.

1.5 The scope of this Dissertation

Currently, basic and clinical research focuses on encapsulation material, transplantation site and methods to improve immune modulation and neovascularization. Despite important advances mentioned in this Chapter, encapsulation technology continues to face significant obstacles for full clinical implementation. Conventional microencapsulation technologies fail to prevail, as they produce single-sized microcapsules and attain low efficiencies. Given the fact of polydispersity in islets, different manipulation is required in every occasion, in order to attain microcapsules of proper size. Efficiency here is defined as the ratio of the number of properly encapsulated islets to the total number of islets fed. By proper encapsulation it is meant one in which the encapsulated islets are viable and functional. In order to accomplish this goal, a uniform coating of thickness from 10 to 50 μm is required. With the intent to contribute to eliminating some of the challenges, we propose an islet microencapsulation apparatus designed by the principles of Mechanics and Cytotechnology. The fundamental idea of our approach is that encapsulation occurs due to islet motion and capsule size and shape are determined by the individual islet size and shape, respectively.

The conceptual design of the apparatus is presented in Chapter 2 by introducing its functional parts. It consists of a feeder, an encapsulation chamber, a photopolymerization section and a sorting system. In this Dissertation, we focus specifically on two parts of the apparatus; the feeding system and the encapsulation chamber. The feeder utilizes hydrodynamic focusing which separates, aligns in a single file and directs the individual islets to the encapsulation site. Selective withdrawal is proposed as the microencapsulation method. In Chapter 3 and 4, the hydrodynamics relevant to these phenomena are studied through computational fluid mechanics simulations. In Chapter 3, we develop a computational model to simulate the motion of islets in a hydrodynamic focusing configuration. Islets are modeled as spherical and elliptical particles in order to study the dependence of their motion on their morphology. To our knowledge, this is the first study of hydrodynamic focusing where the flow is considered as a liquid-solid flow. This consideration allows us to estimate the trajectory of a particle in order to accomplish the focusing and separation of two or more particles. In Chapter 4, the flow generated by selective withdrawal in the encapsulation chamber is numerically simulated. Contrary to previous numerical studies, the model presented here employs a detailed geometry including an inlet and a withdrawal tube. The

aim of the study is to identify the effect of design and function parameters on selective withdrawal. The results derived from the two computational studies can shed light to the physical mechanisms occurring in the apparatus and lead to optimal design. In Chapter 5, we report the development of an apparatus including a hydraulic pumping system by employing three-dimensional (3D)-printing technology. Despite the rapid expansion of 3D-printing, there is a limited number of reports in the literature demonstrating the potential contribution to encapsulation technology. By operating the 3D-printed apparatus, we experimentally investigate the encapsulation of spherical beads serving as islet surrogates.

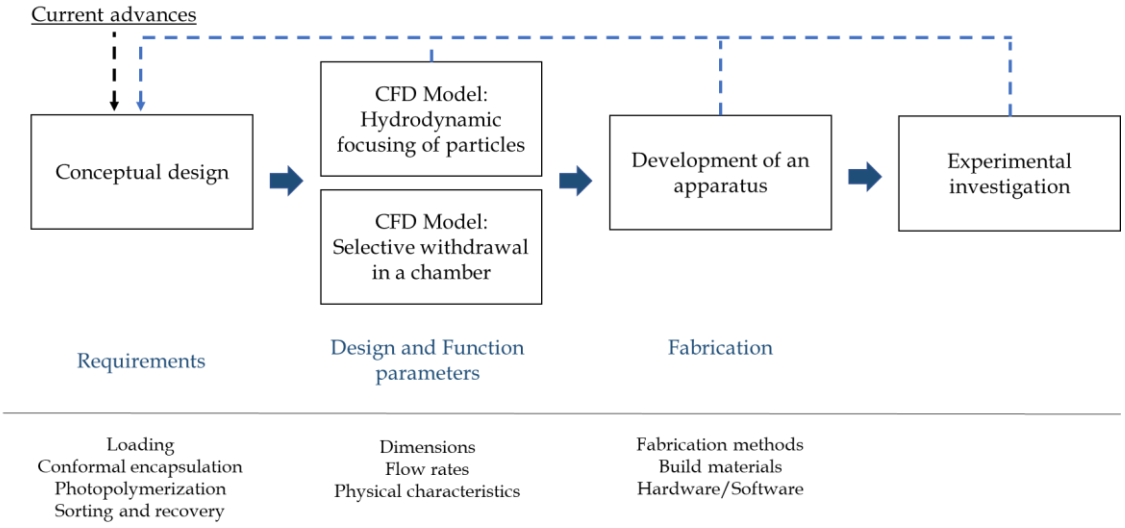

Figure 1.3 Flow chart of the proposed research.

Chapter

2 Designing a microencapsulation islet apparatus

Synopsis

In this Chapter, we present a microencapsulation islet apparatus designed by the principles of Mechanics and Cytotechnology. We initially explain the conceptual design of the apparatus by introducing the functional parts of the apparatus. The utilization of hydrodynamic focusing and selective withdrawal is proposed as a feeding system and a microencapsulation method, respectively.

2.1 Conceptual design of a microencapsulation islet apparatus

Stochastic loading and islet separation, processing stress reduction, efficient polymerization and high yields and rates of single-islet encapsulation are issues that need to be addressed. A microencapsulation islet apparatus was recently designed aiming at efficiently encapsulating a large number of islets within a reasonable time [76]. The apparatus is depicted in Figure 2.1 The functional parts of the apparatus. (i) a hydrodynamic focusing feeder, which aligns the islets in a single file to the withdrawal tube; (ii) an encapsulation chamber where the islets are coated by a solution of PEG-DA; (iii) a coiled tube for photopolymerization where the polymer is crosslinked to form a conformal semipermeable membrane; and (iv) a sorting system, where the islets are isolated and recovered. The apparatus is designed to address the challenges arising from high requirements to achieve insulin independence (5-10,000 IEQ/kg BW) and shortage in islet supply. The main advantages of the proposed technology are the accurate separation of loaded islets to encapsulate one islet per capsule, the uniform thickness of the capsule membrane to accommodate the heterogeneous morphology of islets, and the controlled polymerization to produce a semipermeable membrane that ensures islet viability and function. Lastly, the components of the apparatus can be produced using 3-D printing technology in a time efficient manner.

Designed by the principles of Mechanics and Cytotechnology, the apparatus is depicted in Figure 2.1 and consists of the following four parts:

a. a feeder with hydrodynamic focusing, which aligns the islets in a single file to the withdrawal tube,
b. an encapsulation chamber, where the islets are coated by a polymeric solution,
c. a coiled tube for photopolymerization, where the polymer is crosslinked to form a conformal semipermeable membrane; and
d. a sorting system, where the islets are isolated and recovered.

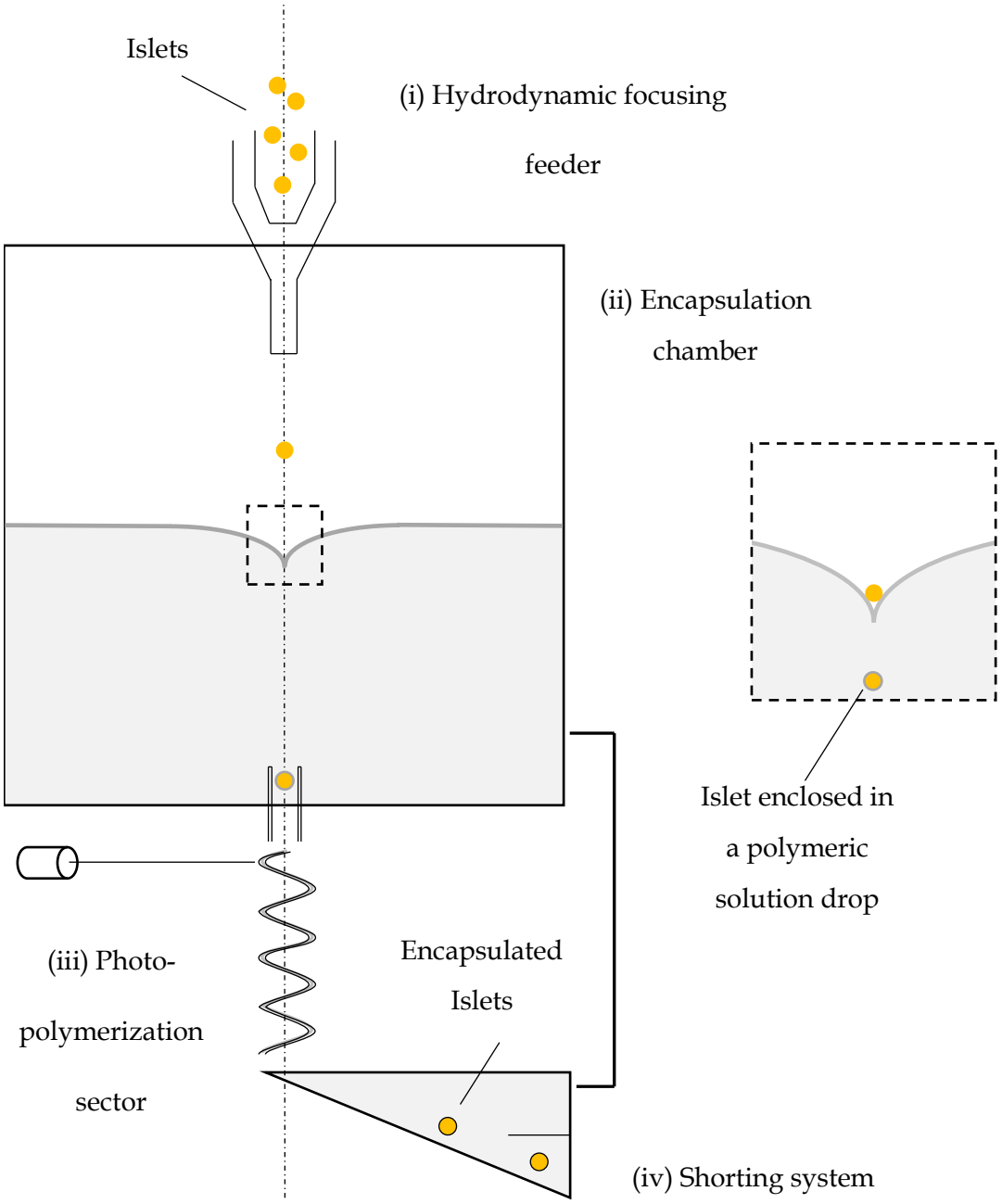

Figure 2.1 The functional parts of the apparatus. (i) a hydrodynamic focusing feeder, which aligns the islets in a single file to the withdrawal tube; (ii) an encapsulation chamber where the islets are coated by a solution of PEG-DA; (iii) a coiled tube for photopolymerization where the polymer is crosslinked to form a conformal semipermeable membrane; and (iv) a sorting system, where the islets are isolated and recovered.

The feeding system is like those used in cytometers. A hydrodynamic focusing configuration is utilized to ensure feeding the individual islets in the direction to the inlet of a withdrawal tube. The focusing configuration can be either a cross-junction geometry with side channels perpendicular to a central channel or a two-nozzle system with one nozzle

inside the other. The sample fluid, comprised of precursor polymer solution, islets labeled with Eosin-Y and a cell culture medium is fed through a central channel. The sheath fluid comprised of precursor solution and culture medium is fed through the outer channels. Both sample and sheath fluid contain 1-vinyl-2-pyrolidinone and triethanolamine acting as accelerator and co-initiator for photopolymerization, respectively [77].

The encapsulation chamber is a vessel containing two horizontally stratified layers of two immiscible fluids. The islets enter the chamber in a file through a vertical tube with its outlet orifice above the interface of the two fluids. The lower fluid is a chlorinated hydrocarbon oil, while the upper fluid is a precursor polymer solution, an aqueous PEGDA solution. This solution also contains 1-vinyl-2-pyrolidinone and triethanolamine. The islets are encapsulated by utilizing the method of Cohen et al [78], who have applied it to coat microparticles.

The islets enclosed in polymeric solution drops enter the withdrawal tube, a tube of cross section equal to the tube feeding the islets and at the same distance on the other side of the interface. The withdrawal tube begins with a straight vertical part and ends with a coiled part providing enough time for polymer crosslinking and formation of a hydrogel membrane. A 514 nm light of an argon-ion laser is employed to excite Eosin-Y on the surface of the islets and initiate free-radical polymerization of the solution. As a result, PEGDA hydrogels are formed and the exposing time determines the degree of polymerization and the porosity and permeability of the capsule.

Lastly, the encapsulated islets are sorted and recovered using a gravity-driven microfluidic sorting system [79]. These systems have an advantage in cell handling over conventional mechanical filtration, as damaging mechanical stresses are avoided. In such a configuration, the width of the main channel progressively increases resulting in reduction of the horizontal velocity of the particle. Due to gravity forces, the particle starts to move downward and enters the separation channel. By exploiting both gravity and hydrodynamic forces in the isolation sector, the apparatus can continuously separate and recover the encapsulated islets.

2.1.1 A feeding system by hydrodynamic focusing

As previously stated, the utilization of hydrodynamic focusing is proposed as a feeding system in our device. In a typical cytometer, the volumetric fraction of cells is small (<0.1), thus, rendering the fluid–cell and the cell-cell interaction negligible. However, the volumetric fraction of islets is significant in the proposed feeding system. The size and the shape of the encapsulated material is mainly dependent on the cell source. Isolated mice, porcine, and human islets have been already tested in small animals, non-human primates and humans. There is a variety in size and shape contingent on the type of species, their age and health state [80], [81]. The diameter of a typical human islet ranges from 50 to 450 μm and can be differently shaped in elliptical or spherical arrangements. Large human islets (over 150 μm in diameter) are ellipsoidal in shape, while smaller are more spherical [82]. We can characterize the shape of the islet by the aspect ratio

$$\alpha = \frac{b}{a} \tag{2.1},$$

where *a* and *b* the major and minor axis, respectively. The size distribution can be assumed to follow a Weibull distribution [83], also known as Rosin-Rammler. The corresponding probability density function is given as:

$$F(d_{islets}) = \frac{N(d_{islets})}{N} = \frac{\kappa}{\lambda}\left(\frac{d_{islets}}{\lambda}\right)^{\kappa-1} e^{-\left(\frac{d_{islets}}{\lambda}\right)^{\kappa}} \tag{2.2},$$

where κ and λ are shape and scale parameters, respectively. Pluripotent stem cells, representing a promising alternative strategy in cell transplantation, are arranged in clusters consisting of several hundreds of differentiated cells, with diameters between 100 and 200 μm [84].

(i) (ii)

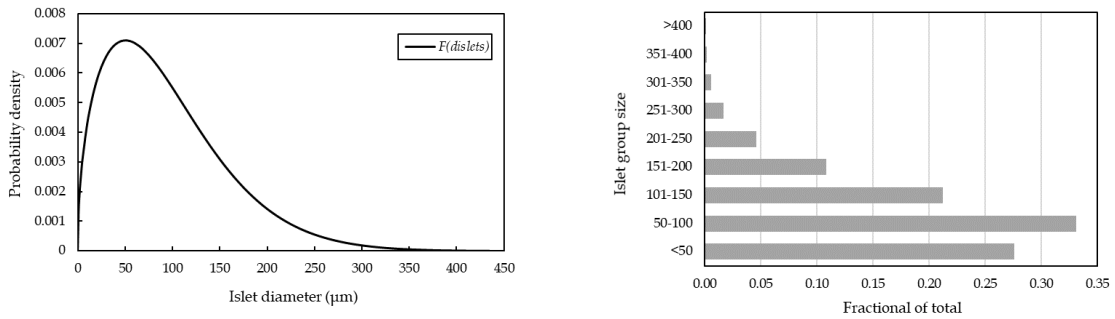

Figure 2.2 The probability density of islets as a function of d_{islets} and (ii) The fractional contribution per islet size group (κ=1.5, λ=105). Reprinted from [83].

Our hydrodynamic focusing system aims at feeding the pancreatic islets in a single file, thus ensuring separate encapsulation of individual islets. According to our design, the sample fluid with islets are fed through an inner channel, while the sheath fluid without islets, fed though side channels, forces the islets into a single file. The focusing configuration can be either a cross-junction geometry with side channels vertical to a central channel or a two-nozzle system. In symmetric focusing, i.e., equal sheath flow $Q_{sh1} = Q_{sh2} = Q_{sh}$, and the sheath-to-sample flow ratio is

$$k = \frac{Q_{sh}}{Q_{sa}} \tag{2.3}.$$

The length of the focusing channel, L, is constrained by the focusing length, l_{foc}, i.e., the minimum axial distance for a particle to be focused. Beyond this, the impact of sheath flows decays and a Hagen-Poiseuille flow may occur. Consequently, the focusing channel, L, has to be O(l_{foc}). For simplicity and symmetry reasons, all channels have the same width, W. It is $W \geq 3d_{islets}$ in order to allow easy passage of the islets. As it is known for particles moving in channels, the blockage ratio is

$$\beta = \frac{W}{a} \tag{2.4}.$$

Hereinafter, the encapsulated cellular material, i.e., cell islet or cluster, for the purposes of this Dissertation is termed as particle. In order to ensure proper focusing and separation, we must elucidate:

- What is the minimum value of the sheath-to-sample flow ratio for a group of particles to be separated and aligned?
- What is the focusing length, a critical design parameter of the central channel length?

The final position and the terminal translational velocity of the particle can be determined through numerical analysis. The terminal velocity, V_t, is the velocity that the particle enters the encapsulation chamber. Considering the case of an arbitrary-shape particle, the translational motion is obtained by applying Newton's second law

$$m\frac{d\mathbf{V}}{dt} = \mathbf{G} + \mathbf{F} \tag{2.5},$$

where **V** is the translational velocity; m is the mass; **G** is the body force due to gravity (**G**=m**g** where **g** is the gravity acceleration); **F** is the hydrodynamic force and is calculated by integrating the stress over the particle surface:

$$\mathbf{F} = -\int_{\partial\Omega_i(t)} \boldsymbol{\sigma} \cdot \mathbf{n_p}\, dS \tag{2.6},$$

where $\boldsymbol{\sigma}$ is the stress tensor given by $\boldsymbol{\sigma} = -p\mathbf{I} + \mu_f[\nabla\mathbf{u} + (\nabla\mathbf{u})^{\boldsymbol{T}}]$; and $\mathbf{n_p}$ is the unit normal vector on the surface of the particle pointing into the particle.

2.1.2 Microencapsulation by selective withdrawal

In the study by Cohen et al [85], a layer of an aqueous polymeric solution overlays a layer of a heavy mineral oil. The particles to be encapsulated enter the chamber with the two horizontally stratified layers through the aqueous phase. A flow Q is withdrawn through a tube the inlet orifice of which is at a fixed height above the interface of the two horizontally stratified layers. When the withdrawal flow is below a critical value Q_c, the interface is disturbed weakly and forms a steady-state smooth dent. This state is termed as hump by Cohen et al [85]. An increase in the flow, leads to a higher and more curved hump. As the flow reaches a critical value, the steady-state hump evolves dramatically and reaches a cusp shape.

Since only the one of two fluids is drained, this flow domain is known as the selective withdrawal regime [86]. In the selective withdrawal regime, capillary forces are greater than hydrodynamic forces and prevent the entrainment of the upper fluid. By increasing the flow beyond this threshold, a topological transition occurs. The tip of the cusp extends smoothly and enters the tube as a thin spout of diameter d_s. The simultaneous withdrawal of both liquid layers is called viscous entrainment. The dispersed particles become entrained in the spout and eventually coated by the upper fluid, as the spout breaks both above and below the particle because of stretching. Figure 2.3 illustrates the topological transitions from selective withdrawal (ii-iii) to viscous entrainment (iv).

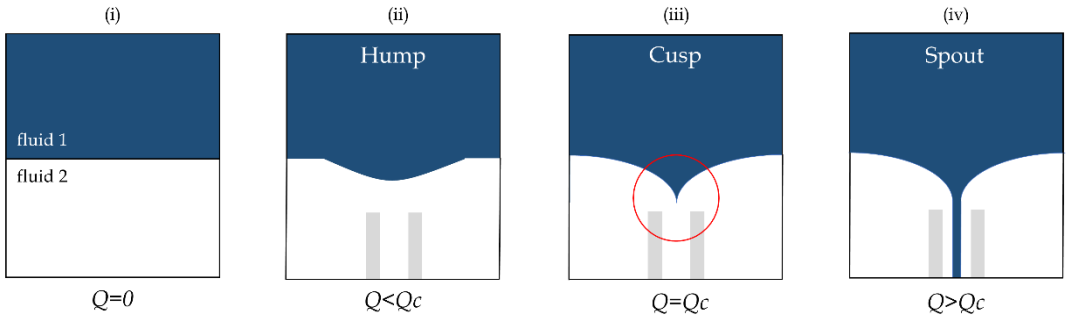

Figure 2.3 Illustration of topological transitions from selective withdrawal (ii-iii) to viscous entrainment (iv). (i) Two immiscible fluids at rest (ii) Hump (iii) Cusp (iv) Spout of diameter d_s.

In Hatziavramidis' original design, the islets are encapsulated by employing the hydrodynamics of the viscous entrainment regime. The main advantage of this approach is that enables uniform coating of diverse composition and controllable thickness of coating [86]. The spout can break both above and below the particle because of stretching, when the islet radius is larger than that of the spout [86], or because of Rayleigh capillary instability, when the islet radius is smaller than that of the spout [87]. In both cases the particle size has moderate effect on the thickness of the coating film. Given the heterogeneous size distribution and different shape, as well as the advantages of a membrane that conforms to the shape and size of the islet a slightly different approach is proposed.

In our modified design, the particles are encapsulated by employing the hydrodynamics of the selective withdrawal regime. The system feeds the particle in the same way as in the apparatus designed by Hatziavramidis [76], dealing with stochastic loading. A steady suction equal to Q_c is applied throughout the withdrawal tube, so that the interface

forms a steady-state cusp. The shape of the interface can be explicitly determined through a numerical solution of the the Navier-Stokes equations with boundary conditions at the interface given by:

$$\mathbf{u_1} \cdot \mathbf{n} = \mathbf{u_2} \cdot \mathbf{n} \tag{2.7}$$

$$\mathbf{n} \cdot [\mathbf{T_1} - \mathbf{T_2}] = \gamma \mathbf{n}(\nabla_t \cdot \mathbf{n}) - \nabla_t \gamma \tag{2.8},$$

where $\mathbf{u}_i$ and $\mathbf{T}_i$ is the fluid velocity and the total stress tensor; $\mathbf{n}$ is the unit outward normal vector to the surface; and γ the interfacial tension. The mean curvature, $\mathcal{H}$, of the axisymmetric interface of the form $z = f(r)$, can be calculated from:

$$2\mathcal{H} = \frac{f''(r)}{[1 + (f'(r))^2]} + \frac{f'(r)}{r[1 + (f'(r))^2]^{1/2}} \tag{2.9},$$

where $f'(r) = df/dr$ and $f''(r) = d^2f/dr^2$.

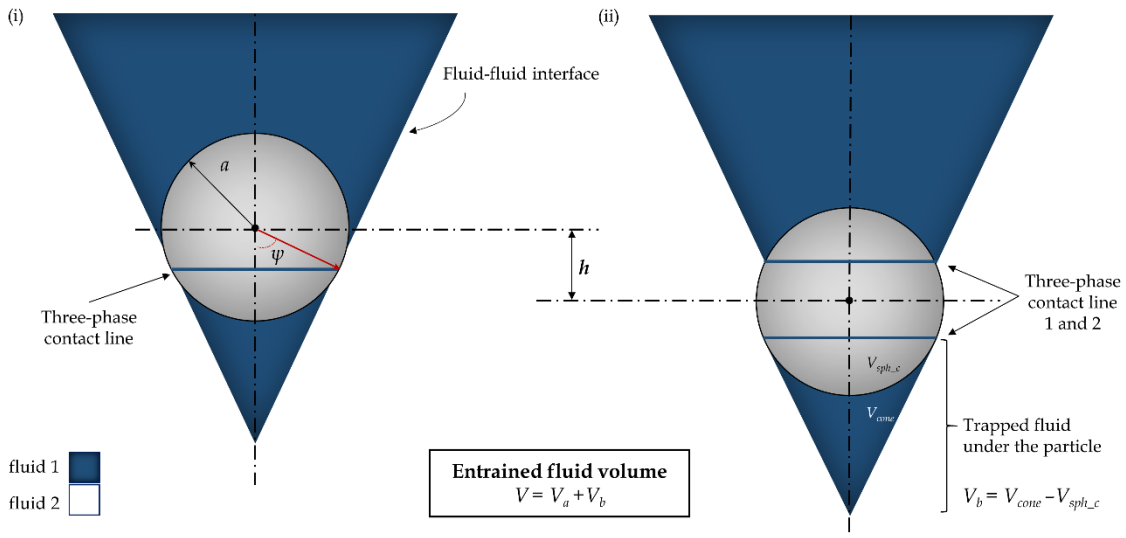

Figure 2.4 Concept illustration of encapsulation by selective withdrawal.

The particle enters the encapsulation chamber and moves towards the tip of the cusp, i.e., the point of the interface at maximum depth. At this point, the particle surface touches the interface forming a three-phase contact line (TPCL). The TPCL is exclusively determined by

the size of the particle and the interface shape, namely, the mean radius of the object and the depth, width and curvature of the cusp tip. Depending on the physical properties and the inertia of the particle and the fluids, the particle may either float or move through the interface. When the particle moves through the interface, a volume of the upper fluid below, V_b, and above, V_a, the TPCL is entrained along with the particle. In consequence, a twofold question arises:

- What is the condition for a moving particle to move through a dynamic steady-state interface?
- What is the volume of the upper fluid being entrained and attached to the particle surface?

Figure 2.4 illustrates a simplified configuration of the process by assuming the particle as a rigid sphere of radius a and density ρ_p, and the tip of the cusp as truncated conical volume below the TPCL. In, particular, the volume of the trapped fluid below the TPCL, V_b, is the volume of a cone $V_{cone} = \frac{1}{3}\pi a^3 \frac{\sin\psi^4}{\cos\psi}$ minus the volume of a spherical cap $V_{spc} = \frac{1}{3}\pi a^3(2 - 3cos\psi + \cos\psi^3)$. We note that when ψ=π/2, corresponding to a spout formation, the volume V_b becomes infinite.

As the particle moves downward with velocity $V=dh/dt$, the detachment stage begins. The assumption of total wetting, i.e., neglecting the film thickness at the flank, leads to a second TPCL on the upper side of the particle. The volume V_a can be approximately estimated according to the interface shape at breakup [88]. The mean radius of the entrained volume is O(a), while the height depends on the breakthrough mode. Tailing mode indicates the formation of a truncated column, while film draining indicates a truncated conical volume [89][90][88][91]. We want to highlight the fact that in all studies the upper fluid is oil, while it is water in our case.

Generally, a static breakthrough occurs when the weight force, F_w, is greater than the sum of the buoyancy force, F_b, and the vertically resolved surface tension force, F_σ, acting per unit length of the TPCL [92][93]. Hence, breakthrough is possible for spheres for which

$$\rho_f V_p g \; + \; 2\pi\gamma a \sin 2\psi - \rho_p V_p g \; < \; 0 \qquad (2.10).$$

As the interfacial tension between the two fluids is 0.03 N/m, a typical value for water-oil interface, the leading term in our case is the surface tension force. In particular, F_σ is three orders of magnitude greater than the two other forces for a sphere of radius a=75 μm. The condition $F_b + F_\sigma > F_w$ is valid even for larger spheres. Although the importance of the surface tension force is highlighted, this is strictly a static approach and does not include the inertia of the sphere and the two fluids. Incorporation of sphere dynamics may probably alter the outcome. To gain a straightforward understanding of the phenomenon, an experimental study is necessary.

References

[1] G. A. Rutter, T. J. Pullen, D. J. Hodson, and A. Martinez-Sanchez, "Pancreatic β-cell identity, glucose sensing and the control of insulin secretion," *Biochem J*, vol. 466, no. 2, pp. 203–218, 2016.

[2] A. M. J. Shapiro, M. Pokrywczynska, and C. Ricordi, "Clinical pancreatic islet transplantation," *Nat. Rev. Endocrinol.*, vol. 13, no. 5, p. 268, 2017.

[3] J. Størling and F. Pociot, "Type 1 Diabetes Candidate Genes Linked to Pancreatic Islet Cell Inflammation and Beta-Cell Apoptosis Joachim," *Genes (Basel).*, vol. 8, no. 2, p. 72, 2017.

[4] S. A. Paschou, N. Papadopoulou-Marketou, G. P. Chrousos, and C. Kanaka-Gantenbein, "On type 1 diabetes mellitus pathogenesis," *Endocr. Connect.*, vol. 7, no. 1, pp. R38–R46, 2018.

[5] V. Pathak, N. M. Pathak, C. L. O. Neill, J. Guduric-fuchs, and R. J. Medina, "Therapies for Type 1 Diabetes: Current Scenario and Future Perspectives," *Clin. Med. Insights Endocrinol. Diabetes*, vol. 12, p. 1179551419844521, 2019.

[6] B. Ludwig *et al.*, "Transplantation of human islets without immunosuppression," *Proc. Natl. Acad. Sci.*, vol. 110, no. 47, pp. 19054–19058, 2013.

[7] S. Pellegrini, E. Cantarelli, V. Sordi, R. Nano, and L. Piemonti, "The state of the art of islet transplantation and cell therapy in type 1 diabetes," *Acta Diabetol.*, vol. 53, no. 5, pp. 683–691, 2016.

[8] Y. Fukuda, T. Akagi, T. Asaoka, H. Eguchi, and K. Sasaki, "Layer-by-layer cell coating technique using extracellular matrix facilitates rapid fabrication and function of pancreatic b-cell spheroids," *Biomaterials*, vol. 160, pp. 82–91, 2018.

[9] M. R. Haque *et al.*, "Xenotransplantation of layer-by-layer encapsulated non-human primate islets with a specified immunosuppressive drug protocol," *J. Control. Release*, vol. 258, pp. 10–21, 2017.

[10] H. Park *et al.*, "Polymeric nano-shielded islets with heparin-polyethylene glycol in a non-human primate model," *Biomaterials*, vol. 171, pp. 164–177, 2018.

[11] S. Lou, X. Zhang, J. Zhang, J. Deng, D. Kong, and C. Li, "Pancreatic islet surface bioengineering with a heparin-incorporated starPEG nanofilm," *Mater. Sci. Eng. C*, vol. 78, pp. 24–31, 2017.

[12] M. Ma *et al.*, "Core-shell Hydrogel Microcapsules for Improved Islets Encapsulation," *Adv. Healthc. Mater.*, vol. 2, no. 5, pp. 667–672, 2013.

[13] Y. Teramura, O. P. Oommen, J. Olerud, J. Hilborn, and B. Nilsson, "Microencapsulation

of cells, including islets, within stable ultra-thin membranes of maleimide-conjugated PEG-lipid with multifunctional crosslinkers," *Biomaterials*, vol. 34, no. 11, pp. 2683–2693, 2013.

[14] A. Tomei *et al.*, "Device design and materials optimization of conformal coating for islets of Langerhans.," *Proc. Natl. Acad. Sci. U. S. A.*, vol. 111, no. 29, pp. 10514–9, 2014.

[15] V. Manzoli *et al.*, "Immunoisolation of Murine Islet Allografts in Vascularized Sites Through Conformal Coating with Polyethylene Glycol," *Am. J. Transplant.*, vol. 18, no. 3, pp. 590–603, 2018.

[16] D. Chaimov, L. Baruch, S. Krishtul, I. Meivar-levy, S. Ferber, and M. Machluf, "Innovative encapsulation platform based on pancreatic extracellular matrix achieve substantial insulin delivery," *J. Control. Release*, vol. 257, pp. 91–101, 2017.

[17] A. R. Pepper, B. Gala-Lopez, R. Pawlick, S. Merani, T. Kin, and A. M. J. Shapiro, "A prevascularized subcutaneous device-less site for islet and cellular transplantation," *Nat. Biotechnol.*, vol. 33, no. 5, pp. 518–523, 2015.

[18] K. Kirk, E. Hao, R. Lahmy, and P. Itkin-Ansari, "Human embryonic stem cell derived islet progenitors mature inside an encapsulation device without evidence of increased biomass or cell escape," *Stem Cell Res.*, vol. 12, no. 3, pp. 807–814, 2014.

[19] B. Ludwig, S. Ludwig, A. Steffen, Y. Knauf, B. Zimerman, and S. Heinke, "Favorable outcome of experimental islet xenotransplantation without immunosuppression in a nonhuman primate model of diabetes," *Proc. Natl. Acad. Sci.*, p. 201708420, 2017.

[20] Y. Evron *et al.*, "Long-term viability and function of transplanted islets macroencapsulated at high density are achieved by enhanced oxygen supply," *Sci. Rep.*, no. September 2017, pp. 1–13, 2018.

[21] T. Boettler *et al.*, "Pancreatic Tissue Transplanted in TheraCyte ™ Encapsulation Devices Is Protected and Prevents Hyperglycemia in a Mouse Model of Immune-Mediated Diabetes," *Cell Transplant.*, vol. 25, no. 3, pp. 609–614, 2016.

[22] M. Kumagai-Braesch *et al.*, "The TheraCyte ™ Device Protects Against Islet Allograft Rejection in Immunized Hosts," *Cell Transplant.*, vol. 22, no. 7, pp. 1137–1146, 2013.

[23] A. D. Agulnick, D. M. Ambruzs, M. A. Moorman, A. Bhoumik, R. M. Cesario, and J. K. Payne, "Insulin-Producing Endocrine Cells Differentiated In Vitro From Human Embryonic Stem Cells Function in Macroencapsulation Devices In Vivo," *Stem Cells Transl. Med.*, vol. 4, no. 10, pp. 1214–1222, 2015.

[24] T. Robert *et al.*, "Functional Beta Cell Mass from Device-Encapsulated hESC-Derived Pancreatic Endoderm Achieving Metabolic Control," *Stem cell reports*, vol. 10, no. 3, pp. 739–750, 2018.

[25] M. Köllmer, A. A. Appel, S. I. Somo, and E. M. Brey, "Long-term function of alginate encapsulated islets," *Tissue Eng. Part B Rev.*, p. ten.TEB.2015.0140, 2015.

[26] S. I. Somo *et al.*, "Synthesis and evaluation of dual crosslinked alginate microbeads," *Acta Biomater.*, vol. 65, pp. 53–65, 2018.

[27] J. Dusseault *et al.*, "Evaluation of alginate purification methods: Effect on polyphenol, endotoxin, and protein contamination," *J. Biomed. Mater. Res. - Part A*, vol. 76, no. 2, pp. 243–251, 2006.

[28] G. Klöck *et al.*, "Production of purified alginates suitable for use in immunoisolated transplantation," *Appl. Microbiol. Biotechnol.*, vol. 40, no. 5, pp. 638–643, 1994.

[29] J. C. Breger, B. Fisher, R. Samy, S. Pollack, N. S. Wang, and I. Isayeva, "Synthesis of 'click' alginate hydrogel capsules and comparison of their stability, water swelling, and diffusion properties with that of Ca^{+2} crosslinked alginate capsules," *J. Biomed. Mater. Res. - Part B Appl. Biomater.*, vol. 103, no. 5, pp. 1120–1132, 2015.

[30] R. M. Desai, S. T. Koshy, S. A. Hilderbrand, D. J. Mooney, and N. S. Joshi, "Versatile click alginate hydrogels crosslinked via tetrazine-norbornene chemistry," *Biomaterials*, vol. 50, no. 1, pp. 30–37, 2015.

[31] H. K. Yang *et al.*, "Long-term Efficacy and Biocompatibility of Encapsulated Islet Transplantation with Chitosan-Coated Alginate Capsules in Mice and Canine Models of Diabetes," *Transplantation*, vol. 100, no. 2, pp. 334–343, 2016.

[32] A. L. Hillberg, M. Oudshoorn, J. B. B. Lam, and K. Kathirgamanathan, "Encapsulation of porcine pancreatic islets within an immunoprotective capsule comprising methacrylated glycol chitosan and alginate," *J. Biomed. Mater. Res. - Part B Appl. Biomater.*, vol. 103, no. 3, pp. 503–518, 2015.

[33] M. Kumar, S. K. Nandi, D. L. Kaplan, and B. B. Mandal, "Localized Immunomodulatory Silk Macrocapsules for Islet-like Spheroid Formation and Sustained Insulin Production," *ACS Biomater. Sci. Eng.*, vol. 3, no. 10, pp. 2443–2456, 2017.

[34] R. M. Olabisi, "Cell microencapsulation with synthetic polymers," *J. Biomed. Mater. Res. - Part A*, vol. 103, no. 2, pp. 846–859, 2015.

[35] G. Marchioli *et al.*, "Layered PEGDA hydrogel for islet of Langerhans encapsulation and improvement of vascularization," *J. Mater. Sci. Mater. Med.*, vol. 28, no. 12, pp. 1–12, 2017.

[36] O. Veiseh *et al.*, "Size- and shape-dependent foreign body immune response to materials implanted in rodents and non-human primates," *Nat. Mater.*, vol. 14, no. 6, pp. 643–651, 2015.

[37] H. Shih, R. G. Mirmira, and C.-C. Lin, "Visible light-initiated interfacial thiol-norbornene photopolymerization for forming an islet surface conformal coating.," *J. Mater. Chem. B Mater. Biol. Med.*, vol. 3, no. 2, pp. 170–175, 2015.

[38] K. Gattas-Asfura and C. L. Stabler, "Bioorthogonal layer-by-layer encapsulation of pancreatic islets via hyperbranched polymers," *ACS Appl. Mater. Interfaces*, vol. 5, no. 20, pp. 9964–9974, 2013.

[39] H. Ren, Y. Sang, F. Zhang, Z. Liu, N. Qi, and Y. Chen, "Comparative Analysis of Human Mesenchymal Stem Cells from Umbilical Cord, Dental Pulp, and Menstrual Blood as Sources for Cell Therapy," *Stem Cells Int.*, vol. 2016, pp. 1–13, Jan. 2016.

[40] U. G. Thakkar, H. L. Trivedi, A. V. Vanikar, and S. D. Dave, "Insulin-secreting adipose-derived mesenchymal stromal cells with bone marrow-derived hematopoietic stem cells from autologous and allogenic sources for type 1 diabetes mellitus," *Cytotherapy*, vol. 17, no. 7, pp. 940–947, 2015.

[41] O. M. Sabek *et al.*, "Characterization of a nanogland for the autotransplantation of human pancreatic islets," *Lab Chip*, vol. 13, no. 18, p. 3675, 2013.

[42] J. A. Giraldo *et al.*, "The impact of cell surface PEGylation and short-course immunotherapy on islet graft survival in an allogeneic murine model," *Acta Biomater.*, vol. 49, pp. 272–283, 2017.

[43] L. T.-T. Dang, N. K. Phan, and K. D. Truong, "Mesenchymal stem cells for diabetes mellitus treatment: new advances," *Biomed. Res. Ther.*, vol. 4, no. 1, pp. 1062–1081, 2017.

[44] A. J. Vegas *et al.*, "Long-term glycemic control using polymer-encapsulated human stem cell-derived beta cells in immune-competent mice," *Nat. Med.*, vol. 22, no. 3, pp. 306–311, 2016.

[45] P. Chhabra and K. L. Brayman, "Stem Cell Therapy to Cure Type 1 Diabetes: From Hype to Hope," *Stem Cells Transl. Med.*, vol. 2, no. 5, pp. 328–336, 2013.

[46] T. Fujikawa, S.-H. Oh, L. Pi, H. M. Hatch, T. Shupe, and B. E. Petersen, "Teratoma Formation Leads to Failure of Treatment for Type I Diabetes Using Embryonic Stem Cell-Derived Insulin-Producing Cells," *Am. J. Pathol.*, vol. 166, no. 6, pp. 1781–1791, Jun. 2005.

[47] S. Véri ter *et al.*, "Improvement of subcutaneous bioartificial pancreas vascularization and function by coencapsulation of pig islets and mesenchymal stem cells in primates," *Cell Transplant.*, vol. 23, no. 11, pp. 1349–1364, 2014.

[48] R. S. Teotia *et al.*, "Islet encapsulated implantable composite hollow fiber membrane based device: A bioartificial pancreas," *Mater. Sci. Eng. C*, vol. 77, pp. 857–866, 2017.

[49] L. Baeyens *et al.*, "Transient cytokine treatment induces acinar cell reprogramming and regenerates functional beta cell mass in diabetic mice," *Nat. Biotechnol.*, vol. 32, no. 1, pp. 76–83, Jan. 2014.

[50] M. Zhang *et al.*, "Growth factors and medium hyperglycemia induce Sox9+ ductal cell differentiation into β cells in mice with reversal of diabetes.," *Proc. Natl. Acad. Sci. U. S. A.*, vol. 113, no. 3, pp. 650–5, Jan. 2016.

[51] R. Bouchi *et al.*, "FOXO1 inhibition yields functional insulin-producing cells in human gut organoid cultures," *Nat. Commun.*, vol. 5, p. 4242, Jun. 2014.

[52] C. Ariyachet *et al.*, "Reprogrammed Stomach Tissue as a Renewable Source of

Functional β Cells for Blood Glucose Regulation," *Cell Stem Cell*, vol. 18, no. 3, pp. 410–421, 2016.

[53] M. Cito, S. Pellegrini, L. Piemonti, and V. Sordi, "The potential and challenges of alternative sources of β cells for the cure of type 1 diabetes," *Endocr. Connect.*, vol. 7, no. 3, pp. R114–R125, 2018.

[54] H. Zhu, L. Lu, X. Liu, L. Yu, Y. Lyu, and B. Wang, "Treatment of diabetes with encapsulated pig islets: an update on current developments," *J. Zhejiang Univ. B*, vol. 16, no. 5, pp. 329–343, 2015.

[55] Y. Sato *et al.*, "Cellular hypoxia of pancreatic ??-cells due to high levels of oxygen consumption for insulin secretion in vitro," *J. Biol. Chem.*, vol. 286, no. 14, pp. 12524–12532, 2011.

[56] M. Padmasekar, N. Lingwal, B. Samikannu, C. Chen, H. Sauer, and T. Linn, "Exendin-4 protects hypoxic islets from oxidative stress and improves islet transplantation outcome," *Endocrinology*, vol. 154, no. 4, pp. 1424–1433, 2013.

[57] B. Lew, I.-Y. Kim, H. Choi, and K. Kim, "Sustained exenatide delivery via intracapsular microspheres for improved survival and function of microencapsulated porcine islets," *Drug Deliv. Transl. Res.*, pp. 1–6, 2018.

[58] E. A. Phelps, D. M. Headen, W. R. Taylor, P. M. Thulé, and A. J. García, "Vasculogenic bio-synthetic hydrogel for enhancement of pancreatic islet engraftment and function in type 1 diabetes," *Biomaterials*, vol. 34, no. 19, pp. 4602–4611, 2013.

[59] G. Marchioli *et al.*, "Hybrid Polycaprolactone/Alginate Scaffolds Functionalized with VEGF to Promote de Novo Vessel Formation for the Transplantation of Islets of Langerhans," *Adv. Healthc. Mater.*, vol. 5, no. 13, pp. 1606–1616, 2016.

[60] C. K. Colton, "Oxygen supply to encapsulated therapeutic cells ☆," *Adv. Drug Deliv. Rev.*, vol. 67–68, pp. 93–110, 2014.

[61] S.-H. Lee *et al.*, "Improvement of islet function and survival by integration of perfluorodecalin into microcapsules *in vivo* and *in vitro*," *J. Tissue Eng. Regen. Med.*, 2018.

[62] A. Rodriguez-Brotons *et al.*, "Comparison of Perfluorodecalin and HEMOXCell as Oxygen Carriers for Islet Oxygenation in an *In Vitro* Model of Encapsulation," *Tissue Eng. Part A*, vol. 22, no. 23–24, pp. 1327–1336, 2016.

[63] M. H. Tootoonchi, M. Hashempour, P. L. Blackwelder, and C. A. Fraker, "Manganese oxide particles as cytoprotective, oxygen generating agents," *Acta Biomater.*, vol. 59, pp. 327–337, 2017.

[64] S. Song and S. Roy, "Progress and challenges in macroencapsulation approaches for type 1 diabetes (T1D) treatment: Cells, biomaterials, and devices," *Biotechnol. Bioeng.*, vol. 113, no. 7, pp. 1381–1402, 2016.

[65] A. P. Chandra *et al.*, "Association between islet xenograft rejection mediated by

activated macrophages and upregulated chemokines.," *Zhong Nan Da Xue Xue Bao. Yi Xue Ban*, vol. 32, no. 1, pp. 26–35, Feb. 2007.

[66] A. Corrado, S. M. Ferrari, C. Ferri, E. Ferrannini, A. Antonelli, and P. Fallahi, "Type 1 diabetes and (C-X-C motif) ligand (CXCL) 10 chemokine.," *Clin. Ter.*, vol. 165, no. 2, pp. e181-5, 2014.

[67] A. Zhernakova *et al.*, "Genetic variants of RANTES are associated with serum RANTES level and protection for type 1 diabetes," *Genes Immun.*, vol. 7, no. 7, pp. 544–549, Oct. 2006.

[68] T. Chen *et al.*, "Alginate encapsulant incorporating CXCL12 supports long-term allo- and xenoislet transplantation without systemic immune suppression," *Am. J. Transplant.*, vol. 15, no. 3, pp. 618–627, 2015.

[69] T. T. Pham *et al.*, "Tissue adhesive FK506–loaded polymeric nanoparticles for multi–layered nano–shielding of pancreatic islets to enhance xenograft survival in a diabetic mouse model," *Biomaterials*, vol. 154, pp. 182–196, 2018.

[70] L. A. Llacua, A. Hoek, B. J. de Haan, and P. de Vos, "Collagen type VI interaction improves human islet survival in immunoisolating microcapsules for treatment of diabetes," *Islets*, vol. 2014, p. e1420449, 2018.

[71] D. Pham-Hua *et al.*, "Islet encapsulation with polyphenol coatings decreases pro-inflammatory chemokine synthesis and T cell trafficking," *Biomaterials*, vol. 128, pp. 19–32, 2017.

[72] T. Desai and L. D. Shea, "Advances in islet encapsulation technologies," *Nat. Rev. Drug Discov.*, vol. 16, no. 5, p. 338, 2017.

[73] J. C. Doloff *et al.*, "Colony stimulating factor-1 receptor is a central component of the foreign body response to biomaterial implants in rodents and non-human primates," *Nat. Mater.*, vol. 16, no. 6, pp. 671–680, 2017.

[74] P. Carlsson *et al.*, "Transplantation of macroencapsulated human islets within the bioartificial pancreas β Air to patients with type 1 diabetes mellitus," *Am. J. Transplant.*, 2017.

[75] D. A. Baidal *et al.*, "Bioengineering of an Intraabdominal Endocrine Pancreas," *N. Engl. J. Med.*, vol. 376, no. 19, pp. 1887–1889, 2017.

[76] D. T. Hatziavramidis, T. M. Karatzas, and G. P. Chrousos, "Pancreatic islet cell transplantation: An update," *Ann. Biomed. Eng.*, vol. 41, no. 3, pp. 469–476, 2013.

[77] G. M. Cruise, D. S. Scharp, and J. A. Hubbell, "Characterization of permeability and network structure of interfacially photopolymerized poly(ethylene glycol) diacrylate hydrogels," *Biomaterials*, vol. 19, no. 14, pp. 1287–1294, 1998.

[78] I. Cohen, H. Li, J. L. Hougland, M. Mrksich, and S. R. Nagel, "Using selective withdrawal to coat microparticles.," *Science (80-.).*, vol. 292, no. 5515, pp. 265–267, 2001.

[79] D. Huh *et al.*, "Gravity-Driven Microfluidic Particle Sorting Device with Hydrodynamic Separation Amplification," *Anal. Chem.*, vol. 79, no. 4, pp. 1369–1376, 2007.

[80] D. Dufrane, R. M. Goebbels, I. Fdilat, Y. Guiot, and P. Gianello, "Impact of porcine islet size on cellular structure and engraftment after transplantation: Adult versus young pigs," *Pancreas*, vol. 30, no. 2, pp. 138–147, 2005.

[81] A. Kim, K. Miller, J. Jo, G. Kilimnik, P. Wojcik, and M. Hara, "Islet architecture: A comparative study.," *Islets*, vol. 1, no. 2, pp. 129–136, 2009.

[82] K. Ramachandran, H. Huang, and L. Stehno-bittel, "A Simple Method to Replace Islet Equivalents for Volume Quantification of Human Islets," *Cell Transplant.*, vol. 24, no. 7, pp. 1183–1194, 2015.

[83] P. Buchwald *et al.*, "Quantitative Assessment of Islet Cell Products: Estimating the Accuracy of the Existing Protocol and Accounting for Islet Size Distribution," *Cell Transplant.*, vol. 18, no. 10–11, pp. 1223–1235, 2009.

[84] F. W. Pagliuca *et al.*, "Generation of functional human pancreatic β cells in vitro," *Cell*, vol. 159, no. 2, pp. 428–439, 2014.

[85] I. Cohen and S. R. Nagel, "Scaling at the Selective Withdrawal Transition through a Tube Suspended above the Fluid Surface," *Phys. Rev. Lett.*, vol. 88, no. 7, p. 074501, 2002.

[86] M. K. Berkenbusch, I. Cohen, and W. W. Zhang, "Liquid interfaces in viscous straining flows: Numerical studies of the selective withdrawal transition," *J. Fluid Mech.*, vol. 613, pp. 171–203, 2008.

[87] M. G. Blyth and C. Pozrikidis, "Particle encapsulation due to thread breakup in Stokes flow," *J. Fluid Mech.*, vol. 617, pp. 141–166, 2008.

[88] H. Chen, Q. Xu, S. Liang, and J. Li, "Film coating on a small sphere crossing an oil-water interface," *Phys. Rev. Fluids*, vol. 3, no. 12, p. 124003, 2018.

[89] A. N. Srdić-Mitrović, N. A. Mohamed, and H. J. S. Fernando, "Gravitational settling of particles through density interfaces," *J. Fluid Mech.*, vol. 381, pp. 175–198, 1999.

[90] B. C. Tan, J. H. A. Vlaskamp, and P. Denissenko, "Cavity formation in the wake of falling spheres submerging into a stratified two-layer system of immiscible liquids," *J. Fluid Mech.*, vol. 790, pp. 33–56, 2016.

[91] P. A. Jarvis, H. M. Mader, H. E. Huppert, K. V. Cashman, and J. D. Blundy, "Experiments on the low-Reynolds-number settling of a sphere through a fluid interface," *Phys. Rev. Fluids*, vol. 4, no. 2, p. 024003, 2019.

[92] D. Vella, "Floating Versus Sinking," *Annu. Rev. Fluid Mech.*, vol. 47, pp. 115–135, 2015.

[93] J. Magnaudet and M. J. Mercier, "Particles, Drops, and Bubbles Moving Across Sharp Interfaces and Stratified Layers," *Annu. Rev. ofFluid Mech.*, vol. 52, pp. 61–91, 2020.

PART II

Computational and Experimental Research

Chapter

3 Modeling the motion of particles in a hydrodynamic focusing domain

Synopsis

In this Chapter, we develop a computational model to simulate the motion of particles in a hydrodynamic focusing configuration serving as a feeding system in our microencapsulation device. The simulation of the motion of biological entities in fluids is essential for the optimum design and development of efficient microfluidic-based medical devices. We initially present an overview of the classical numerical methods to simulate particle-fluid flows. Having presented and validated our methodology, we perform simulations with spherical and elliptical particles, individually released at the entrance of the main channel of a hydrodynamic focusing domain. Finally, we simulate the focusing and separation of two particles as well as a group of particles.

3.1 Introduction

Numerical simulations are a valuable tool to study the dynamics of particles moving in microfluidic domains. The modeling approach is mainly determined by the volumetric fraction of the discrete phase. Other aspects for consideration are the blockage ratio, i.e., the maximum diameter of the particle to the width of the channel, and the demand for resolution in the vicinity of the particle. Many researchers have employed classical continuum approaches, such as Eulerian and Lagrangian, to study solid-fluid suspensions. The Eulerian approach views the two phases as -interpenetrating continua in a fixed mesh described by the continuum equations either postulated or derived from averaging. In a Lagrangian numerical simulation, the flow of the continuous phase is described by the same equations of motion while the particle motion is expressed in terms of Newton's second law. When the concentration of the disperse phase is high, the effect of the particle movement on the flow is dealt with by adding a momentum exchange term into the balance equations (two-way coupling). In the event of a dilute dispersion, this influence is neglected (one-way coupling). Both these classical methods employ empirical forms of hydrodynamic forces. A new class of algorithms, known as Direct Numerical Simulation (DNS), have been developed to overcome this limitation. The main feature of DNS is that hydrodynamic forces are directly calculated from the fluid flow and the motions of solid and fluid phases are fully coupled [1].

A broadly used DNS method is an Arbitrary Lagrangian-Eulerian (ALE) technique that combines the best characteristics of Eulerian and Lagrangian approaches. Hu and co-workers [2][3] were first to propose an ALE-particle-mover scheme, which has undergone numerous alterations, to simulate fluid-particle motions. This formulation combines the fluid and particle motion equations, together with an ALE moving finite element mesh technique. At every time step, the mesh nodes on the particle surface are moved to follow the particle motion, while the mesh displacement in the interior of the fluid is computed by solving a Laplace equation assuring smooth variation. High accuracies can be accomplished by employing an ALE scheme due to a boundary-fitted mesh during the whole simulation [1]. As the particle moves resulting in mesh distortion, a remeshing procedure is necessary. This drawback should be handled in order to reduce the computational cost. Despite the need for periodically remeshing, the ALE method has already been used for the simulation of 1000 particles [4]. Several authors studied for a long time the motion of one or a finite number of

particles in Newtonian fluids by employing the ALE method. Hu et al [2] studied the sedimentation of circular and elliptical cylinders in a two-dimensional (2D) channel. Few years later, the motion of many circular particles was directly simulated by Hu [3]. Feng and co-workers investigated the interaction of sedimented particles for different scenarios [5], as well as the motion of a circular particle in Poiseuille and Couette flows [6]. Furthermore, the ALE method was applied to flows of a Non-Newtonian viscoelastic fluid by Huang et al [7]. D' Avino et al [8] reported the results of a 2D simulation on the migration of a suspending particle in a Poiseuille flow of a viscoelastic fluid.

Another approach to simulate fluid flows with particle-fluid interfaces is fictitious-domain (FD) methods - also called domain embedding methods. In a FD method, the mesh is fixed for the whole domain, and the forces are set so that the fluid domain, i.e., the fictitious domain, inside of which the particle behaves as if it was a rigid body. FD methods are mainly classified whether the forces are applied to the particle surface (immersed boundary methods) or the volume (immersed body methods). Glowinski et al [9][10] firstly proposed the Distributed Lagrange Multiplier (DLM) based FD method for particulate flows. The main idea is to embed a time-dependent complex computational domain into a larger, but simpler domain, i.e., the fictitious domain, and to apply simple boundary conditions. DLM-FD and variants have been applied to simulate particle-fluid flows [11][12][13][12].

The lattice-Boltzmann method (LBM) has become a useful alternative for simulating fluid-solid flows [14], and was initially applied by Ladd [15] to simulate flow of suspending particles. In the LBM formulation, simplified kinetic models are constructed based on microscopic and macroscopic equations. The hydrodynamic forces and moments on particles are computed by solving LBM and, consequently, these forces determine the movement of the particle using Newton's second law. Many groups proposed variants of LBM with interesting results by coupling LBM with multi-block [16], discrete element [17] and the immersed boundary method of Peskin [18][19] among others. For instance, Xia et al [20] studied the sedimentation of a 2D elliptical particle with high resolution near the particle surface using multi-block LBM. In LBM, the computational mesh is nonadaptive and eliminating the necessity for remeshing. Thus, it can be efficiently used for simulating many particles [21]. Recently, Başağaoğlu et al [22] investigated the motion of a mixture of different-shape particles in a 2D bounded domain via an extended LBM for discretized particle surfaces. Artificial forces, such as lubrication [23] or spring forces [19], are necessary to simulate the

dynamics of particulate flows. Research on LBM is described in a thorough review by Aidun and Clausen [24].

3.2 Problem statement

As already stated, the utilization of hydrodynamic focusing (HF) is proposed as a feeding system in our device. HF employs the interaction of two fluid streams, to confine the contents of the slow-moving fluid into a volume defined by the flow ratio of the two merging streams [25]. These systems are encountered in different features and geometries, such as cross-junction geometries with rectangular channels [26] and two-nozzle systems with linear- or curvilinear-shaped nozzles [27]. HF is a versatile tool and one of the most utilized techniques in microfluidics covering a wide range of engineering applications (e.g., [28][29][30][31]). The hydrodynamics of the interaction of two fluid streams have been studied through experiments [26], [27] as well as analytical [32] and numerical models [26][33][25]. The object of these studies is the precise control of the focusing width (radial width of the focused fluid) and focusing length (axial distance downstream from the inner zone exit as in [25]). The effect of focusing geometry, flow rates and fluid properties, i.e., density, viscosity and miscibility, is investigated.

In previous numerical studies, the sample fluid was assumed homogenous, even though it was loaded with cells or microparticles. To our knowledge, this is the first numerical study of HF with particles present. The primary purpose of our research is the effect of sheath-to-sample flow ratio on the separation and focusing of biological particles. We simplify our model by assuming that the islet shape slightly deforms due to fluid stresses. Moreover, the dependence of the motion of particles on their morphology is studied. Firstly, we perform simulations with spherical and elliptical particles, individually released at the entrance of the main channel of a HF domain. We continue by investigating the focusing and separation of two particles, as well as a group of particles of different shapes.

3.3 Methodology

3.3.1 Physical Model

We consider the case of the HF of particles in a two-dimensional cross-junction geometry. A schematic illustration is presented in Figure 3.1. The major and minor axis of the particle are a and b respectively. In physical units the width of all channels, W, are equal to 1.2 mm, and the length of the focusing channel, L, is equal to 24 mm. The density, ρ_f, and the viscosity, μ_f, of the sheath and sample fluid are 1000 g/ml and 0.01 N/m², respectively. The diameter of a pancreatic islet ranges from 50 to 450 μm [34] and is comparable to the diameter of the internal channel. This means that the trajectories can be notably influenced due to wall-particle interactions. Islets are encountered in ellipsoidal and spherical shapes [35]. Using MATLAB™'s image processing toolbox, the shape of the particles is extracted from microscopic images [Appendix A.1]. We model the particles by determining the aspect ratio, α, and the blockage ratio, β, as referred to in Chapter 2. The density ratio $\lambda=\rho_p/\rho_f$, where ρ_p the density of the particle, is equal to 1.059 or 1.250 corresponding to the density of islets and heavier particles, respectively. For that range, the density ratio has a moderate effect on particle motion [Appendix A.2].

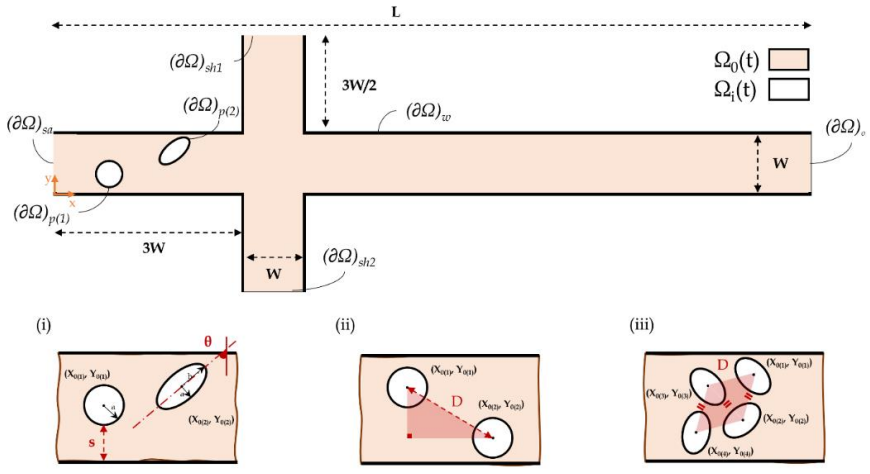

Figure 3.1 Schematic illustration of the hydrodynamic focusing domain. (i) A spherical and an elliptical disk. (ii) The distance of the centers of two disks. (iii) The distance between multiple disks.

3.3.2 Mathematical Model

We consider two-dimensional laminar flow of an incompressible Newtonian fluid of density, ρ_f, and viscosity, μ_f. The initially quiescent fluid contains particles i =1, 2, …, N with centers initially at ($X_{0(i)}$, $Y_{0(i)}$). The computational domain is denoted as $\Omega(t)$. The domain at time t that is occupied by each particle and the fluid is $\Omega_i(t)$ and $\Omega_0(t)=\Omega(t)-U\Omega_i(t)$, respectively. The x coordinate is taken in the direction of the axis of symmetry, which is also the direction of gravity. The y coordinate is in the lateral direction of the focusing channel. The flow in $\Omega_0(t)$ is described by:

$$\nabla \cdot \mathbf{u} = 0 \tag{3.1}$$

$$\rho_f \frac{D\mathbf{u}}{Dt} = \rho_f \mathbf{f} + \nabla \cdot \boldsymbol{\sigma}, \tag{3.2}$$

where $\mathbf{u}$ is the fluid velocity; $\mathbf{f}$ is the body force per unit mass; $\boldsymbol{\sigma}$ is the stress tensor given by:

$$\boldsymbol{\sigma} = -p\mathbf{I} + \mu_f[\nabla\mathbf{u} + (\nabla\mathbf{u})^T] \tag{3.3}$$

where p is the pressure. The translational motion of the particles satisfies Newton's second law:

$$m_i \frac{d\mathbf{V_i}}{dt} = \mathbf{G_i} + \mathbf{F_i} = \mathbf{G_i} - \int_{\partial\Omega_i(t)} \boldsymbol{\sigma} \cdot \mathbf{n}\, \mathrm{d}S \tag{3.4}$$

where $\mathbf{V}$ is the translational velocity; m is the mass; $\mathbf{G}$ is the body force exerted by external fields such as gravity; $\mathbf{F}$ is the hydrodynamic force acting on the particle; $\mathbf{n}$ is the unit normal vector on the surface of the particle pointing into the particle. The rotational motion satisfies Euler's equation:

$$\frac{d}{dt}(\mathbf{I_i}\omega_i) = \mathbf{T_i} = -\int_{\partial\Omega_i(t)} (\mathbf{x} - \mathbf{X_i}) \times (\boldsymbol{\sigma} \cdot \mathbf{n})\, \mathrm{d}S \tag{3.5}$$

where $\mathbf{I_i}$ is the moment of the inertia matrix of the i^{th} particle; ω is the angular velocity; $\mathbf{T_i}$ is the moment of force acting on the particle. Both $\mathbf{F_i}$ and $\mathbf{T_i}$ are calculated by integrating the stress over the particle surface. The centroid, $\mathbf{X_i}$, and the orientation, Θ_i, of each particle are updated at every time step according to:

$$\frac{d\mathbf{X_i}}{dt} = \mathbf{V_i} \tag{3.6}$$

$$\frac{d\Theta_i}{dt} = \omega_i \tag{3.7}$$

Appropriate boundary conditions are applied at the outer boundaries $(\partial\Omega)_j$ of the fluid, that is initially at rest. On the stationary walls of the microchannels, $(\partial\Omega)_{w1}$ and $(\partial\Omega)_{w2}$, the no-slip condition is applied. At the inlet $(\partial\Omega)_{sa,}$ the fluid velocity is u_{sa}, while at $(\partial\Omega)_{sh1}$ and $(\partial\Omega)_{sh2}$ it is u_{sh}. At the outlet, $(\partial\Omega)_o$, the traction-free condition is applied. We consider the no-slip condition on the particle surface, $(\partial\Omega)_{p(i)}$, and we assure that the motion of the fluid and the particles are fully coupled by applying the boundary condition:

$$\mathbf{u} = \mathbf{V_i} + \omega_i \times (\mathbf{x} - \mathbf{X_i}) \quad \mathbf{x} \in \partial\Omega_i(t) \tag{3.8}$$

3.3.3 Computational Model and Validation

3.3.3.1 Numerical Method

The governing equations are solved by implementing the Finite Element (FE) formalism on a triangular mesh T_h, where h_{mesh} is the typical mesh size, coupled with free time-stepping Backward Differential Formula with order of accuracy up to two, in the commercial simulation environment of COMSOL Multiphysics 5.0. Due to the particle motion, the mesh moves and deforms at every time step, t_{n+1}, and thus it is recreated by employing the ALE moving mesh technique [2], as is shown in Figure 3.2. Mesh refinement is performed mainly in regions in the vicinity of the particle and/or where solid surfaces approach each other.

On the wall boundaries, the mesh velocity, $\mathbf{u_{mesh}}$, is equal with the velocity that the boundary moves. The mesh nodes at the inlet and outlet boundaries are fixed. The mesh displacement in the interior of the fluid domain, $\Omega_0(t)$, is computed by solving a Laplace equation assuring smooth variation:

$$\nabla \cdot (k^e \nabla \mathbf{u_{mesh}}) = 0 \tag{3.9}$$

where k^e is the inverse of the local element volume. This control function ensures that the mesh deformation gets absorbed away from the particle surface, thus, keeping the region in the vicinity of the particle stiff. In order to obtain an accurate solution in a reasonable time, a convergence and mesh-independence test is made through preliminary numerical tests. By decreasing the mesh size until the solutions for two consecutive mesh sizes show no divergence, we ensure that the solution is independent of mesh size [Appendix A.3]. The maximum and minimum grid sizes are chosen to be a/3 and a/24, respectively.

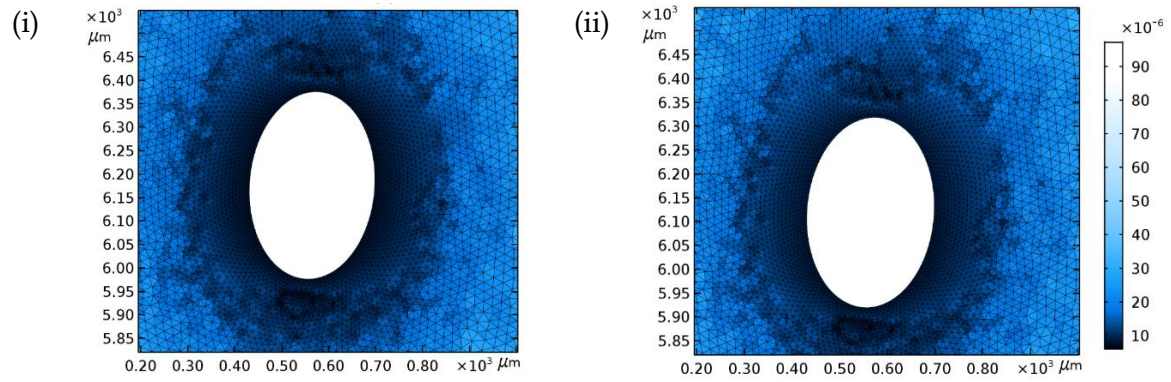

Figure 3.2 (i) The mesh at t_n (ii) The mesh at t_{n+1}. The two snapshots were taken at the vicinity of the particle.

3.3.3.2 Validation with other numerical models

We validate our model by comparing its results against those obtained from two studies investigating the sedimentation of circular and elliptical particles. In the first validation, the sedimentation of a circular disk (α=1.00) in a tube, filled with a fluid that is initially at rest, is simulated with our model and the results are compared against the solution of the same problem by Glowinski et al [Glowinski et al, 2001]. In these simulations, the computational domain, $\Omega(t) = \Omega_0(t) + U\Omega_i(t)$, is $\Omega = (0, 2) \times (0, 6)$ cm, the radius of the disk is a=0.125 cm and the disk is initially located at $(X_{0(1)}, Y_{0(1)}) = (1, 4)$. c. Comparison of our solution and the results of Glowinski et al [10] showed good agreement. A slight difference in the terminal velocity is observed (less than 1.5%) and it is mainly attributed to the different numerical methodology. We follow the simulation of a single disk with the sedimentation of two disks, before a collision occurs. The disks are initially located at $(X_{0(1)}, Y_{0(1)}) = (1, 5)$ and $(X_{0(2)}, Y_{0(2)}) = (1, 4.5)$. Figure 3.3 shows that our results are in good agreement with the published results. In the

second validation model, the trajectory and angular rotation of an elliptical disk (α=2.00) sedimenting in a tube, filled with a fluid that is initially at rest, is simulated and the results are compared against the solutions of Xia et al [20]. The initial angle, θ, of the ellipse is π/4 and the center of the ellipse is on the axis of the channel. The physical parameters and the boundary conditions are the same as in Xia et al [20]. Figure 3.4 shows that the trajectory and the orientation of an elliptical disk computed by our method are in good agreement with the results of Xia et al [20].

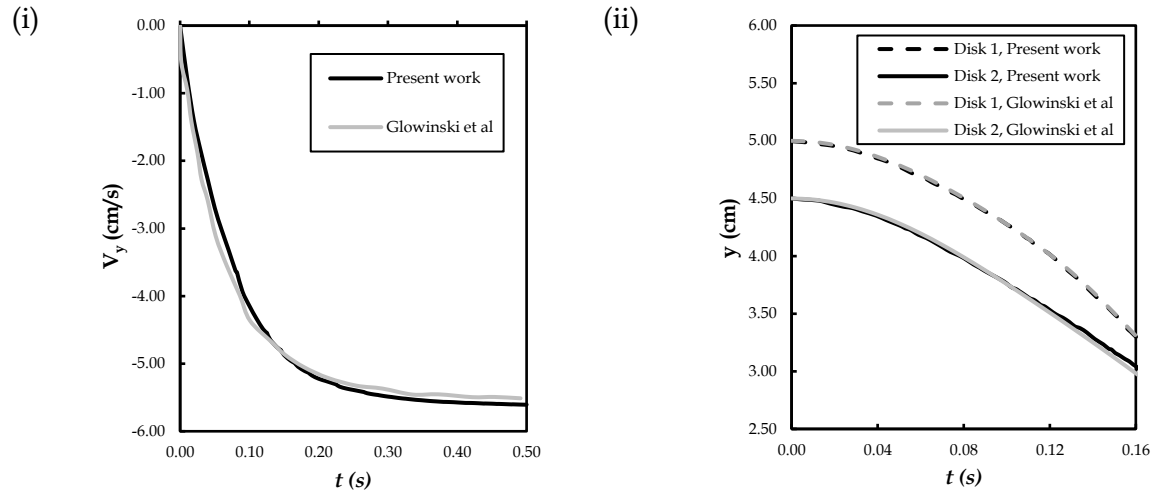

Figure 3.3 (i) The velocity, V_x, of one disk and (ii) the trajectory of two disks sedimenting in a domain as in Ref. [10].

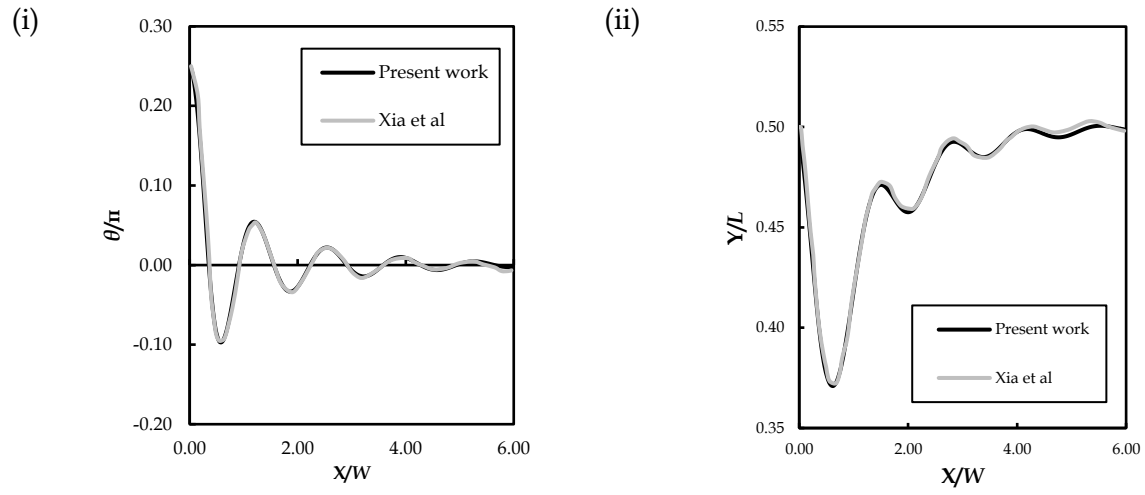

Figure 3.4 (i)The trajectory and (ii) the orientation angle of the sedimented ellipse in a domain as in Ref. [20].

3.4 Results and Discussion

3.4.1 Focusing of a circular particle

In this Section, we present computations of one circular disk (α=1.00, β=6.00) moving in a HF domain. The disk is at rest and located at ($X_{0(1)}$, $Y_{0(1)}$), far enough from the inlet boundary, S_{sa}, where the flow is fully developed. The density ratio is λ=1.250. We firstly conduct preliminary simulations with the disk at the central axis of the main channel, ($X_{0(1)}$, $Y_{0(1)}$)=(W, $W/2$), to ensure that symmetry is preserved even for high values of sheath-to-sample flow ratio, k.

We simulate the focusing of one disk with various initial positions ($X_{0(1)}$, $Y_{0(1)}$) = (W, a+s), where s is the distance of the particle surface from the wall. In Figure 3.5 (i), snapshots of a particle are presented for time step Δt=0.02s. The particle is initially released at $Y_{0(1)}$ =3a/2 and the flow ratio k is 6. Figure 3.5 (ii) shows the trajectory of the particle. As the disk approaches the focusing area, i.e., the area which the side channels are attached to the main channel, the vertical position, $Y_{0(1)}$, is constant. Snapshots at the focusing area are also presented for time step Δt=0.01s.

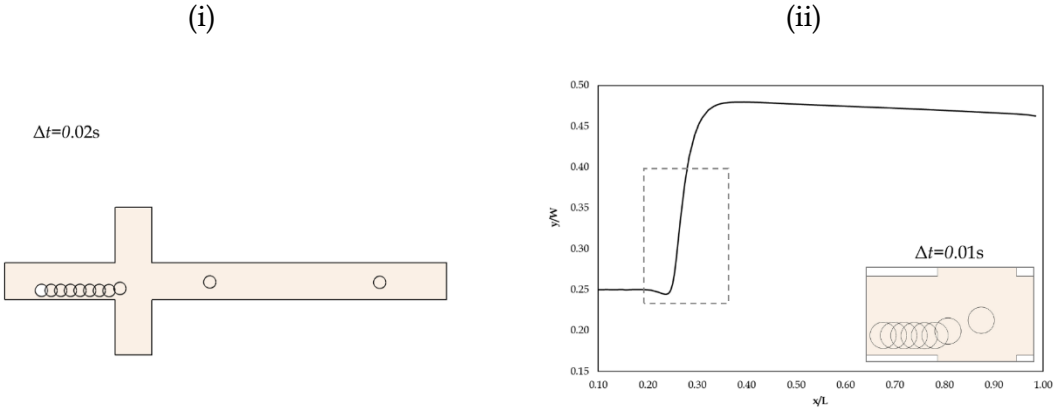

Figure 3.5 Focusing of a disk initially released at $Y_{0(1)}$ =3a/2 (white infill). The flow ratio is k=2. (i) Snapshots for time step Δt=0.02s (ii) Trajectory and snapshots for time step Δt=0.01s.

In Figure 3.6, the trajectory and the angular velocity of a disk for various sheath-to-sample flow ratios, k, is presented. Depending on the ratio k, the center of the disk changes and moves close to the channel axis. According to Figure 3.6 (i) where s=a/2, the final position of the disk is closer to the channel axis, as the value of k increases. After a certain point and all

the way to the outlet, the position, $Y_{0(1)}$, of the disk does slightly change (less than 3%). In Figure 3.6 (ii) and (iii), the trajectory and the angular velocity with initial s equal with $a/9$ and $a/12$ respectively, are presented. The disk moves in the same manner. Figure 3.6 (iv-vi) show the angular velocity, ω, of the disk, varying with the nondimensional time $t^*=t/T$, where T is the time needed for a disk to reach the outlet. In the flow domain before the disk reaches the cross section with the side channels, its angular velocity is negative, constant and equal in all cases studied. The disk rotates more in one direction as it moves, due to uneven shear stresses on its segments facing the wall. For constant inlet flow, the value of angular velocity varies with the initial distance of the disk from the wall. As the disk enters the focusing area, the angular velocity decreases and for k>1 the disk rotation reverses. This alteration can be attributed to the nonlinear effect of inertia caused mainly from the sheath flow of the closest channel.

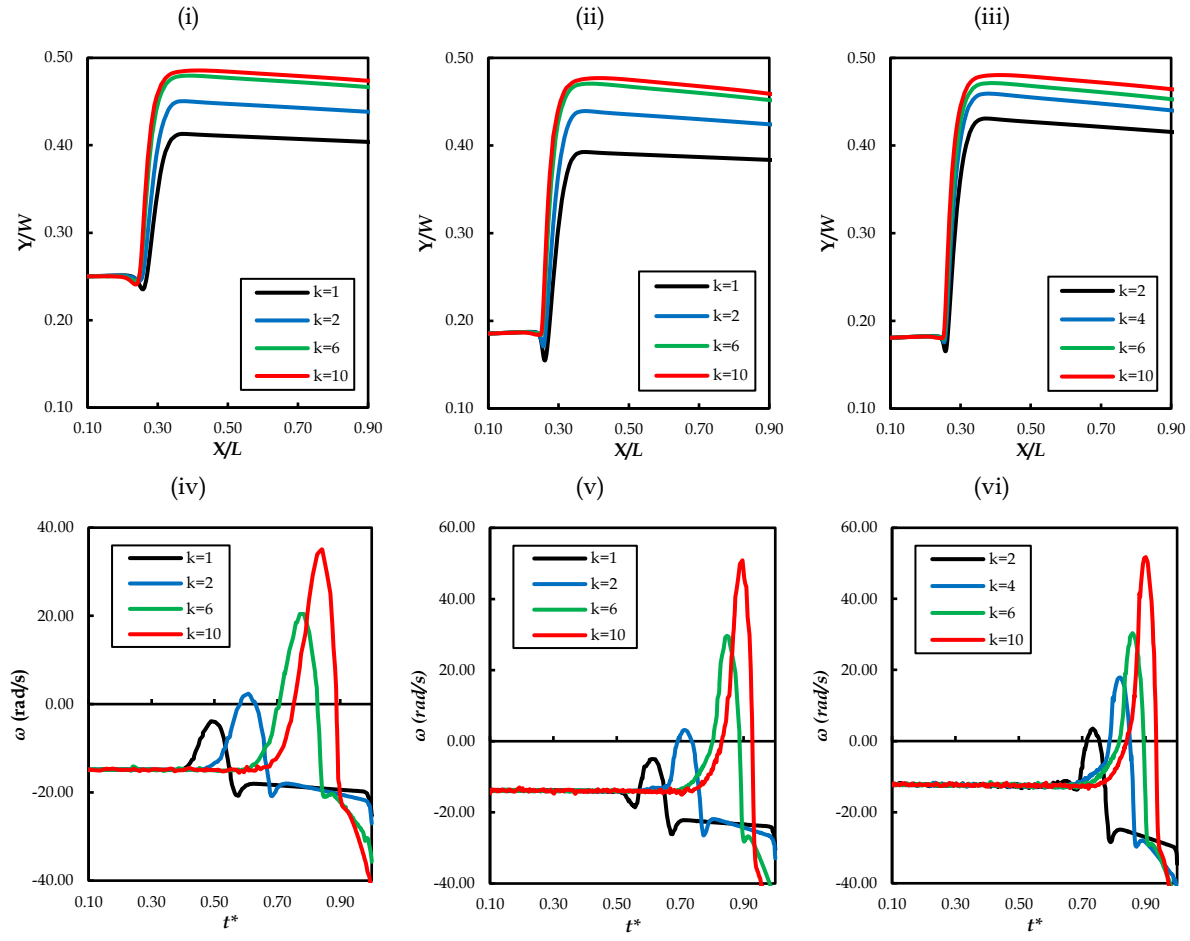

Figure 3.6 Focusing trajectories and angular velocity of a circular disk (α=1.00) for various k. The distance of the particle surface from the wall is equal with (i, iv) $a/2$, (ii, v) $a/9$ (iii, vi) $a/12$.

3.4.2 Focusing of an elliptical particle

In this Section, the HF of an ellipse, i.e., the aspect ratio, α, is greater than 1.00, is simulated. The ellipse at rest is located at ($X_{0(1)}$, $Y_{0(1)}$), far enough from the inlet boundary, S_{sa}, where the flow is fully developed. We assume that the density ratio is λ=1.059. In Figure 3.7 (i), snapshots of an elliptical particle (α=1.50) are presented for time step Δt=0.04s. The particle is initially released at ($X_{0(1)}$, $Y_{0(1)}$) = (W, $W/6$) and angle of orientation $\theta=\pi/4$. The flow ratio is k=5. Figure 3.7 (ii) shows the orientation and snapshots for time step Δt=0.02s. For $t^* \leq 0.3$, the ellipse moves close to the wall channel and rotates clockwise. As it enters the focusing area, the orientation abruptly changes due to uneven hydrodynamic forces. In particular, the flow from the closest channel forces the particle to reverse rotation and to move closer to the axis of the main channel. Figure 3.8 shows the streamlines as the ellipse enters and exits the focusing area. The streamlines far from the ellipse are identical. However, the flow in the vicinity of the ellipse is significantly affected by its motion.

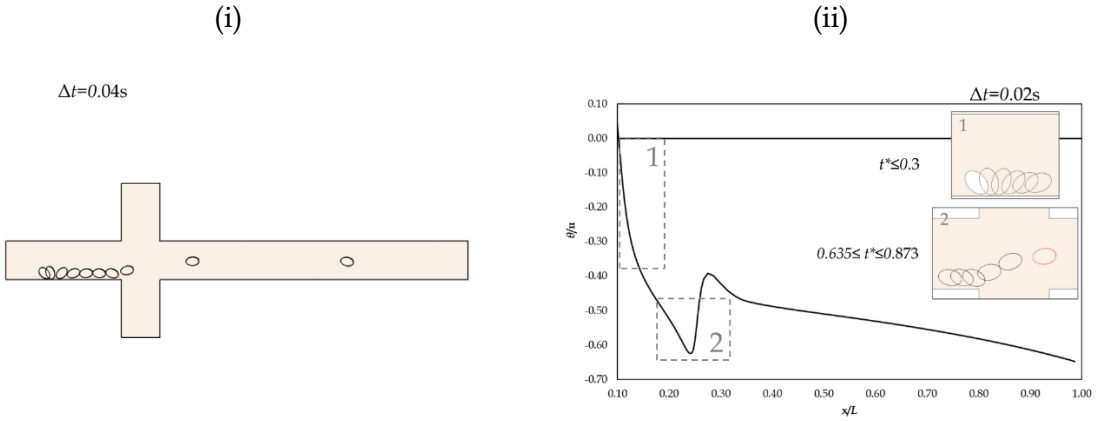

Figure 3.7 Focusing of an ellipse initially released at $Y_{0(1)}$ =W/6 and angle of orientation θ=π/4 (white infill). The flow ratio is k=5. (i) Snapshots for time step Δt=0.04s (ii) Orientation and snapshots for time step Δt=0.02s.

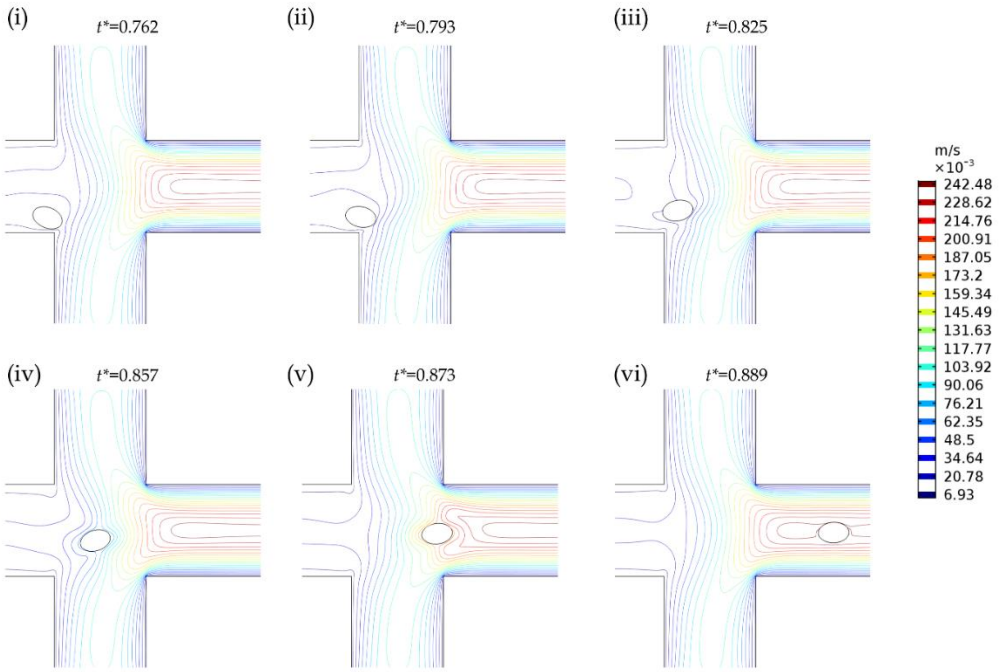

Figure 3.8 Streamlines as the ellipse enters and exits the focusing area.

In Figure 3.9, the trajectories and the orientations of an elliptical disk (α=1.50) are presented. The ellipse is initially released at three positions ($Y_{0(1)}$ =W/2, W/4 and W/6), and angle of orientation θ=π/4. For $Y_{0(1)}$ =W/2, the position of the moving disk slightly changes, while it rotates clockwise. Both position and angle of orientation are stable after the focusing

area. Depending on the ratio k, the center of the disk changes and moves close to the channel axis. Figure 3.9 (ii, v) and (iii, vi) shows the cases where the ellipse is released at $Y_{0(1)} = W/4$ and $W/6$. The final position of the disk is closer to the channel axis, as the value of k increases. After a certain point and all the way to the outlet, the position, $Y_{0(1)}$, of the disk slightly changes (less than 3%). The change of orientation with axial distance with the ellipse being initially on the axis is drastically different than that with the ellipse being initially off the axis. The final orientation of the ellipse is more stable, as k decreases.

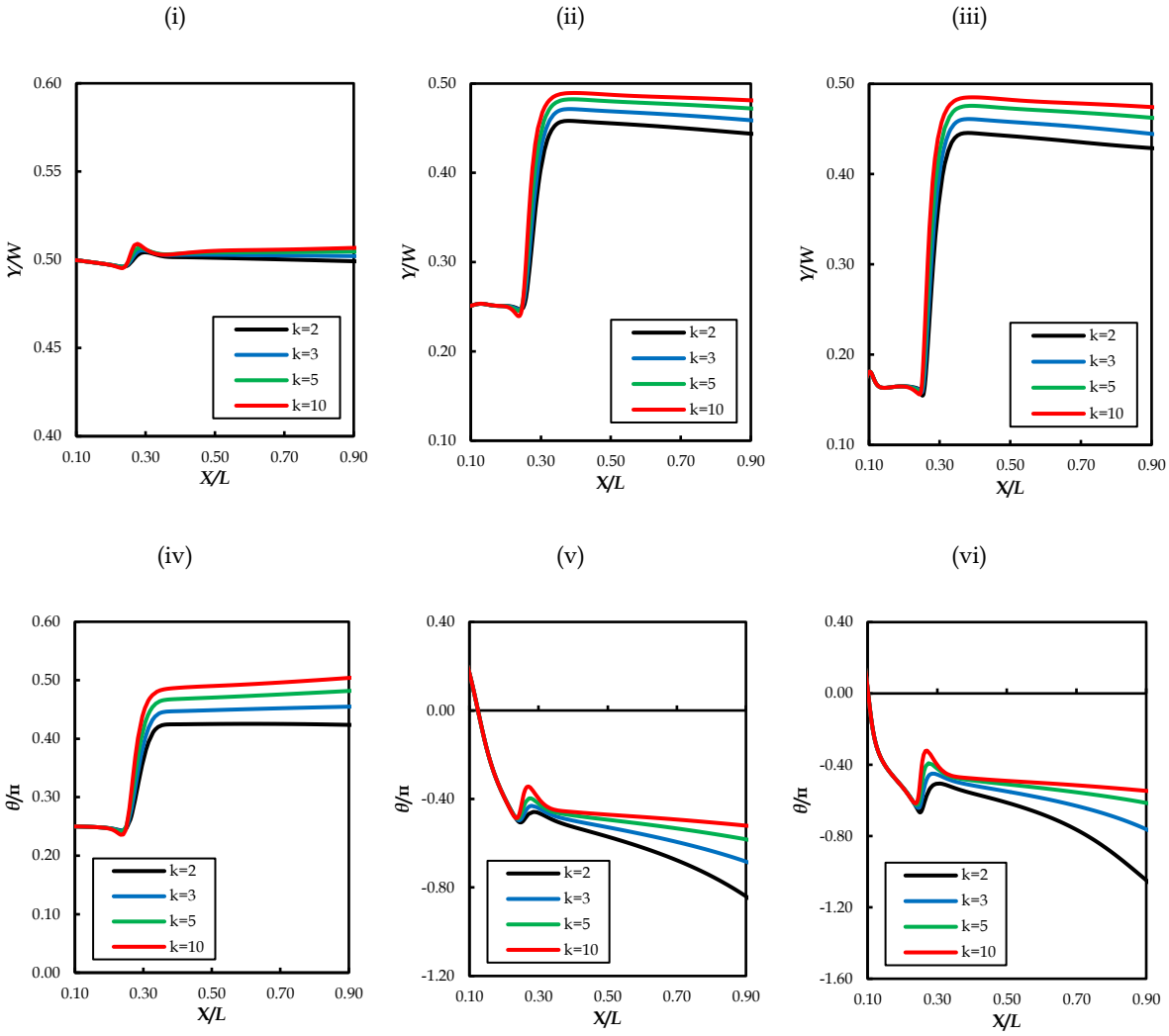

Figure 3.9 Focusing trajectories and orientation of an ellipse (α=1.5, θ=π/4) for various k initially released at $Y_{0(1)}$ equal with (i, iv) $W/2$, (ii, v) $W/4$ (iii, vi) $W/6$.

3.4.3 Focusing and separation of two particles

In this Section, we investigate the focusing and separation of two circular disks (α=1.00, β=6.00, λ=1.250) and of two elliptical disks (α=1.33, β=6.00, λ=1.059). Initially, we present the separation of two identical circular disks that are released, on the axis, at ($X_{0(1)}$, $Y_{0(1)}$)=(W, W/2) and ($X_{0(2)}$, $Y_{0(2)}$)=(W+D_0, W/2), where D_0 the initial distance of the centers of the particles. Simulations are conducted for five values of D_0 and various values of k and the final distance between the disks, D, is calculated. The final distance versus nondimensional time, t^*, is presented in Figure 3.10 (i). In all cases, the disks drift apart significantly due to the sheath flows. The nondimensional distance between the disks, $D^*=D(t)/a$, is stable after a certain time (t^*>0.8 for all cases). As the flow ratio increases, the final distance between the disks increases as well. The dependence of the nondimensional final distance $D^*(t$=T) on k is shown in Figure 3.10 (ii) for various initial positions. The distance $D^*(t$=T) is seen to display a linear scaling with the flow rate (R^2>0.99). For instance, the final distance is equal with twenty times the radius of the disk for k=6 and D_0=7a/3.

Then, we perform a similar set of simulations in order to separate two identical elliptical disks. For convenience, the initial orientation is θ=40° and θ=-80° for the leading and the following disk, respectively. Simulations are conducted for four values of D_0 and various values of k. We observe that $D^*(t$=T) increases with k in all cases. Moreover, the regression analysis reveals a linear relationship between $D^*(t$=T) and k (R^2>0.99). The results are presented in Figure 3.11.

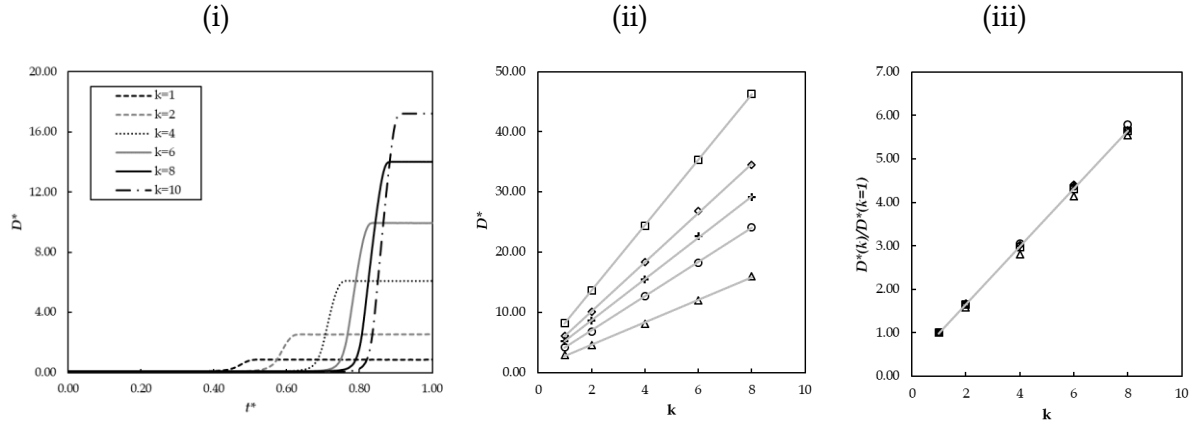

Figure 3.10 The nondimensional final distance, D^*, of two circular disks initially released on the central axis of the channel (i) at D_0=25a/12, vs. nondimensional time, t^*, (ii) at various initial distances, vs. k and (iii) replot of (ii) D^*(k)/$D^*(k$=1) vs. k. The symbols in (ii) and (iii) are: □ $D_0=a$,◇ $D_0=a/2$, + $D_0=a/3$, ○ $D_0=a/5$, △ $D_0=a/12$.

(i) (ii) (iii)

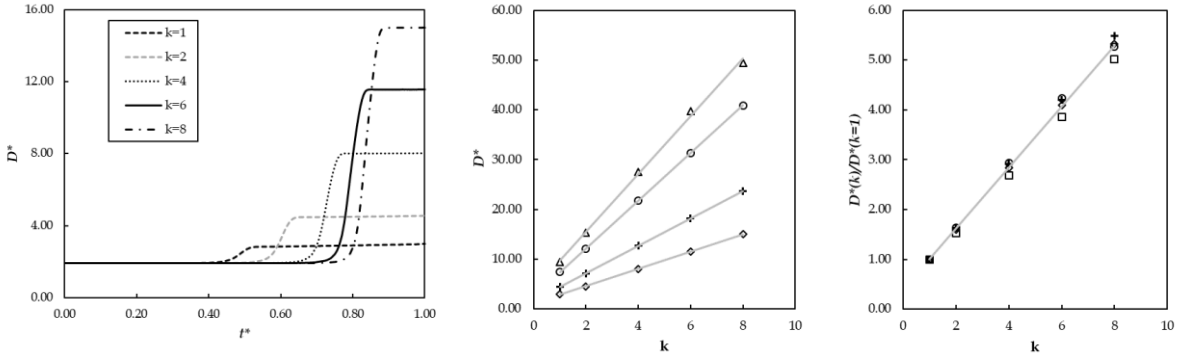

Figure 3.11 The nondimensional final distance, D^*, of two elliptical disks initially on the axis of the central channel (i) at D_0=1.9a, vs. nondimensional time, t^*, (ii) at various initial distances, vs. k and (iii) replot of (ii), D^*(k)/D^*(k=1) vs. k. The symbols in (ii) and (iii) are: ◇ D_0=1.9a, + D_0=2a, ○ D_0=2.5a, △ D_0=3a.

Next, we investigate the focusing of two identical circular disks and of two elliptical disks that are released off the axis of the central channel at ($X_{0(1)}$, $Y_{0(1)}$)=(1.5W-Dx/2, (W-Dy)/2) and ($X_{0(2)}$, $Y_{0(2)}$)=(1.5W+Dx/2, (W+Dy)/2), respectively, where Dx=4a/3 and Dy=(D_0^2-16a^2/9)$^{1/2}$. Simulations are conducted for different D_0 and various values of k and the distance between the disks, D, is determined. The trajectories of the two disks for D_0=7a/3, k=2 and k=8 are presented in Figure 3.12 (i). After a certain time, the particles move and stay close to each other and to the axis of the central channel. They move faster and closer for k=8 than k=2. Snapshots of initial and final position of the particles are shown in Figure 3.12 (ii) and (iii). The dependence of the nondimensional final distance between the disks, D^*, on k is shown in Figure 3.13 (i). In all cases, the disks significantly drifted apart due to sheath flows. For all cases and t^*>0.8 the nondimensional distance, D^*, is stable. Moreover, the regression analysis presented in Figure 3.13 (ii) reveals a linear relationship between D^*(t=T) and k (R^2>0.99).

Then, a similar set of simulations is conducted in order to separate two identical elliptical disks. The initial orientation is θ=40^o and θ=-80^o for the leading and the following disk, respectively. Simulations are conducted for four values of D_0 and various values of k. Figure 3.14 (i) shows the nondimensional final distance, D^*, of two elliptical disks released off the axis of the central tube at D_0=7a/3, vs. t^*. According to our results, D^* increases with k in all cases. We observe that there is a linear relationship between D^*(t=T) and k (R^2>0.99).

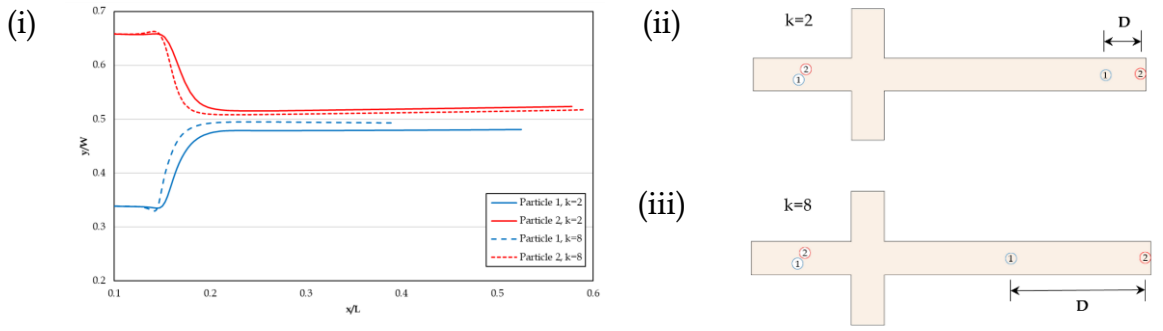

Figure 3.12 (i) Trajectories of two disks ($Y_{0(1)} \neq Y_{0(2)}$) for $D_0=7a/3$ (ii-iii) Snapshots of the initial (white infill) and final position of the two particles for two flow ratios, k.

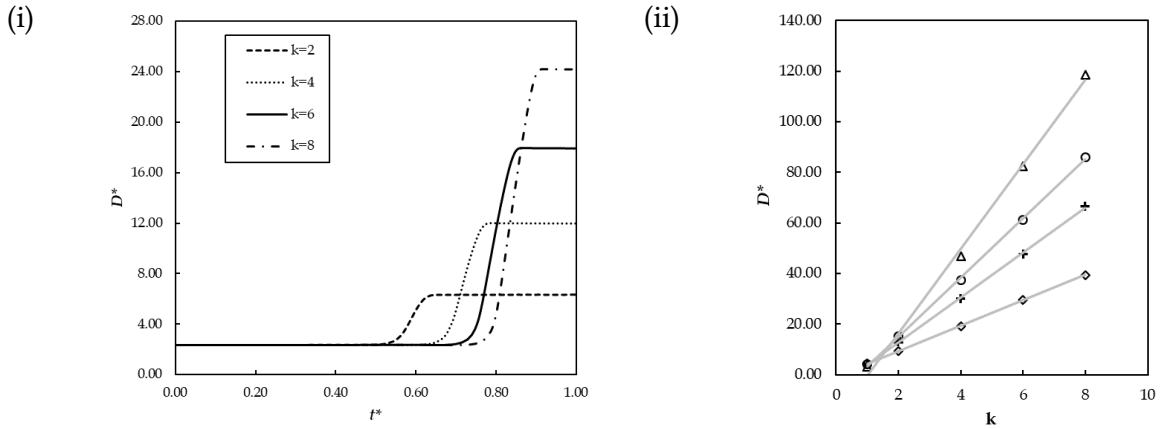

Figure 3.13 The nondimensional final distance, D^*, of two circular disks initially off the axis of the central channel (i) at $D_0=7a/3$, vs. nondimensional time, t*, (ii) at various initial distances, vs. k. The symbols in (ii) are: ◇ $D_0=a$, + $D_0=a/3$, ○ $D_0=a/5$, △ $D_0=a/12$.

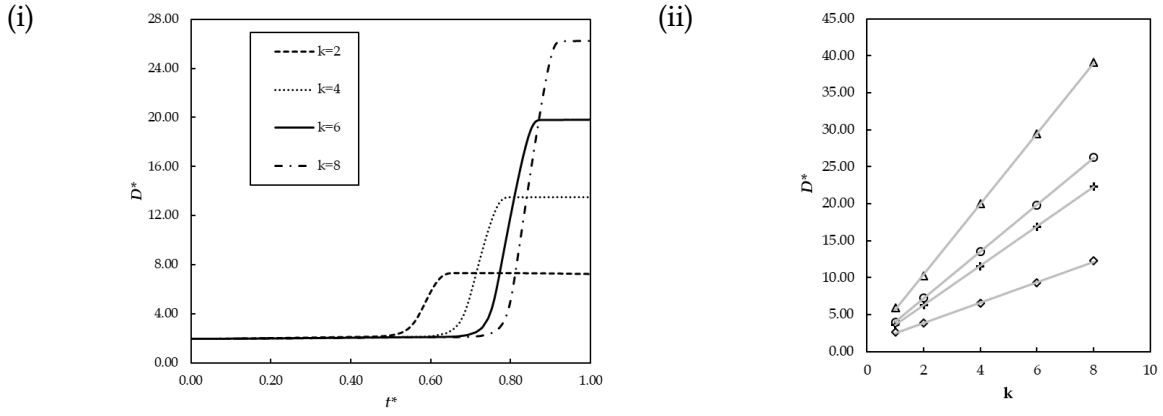

Figure 3.14 The nondimensional final distance, D^*, of two elliptical disks initially off the axis of the central channel (i) at $D_0=2a$, vs. nondimensional time, t^*, (ii) at various initial distances, vs. k. The symbols in (ii) and (iii) are: ◇ $D_0=1.75a$, + $D_0=1.9a$, ○ $D_0=2.0a$, △ $D_0=2.5a$.

3.4.4 Focusing of a group of particles with different shapes

In this Section, we consider the focusing and separation of multiple particles that are initially at rest and located far enough from the inlet boundary. The aim of this Section is to get an idea of grouping behavior of moving particles in a HF domain. To that end, we performed simulations of multiple particles based on different configurations and scenarios. In all simulations, the density ratio is λ=1.059. Simulations are conducted for k=4 and the final distance between neighboring disks, $D_{(i,i+1)}$, is calculated.

Initially, we investigate the effect of the number density of the sample fluid, i.e., number of islets per fluid volume, by spacing the particles according to two configurations. We denote them as configuration A and B corresponding to lower and higher density, respectively. The configurations are elaborated in Appendix A.4. The four circular disks are identical (α=1.00, β=6.00). The initial distance, $D_{0(i,\,i+1)}$, is equal to 2.2a. The evolution of HF of the disks for configuration A is depicted in Figure 3.15. Figure 3.16 shows the nondimensional final distance, $D^*_{(i,\,i+1)}$, between neighboring circular disks in respect to t^*. For configuration A, the final distance between neighboring disks, $D_{(1,2)} \approx D_{(2,3)} \approx D_{(3,4)}$, is approximately equal to 11a. On the contrary, the final distance, $D_{(i,\,i+1)}$, is not the same for all (i, i+1) pairs in configuration B. The initial configuration affects the final distance. The results indicate that a more thorough investigation is needed; however, it is beyond the scope of this Chapter.

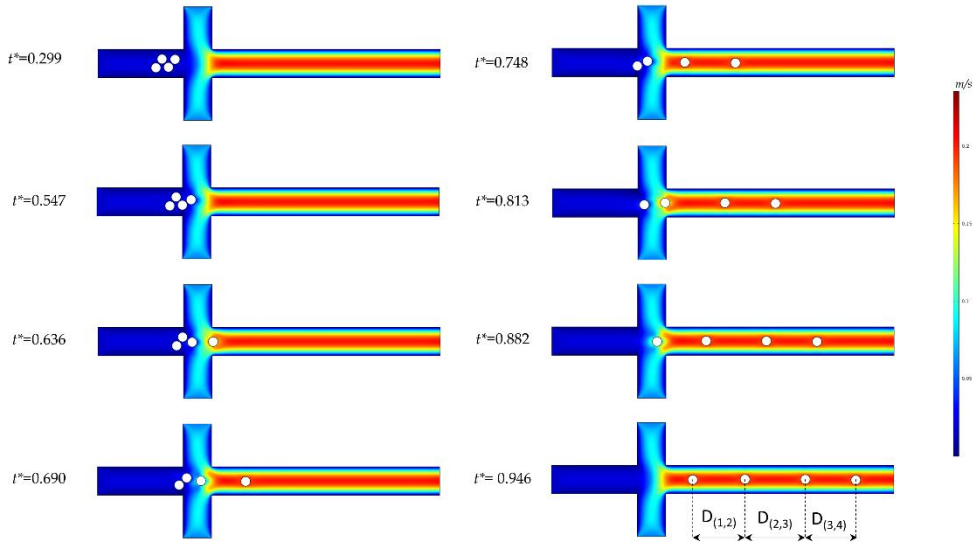

Figure 3.15 Evolution of the focusing and separation of circular disks (α=1.00, β=6.00) for configuration A.

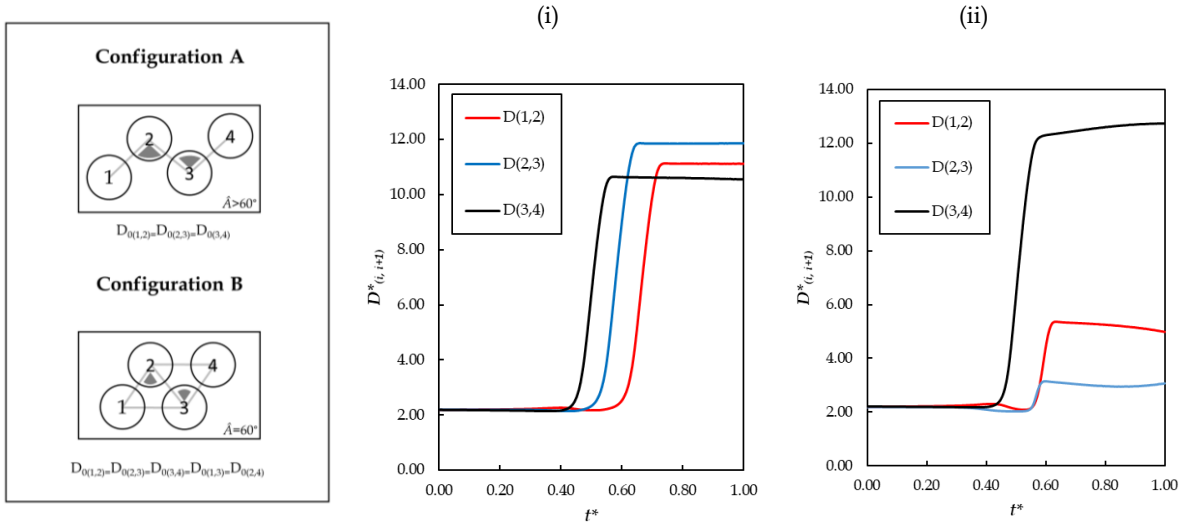

Figure 3.16 The nondimensional final distance, $D^*_{(i,\,i+1)}$, between neighboring circular disks in respect to nondimensionalized time, t^*, for (i) configuration A and (ii) configuration B.

Then, we present the simulation of four disks of various size and shape. For simplicity, we consider only the configuration B, where all the particles are equally spaced, and the initial orientation is chosen appropriately for α>1.00. Initially, we simulate the HF of four identical circular disks (α=1.00) for various blockage ratios (Scenario 1: β=5.00, 6.00, 7.50, 9.00 and

10.50), i.e., different radii of the disks. The initial distance between the centers of the neighboring disks, $D_{0(i,\ i+1)}$, is equal to 11a/5. The results in Figure 3.17 (i) reveal that the nondimensional final distance, $D^*_{(i,\ i+1)} = D_{(i,\ i+1)}/a$, between neighboring disks increases in every case. Figure 3.17 (i) shows the nondimensional final distance, $D^*_{(i,\ i+1)}$, in respect to blockage ratio. For β>7.50, the final distance between particle 1 and particle 2, $D_{(1,\ 2)}$, and between particle 2 and particle 3, $D_{(2,\ 3)}$, is approximately constant. In contrast, the effect of blockage ratio on the distance between particle 3 and particle 4, $D_{(3,\ 4)}$, is significant. For β=5.00, $D_{(3,4)}$ is thirty times the radius of the disk, while for β=10.50 it is less than ten times. Lastly, we simulate the focusing of four disks with a variety of shapes based on different scenarios. The disks are released as in the previous set of simulations. Here, the initial distance between the centers of the neighboring disks, $D_{0(i,\ i+1)}$, is equal to 2a, where a is the maximum radius for each scenario. We perform the simulation by altering the major radius of the elliptical disks (Scenario 2: α_1=1.33, α_2=1.15, α_3=1.25, α_4=1.45) in order to investigate the effect of the aspect ratio. Figure 3.17 (ii-iv) show that the nondimensional final distance, $D^*_{(i,\ i+1)} = D_{(i,\ i+1)}/\bar{a}$, between neighboring disks increases and all particles drift apart. To gain more insight on particle size effect, we perform simulations with circular disks with smaller (Scenario 3: β_1=7.00, β_2=6.00, β_3=8.00, β_4=8.50) and larger radius (Scenario 4: β_1=5.50, β_2=5.00, β_3=4.50, β_4=6.00). The results from both scenarios indicate that the final separation distance $D_{(1,\ 2)}$, and $D_{(2,\ 3)}$ is approximately constant. In addition, $D_{(3,\ 4)}$ is thirty times the mean radius of the disks in Scenario 3, while it is less than ten times in Scenario 4. However, the intermediate particles (2-3) are not distinctly separated in both cases.

(i) **Scenario 1:** Various blockage ratios

β=5.00, 6.00, 7.50, 9.00 and 10.50

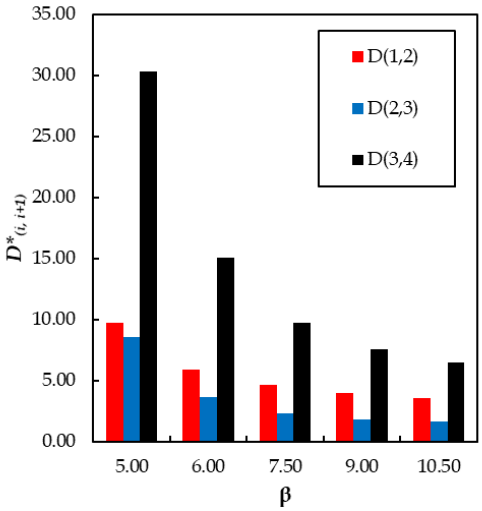

(ii) **Scenario 2:** Elliptical disks

α_1=1.33, α_2=1.15, α_3=1.25, α_4=1.45

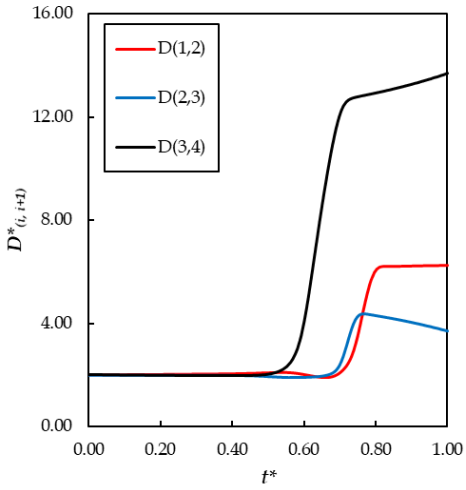

(iii) **Scenario 3:** Small circular disks

β1=7.00, β2=6.00, β3=8.00, β4=8.50

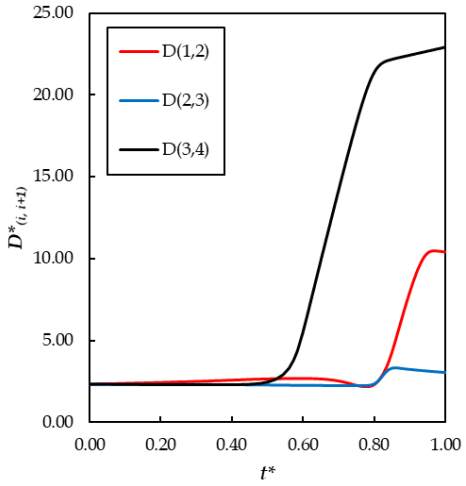

(iv) **Scenario 4:** Large circular disks

β_1=5.50, β_2=5.00, β_3=4.50, β_4=6.00

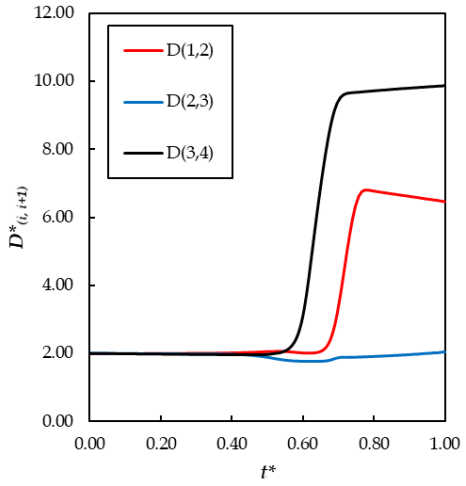

Figure 3.17 Focusing of four disks of various size and shape (i) The nondimensional final distance, $D^*_{(i,\,i+1)}$, versus to blockage ratio. (ii-iv) The distance, $D^*_{(i,\,i+1)}$, vs. t^*, for particles of different shape. In all cases, configuration B is considered.

3.5 Summary and Conclusions

In this Chapter, we presented a computational model to simulate the motion of particles in a HF configuration serving as a feeding system in our microencapsulation device. In all the

earlier numerical studies of HF of microparticles, the equations for the motion of solid phase are not included into the proposed formulation. In our case, the volumetric fraction of islets is significant, and thus, the sample fluid cannot be assumed homogenous. To our knowledge, this is the first time that a numerical model can predict the translational and rotational motion of particles in a HF domain. We considered particularly the case of a two-dimensional cross-junction geometry. By performing image processing, the shape of the particles was extracted from microscopic images. The fluid and particle motion equations were solved by implementing FE formalism and the ALE moving mesh technique is employed. Having validated our methodology, we performed simulations with spherical and elliptical particles. In all cases, the effect of sheath-to-sample flow ratio, k, on separation and focusing was investigated. In this study, we characterize as hydrodynamically focused the particles of which the final position is within the limits of $Y_{f(i)}=W/2 \pm 0.15a$.

The results of numerical simulations are presented as detailed bellow:

- Spherical and elliptical particles were individually released at the entrance of the central channel of the configuration. The final position of the particle depended on the flow ratio, k. At low values of k, the final position of the particle was far from the axis of the central channel thus, the particle cannot be focused. As the flow ratio increased, the particle in its final position came closer to the central channel axis. However, there was a critical flow ratio beyond which the particle in its final position did not come any closer to the axis. At k=10, individual particles became focused irrespective of their initial position and shape.
- A pair of identical particles were released at the entrance of the main channel at various initial distances between them. In all cases, the final distance between the particles was greater than the initial one. The flow ratio determined the final distance between the particles. Even for low values of k, separation occurred. The nondimensional final distance between two particles displayed linear scaling with k. Two particles at a small initial distance between them can be separated by adjusting the flow ratio.
- In order to get an idea of grouping behavior, we performed simulations of multiple particles in different initial configurations. We observed that the initial configuration affects the final distance between every two, leading and following, particles. The results emphasize the importance of the number density of the sample fluid, i.e., number of islets per fluid volume, for proper feeding, i.e., focused and separated particles.

Chapter

4 Modeling the phenomenon of selective withdrawal in a chamber

Synopsis

In this chapter, the flow generated by selective withdrawal in an apparatus for micro-encapsulation of pancreatic islets is studied through computational fluid dynamic simulations. The aim of the study is to identify the effect of varied design and function parameters on the phenomenon of selective withdrawal pertinent to efficient pancreatic islet microencapsulation. Contrary to previous studies that simplify the problem by approximating feeding and withdrawal tubes as a doublet of a point mass source and sink, respectively, the model presented here employs a detailed geometry. The computational model was validated with experimental data. Numerical results shed light on the dependence of the shape of the interface on flow, geometry and physical parameters. These observations can contribute to the design of an encapsulation apparatus that considers the polydispersity in size and the diversity in shape of the islets.

4.1 Introduction

Selective withdrawal has already found applications in the field of water quality control [36], igneous geology of volcanic eruptions [37], and more recently, biomedical science [38]. It is the draining of one of two immiscible fluids from two horizontally-stratified layers through a tube with its tip in the layer of the draining fluid, placed at a distance from the fluid–fluid interface (FFI) [39]. When fluid is withdrawn through a tube in the upper layer at low flow rates, only the upper fluid is withdrawn. As the flow rate is increased, the flow undergoes a transition in which the lower fluid becomes entrained in a spout along with the upper fluid [40]. This occurs also when the distance of the tip of the draining tube from the interface is below a critical value.

The hydrodynamic phenomenon of selective withdrawal has been investigated through experiments, analytical and numerical models. Lister considered the case of selective withdrawal from the upper layer of two stratified layers of immiscible fluids with the same viscosity with the simplest geometry possible [37]. The conclusion of the analytical solution was that the system can be described in terms of the dimensionless flow rate and dimensionless distance from the interface. The effects of surface tension were also investigated through a numerical solution which indicated that in a complete absence of surface tension no stable configuration of the interface is observed.

Cohen and Nagel [40] experimentally studied the same problem, yet, the immiscible fluids had different viscosities. The experiments showed that at sufficiently high flow rates, the interface undergoes a transition so that the lower fluid is entrained with the upper one, forming a thin steady-state spout. According to their similarity analysis, a proper capillary length was identified for the scaling of the interface profile before the transition. Furthermore, they claimed that the reduction of lower fluid viscosity causes an insignificant change in the final curvature of the hump tip. Subsequent experiments confirmed that claim and showed that scaling and similarity profiles extend to systems with different viscosity ratios [41]. Moreover, the nature of selective withdrawal was explored approaching it as a first-order hysteresis topological transition [42]. Hysteresis is observed once the spout is formed, decreasing the flow rate past a second lower transition flow and causing the spout to collapse. The results indicate that for high viscosity ratios, there is an intricate pattern of hysteresis and the spout appears distinctly different compared to patterns with low viscosity ratios. Hence,

it was claimed that independent variation of the viscosity ratio and the flow rate affects significantly the spout profile.

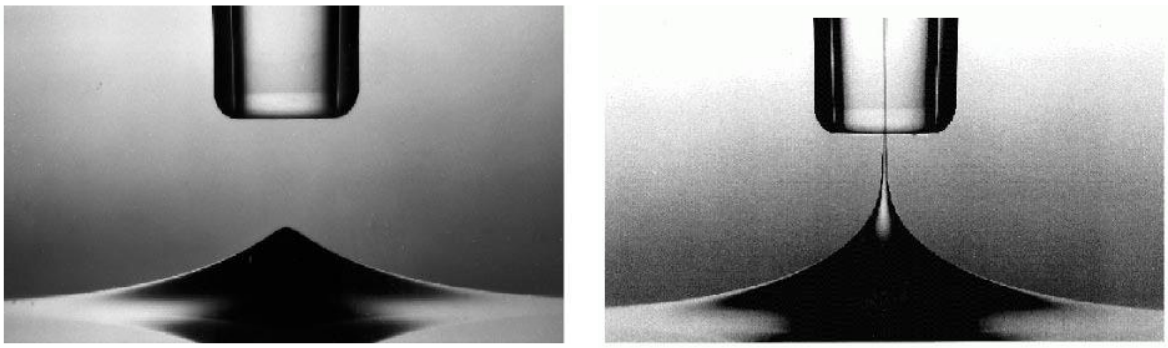

Figure 4.1 Selective withdrawal and viscous entrainment. Reprinted from [41].

Lastly, the selective withdrawal process was modeled as a physical system consisting of a point source and a point sink of equal strength, located on either side of a fluid interface [43]. To eliminate the effect of the side walls the radius of the cylindrical container was kept large compared to the distance of the singularities from the interface. The numerical results agreed with the analytical predictions for small deformation and revealed critical conditions for spout formation at large deformations. The boundary element simulations showed that, when the dimensionless flow rate was sufficiently small, the interface deformed and reached a steady shape. When the flow rate was large, the interface was no longer able to reach a steady shape and continued to evolve into a nearly cusped conical shape whose tip eventually arrived at the point sink.

4.2 Problem statement

According to our conceptual design described in Chapter 2, the employment of the hydrodynamics of selective withdrawal regime is proposed as an encapsulation method. By knowing the effect of design parameters on selective withdrawal, we can appropriately shape FFI. Design parameters include flow rates, geometric dimensions and the physical characteristics of the fluids.

The FFI can be explicitly determined through a numerical solution of the Navier-Stokes equations with appropriate boundary conditions at the interface. Numerical simulation of multiphase flow systems deals with complex material interfaces and mobile boundaries. As a result, an appropriate kinematic description of the continuum is necessary. The Lagrangian approach offers high resolution of free and fluid-fluid interfaces; however, it fails to handle large distortions without frequent remeshing. Eulerian algorithms can handle distortions more efficiently, although with lower tracking precision and flow resolution. A broadly used Direct Numerical Simulation (DNS) method is the Arbitrary Lagrangian-Eulerian (ALE) technique that combines the best characteristics of Eulerian and Lagrangian approaches. A detailed review can be found in Donea et al [44]. The ALE method has been employed for a long time to simulate fluid flows with free surfaces [45][46][44][47][48][49][39], as well as with FFIs [50][51].

In this Chapter, we simulate the case of an axisymmetric flow generated by two cylindrical tubes located on either side of the horizontal interface between two immiscible viscous liquids in a circular tank. Previous studies simplify the problem by considering a tank of infinite size in the horizontal direction and approximating the tubes as a doublet of a point mass source and a sink of equal strength [43]. The model presented here employs a detailed flow geometry of a finite-size tank with a withdrawal and a feeding tube of equal dimensions. Our scope is to identify the effect of varied design and function parameters on the phenomenon of selective withdrawal pertinent to efficient pancreatic cell microencapsulation.

4.3 Methodology

4.3.1 **Physical Model**

We consider the case of axisymmetric flow generated by two vertical equal-dimension cylindrical tubes located on either side of and at equal distance from a horizontal interface of two immiscible viscous fluid layers contained in a circular container. The lower fluid, fluid 1, drains out through the lower tube, and the upper fluid, fluid 2, discharges in through the upper tube. The density of the lower fluid is higher than that of the upper fluid, $\rho_1 > \rho_2$, resulting

in a system that is stably stratified. The interface is initially undisturbed. For this study, the interfacial tension, γ, is kept constant and equal to 0.03 N/m.

The geometry is fully defined in terms of six parameters, the radius of the container, L, the inner radius of the tubes, R, the thickness of the wall of the tubes, w, the height of the tubes, H_t, the distance of the lower tube inlet from the bottom of the container, equal to the distance of the upper tube outlet from the top of the container, H_c, and the distance of the upper tube outlet from the unperturbed interface being equal to that of the lower tube inlet from the same interface, S. Figure 4.1 shows half of the physical domain for the axisymmetric flow of interest. The values of geometry parameters are presented in Table 4.1.

Table 4.1 List of geometry parameters

Symbol	Value
L	3.20 cm
R	0.08 cm
w	0.04 cm
H_t	2.00 cm
H_c	0.40 cm

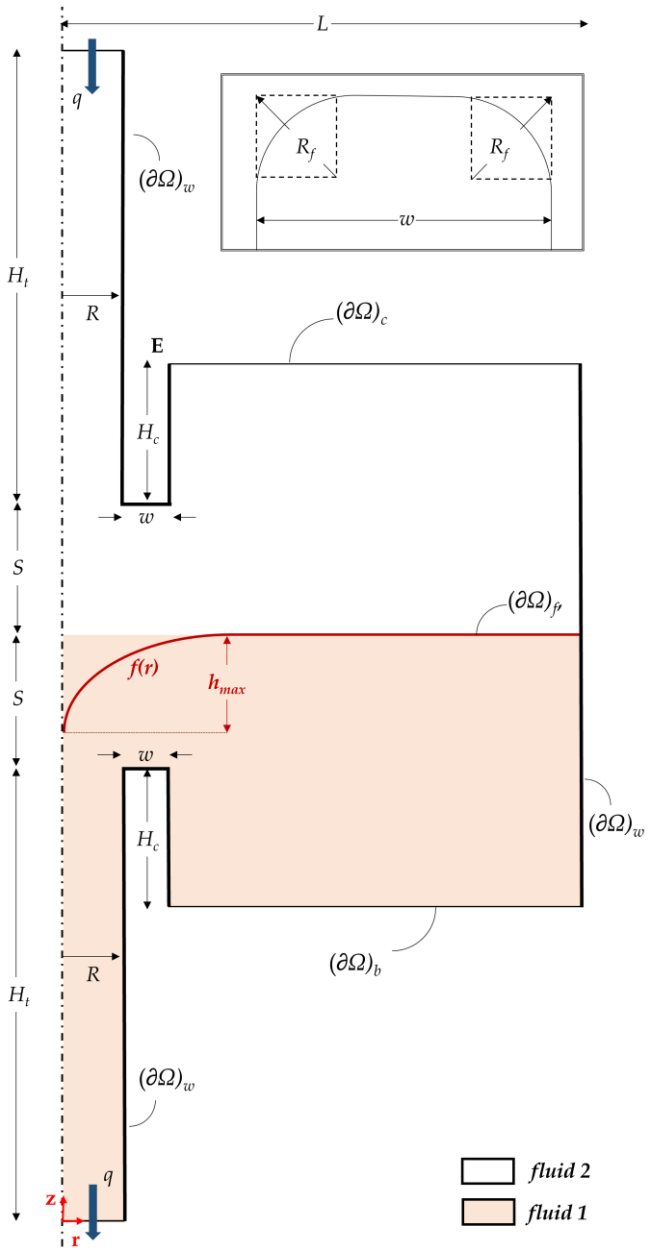

Figure 4.2 Meridian plane of the axisymmetric geometry used to model the problem of selective withdrawal in a pancreatic islet encapsulation apparatus. Inset shows the application of fillets of radius $R_f = 0.2R$ at the tube inlet.

4.3.2 Mathematical model

We denote the flow domain as Ω. We consider laminar axisymmetric flow of Newtonian incompressible fluids, which is governed by the Navier-Stokes equations and the equation of mass conservation,

$$\rho\left(\frac{\partial \mathbf{u}}{\partial t}+\mathbf{u}\cdot\nabla\mathbf{u}\right)=-\nabla p+\nabla\cdot\boldsymbol{\tau}+\rho\mathbf{g} \tag{4.1}$$

$$\nabla\cdot\mathbf{u}=0 \tag{4.2},$$

where $\boldsymbol{u}$ is the velocity; p is the pressure; $\boldsymbol{g}$ is the gravity acceleration vector; $\boldsymbol{\tau}=\mu[\nabla\mathbf{u}+(\nabla\mathbf{u})^{T}]$ is the viscous stress and μ the viscosity of the fluid.

On the boundary of the FFI, $(\partial\Omega)_f$, the kinematic and dynamic boundary conditions are:

$$\mathbf{u_1}\cdot\mathbf{n}=\mathbf{u_2}\cdot\mathbf{n}$$

$$\mathbf{n}\cdot[\mathbf{T_1}-\mathbf{T_2}]=\gamma\mathbf{n}(\nabla_t\cdot\mathbf{n})-\nabla_t\gamma \tag{4.3},$$

where $\mathbf{u}_i$ and $\mathbf{T}_i$ is the fluid velocity and the total stress tensor; $\boldsymbol{n}$ is the unit outward normal vector to the surface. The no-slip boundary condition

$$\mathbf{u}=\mathbf{u_0} \tag{4.4},$$

where $\mathbf{u}_0$ is the velocity of the boundary, is implemented on the tube walls and the side walls of the container, $U(\partial\Omega)_w$, the inlet, $(\partial\Omega)_{in}$, and the outlet boundary, $(\partial\Omega)_{out}$. On $U(\partial\Omega)_w$, the velocity is zero, i.e., $\mathbf{u}_0 = 0$. At the inlet, $(\partial\Omega)_{in}$, and the outlet, $(\partial\Omega)_{out}$, the velocity is specified as $\mathbf{u}_0=(u_r, u_z)=(0, -q/\pi R^2)$. At the container ceiling, $(\partial\Omega)_c$, the pressure is zero (p_0=0 Pa) and at the bottom, $(\partial\Omega)_b$, the pressure is $p= p_0 + (\rho_1 g+\rho_2 g)(S+H_c)$. This specification is necessary to keep the unperturbed interface at a fixed height, S.

The axisymmetric interface can be approximated by an equation of the form $z = f(r)$ and the mean curvature, $\mathcal{H}$, at any of its points can be calculated from the equation

$$2\mathcal{H}=\frac{f''(r)}{[1+(f'(r))^2]}+\frac{f'(r)}{r[1+(f'(r))^2]^{1/2}} \tag{4.5},$$

where $f'(r) = df/dr$ and $f''(r) = d^2f/dr^2$. The mean curvature, κ, at $r = 0$, provided that $f'(0) = 0$, can be calculated by taking the limit of Eq.(4) as $r\rightarrow 0$ and is $\kappa = \mathcal{H}(0) = f''(0)$.

We define a pair of nondimensioanal numbers to characterize the flow. Following Ref. (Zhou and Feng, 2010), we introduce a capillary number, and following Ref. (Hatziavramidis and Pozrikidis, 2008) we introduce the Bond number, respectively, as:

$$Ca=\frac{\mu_1\rho}{\gamma R^2}\ and\ Bo=\frac{\Delta\rho g R^2}{\gamma} \tag{4.5, 4.6},$$

where g the gravity acceleration and $\Delta\rho$ the density difference of the two liquids, $\rho_1-\rho_2$. The capillary number, Ca, and the Bond number, Bo, represent the relative importance of viscous forces and gravitational forces, respectively, as compared to surface tension forces.

4.3.3 Computational Method and Validation

4.3.3.1 Numerical Method

Numerical simulations are carried out using the commercially available software COMSOL Multiphysics™. The governing equations are solved by implementing Finite Element (FE) formalism on a triangular mesh T_h, where h_{mesh} is the typical mesh size. Due to the motion of the FFI, the mesh moves and deforms at every time step, t_{n+1}, and it is recreated by employing the ALE moving mesh technique. The mesh displacement in the interior of the fluid domain is computed by solving a Laplace equation assuring smooth variation [48]:

$$\nabla \cdot (k^{e} \nabla \mathbf{u_{mesh}}) = 0 \tag{4.7},$$

where k^e is the inverse of the local element volume and $\mathbf{u_{mesh}}$ is the velocity of the mesh. The Winslow smoothing method is implemented to evolve the interior mesh near the FFI [51].

Mesh-size independence of the numerical solution is checked using the traditional way of decreasing the mesh size until the solutions with two consecutive mesh sizes show no divergence. In the computations presented here, the smallest grid size is typically around $10^{-3}R$, while the mesh is refined near the interface tip and the tube inlet, as it is shown in Figure 4.3. For convergence, the unstructured triangular mesh has several elements between 154496 and 213584, depending on the container size.

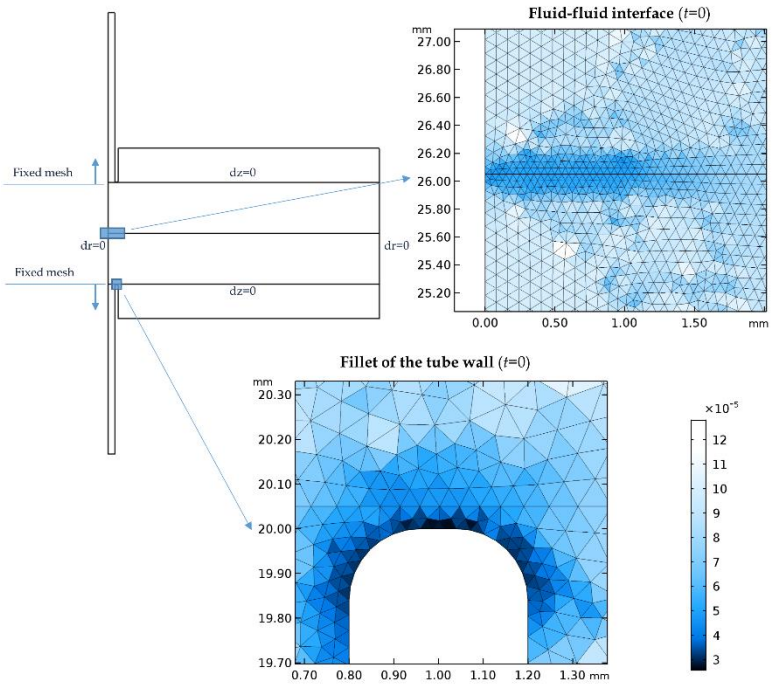

Figure 4.3 The mesh refinement at the fluid-fluid interface and the inlet of the tube (t=0).

In the event of sharp corners of the tube inlet, pressure convergence issues are raised. The convergence issues are more intense at high values of discharge-in/withdrawal-out flow rate, q. To eliminate these problems, each of the sharp corners is approximated by a fillet of radius $R_f = 0.2R$ (insert of Figure 4.2).

First, the effect of the geometric parameter ratio, L/R, is investigated. We conduct a series of simulations, for different values of $L/R \geq 30$, and we plot h_{max} as a function of κ in Figure 4.4. This figure indicates that the size of the cylindrical container does not influence the mean curvature κ, when $L/R \geq 40$. The rest of the simulations that follow are conducted for $L/R = 40$.

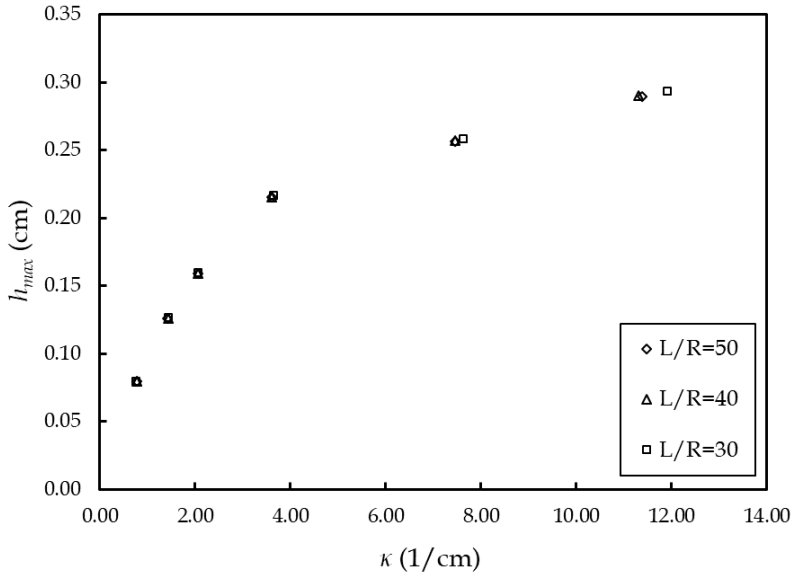

Figure 4.4 Maximum height of the hump, h_{max}, as a function of the mean curvature at the tip, κ, for different ratios L/R and q. In all cases, w/R=0.5.

4.3.3.2 Validation with experimental data

To validate the numerical model, simulations are made with the same geometry and parameter values as those used in Cohen and Nagel's study [40]. Calculated values of the mean curvature of the tip at the hump, κ, are compared to those measured in Cohen and Nagel's [40] experiments.

A hidden parameter, w/R, was found to have a significant effect on the simulation results. This parameter describes two feeding situations, (i) $w/R < 1$, feeding directly through the tube, in which case this parameter is the ratio of tube thickness to tube radius and (ii) $w/R > 1$, feeding through a hole centered on a flat plate, in which case the parameter is the ratio of the radial distance of the outer edge of the flat plate to tube radius.

To measure the mean curvature, the locations of the mesh nodes on the interface are fitted to a parabola around the tip. Figure 4.5 shows that, for $w/R = 7.5$, the simulations of this study agree well with the experimental results for different values of S, while for $w/R = 1$, agreement is only observed at the lowest values of q. The validation results indicate that the thickness of the tube wall influences the mean curvature, κ. It should be noted that no explicit

description of the withdrawal tube geometry is given in the experiments by Cohen and Nagel [40].

For the rest of this study, w/R = 0.5 is used in all cases.

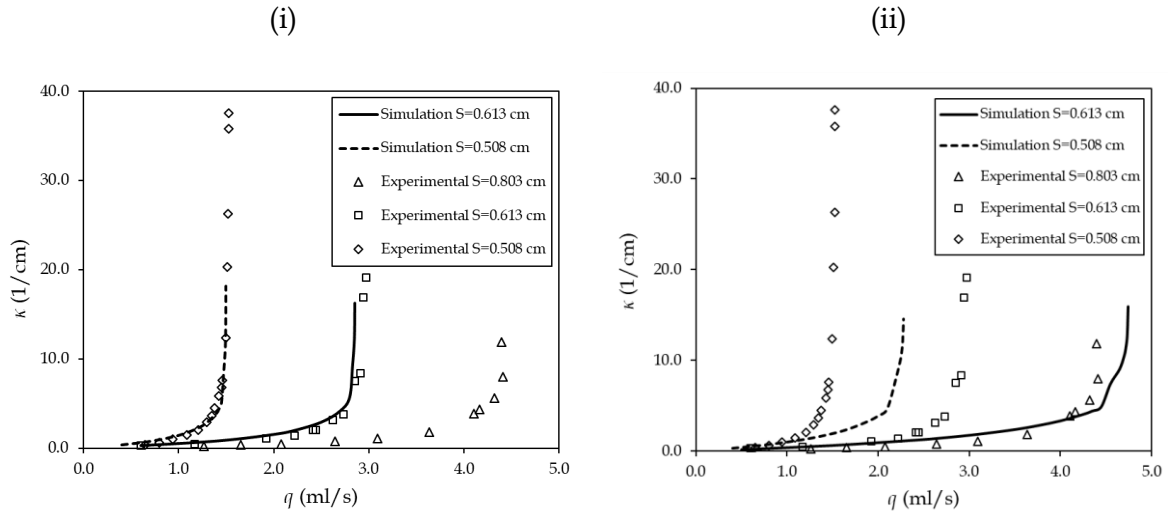

Figure 4.5 Mean curvature at the hump tip, κ, as a function of withdrawal flow rate, q, for different values of S. (i) w/R=7.5, (ii) w/R=1.

Figure 4.6 illustrates the shape of the interface at steady state from hydrodynamic and numerical analysis. In Hatziavramidis and Pozrikidis [43], small and large deformations of the interface were considered by analytical and boundary element methods. In the absence of surface tension, i.e., Bo=∞, the results for sufficiently small flow rates are in excellent agreement for both approaches. However, significant deviations occur at the lowest point of the axisymmetric depression below the point source. Using the proposed model for a tenfold decreased flow rate, all the results agree over the entire length of the interface except at the hump tip. The results of their analysis presented in Figure 4.6 are valid for equal viscosities. However, it appears that the viscosity of the two fluids has a moderate effect on the interface shape. It should be noticed that the effect is greater at the hump tip.

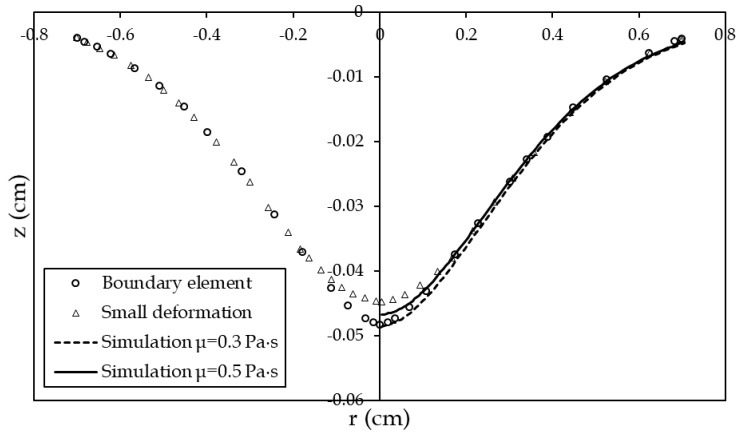

Figure 4.6 Shape of the interface occurred from hydrodynamic and numerical analysis.

4.4 Results and Discussions

4.4.1 Flow and geometry effect

The variables that control the phenomenon of selective withdrawal are the flow rate, q, and the distance of the unperturbed interface from the tube inlet, S. Simulations carried out with varying q and S determine the effect of these variables on the height and the curvature of the hump tip, h and κ, respectively. Figure 4.7 illustrates the distance h_{max} from the undisturbed interface to the tip as a function of the curvature for various flow rates q and two values of S, S=0.8 cm and S=0.7 cm. In all cases, the density ratio ρ_1/ρ_2 is 1.5 and the viscosity ratio μ_1/μ_2 is 10. One can observe two regions: (i) the region of the hump, where the curvature is low, and, (ii) the region of the cusp, with high curvature. The profiles for both values of S display a logarithmic-law divergence. As h_{max} reaches a critical value, the curvature diverges and a transition from hump to cusp occurs. The critical value of h_{max} depends on the distance S (see grey area in Figure 4.7). Similar conclusions were reached in Ref. [52]. Further increase of the

withdrawal rate causes transition from cusp to spout which may remain stable or collapse, depending on the properties of the two immiscible fluids.

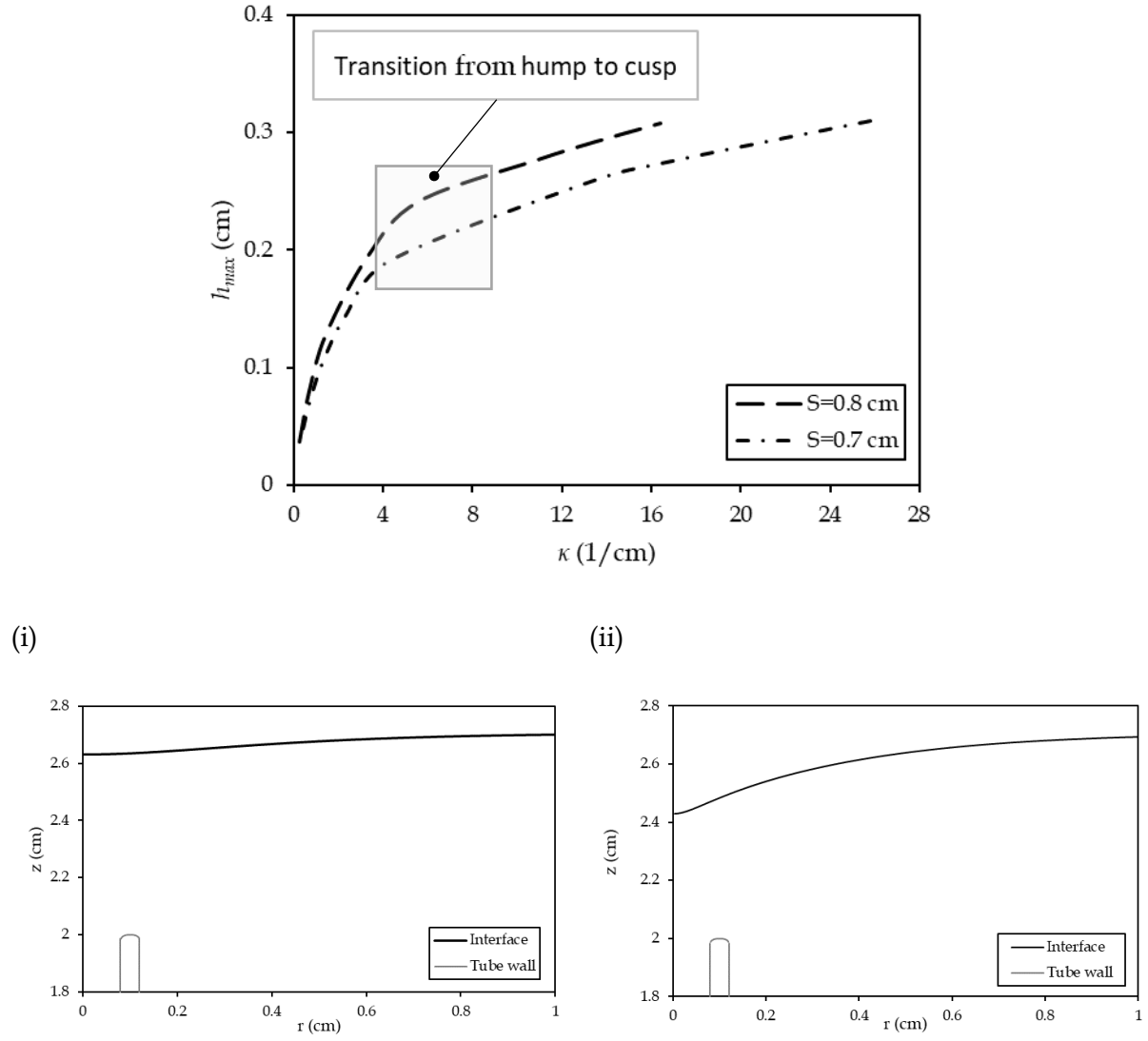

Figure 4.7 Distance of the hump, h_{max}, as a function of tip curvature, κ. Shape of (i) the hump and (ii) the cusp near the tube wall, both for S=0.7cm.

4.4.2 Viscosity and density effect

In this section, the effect of fluid physical properties, such as viscosity and density, on selective withdrawal is investigated. The two fluids are immiscible and the lower fluid is heavier resulting in a system that is stably stratified. Moreover, the lower fluid must be inert, because of exposure to laser light during the photopolymerization of the polymer coat, and nontoxic to ensure cell viability. In the micro-encapsulation device developed by Hatziavramidis [53] the upper fluid is an aqueous solution containing the polymeric precursor, and the lower fluid is a chlorinated hydrocarbon oil (Paroil-152, density=1,26 g/cm^3, Dover Chemical). Figure 7 illustrates the stable and unstable state of the FFI depending on capillary and Bond numbers. Transitions from stable to unstable state are identified by tracking the interface profile after a prolonged period. In all cases, the distance from the undisturbed interface to the tube inlet, S, is kept constant and equal to 0.8 cm.

The simulations reveal that critical conditions occur for specific density and viscosity ratio combinations, $1.03 \leq \rho_1/\rho_2 \leq 2.2$ and $1.2 \leq \mu_1/\mu_2 \leq 92$. The boundary separating stable and unstable regions is fitted by $Ca=0.227\ Bo^{0.424}$ with exceptional goodness of fit. The simulations show that the curvature, κ, increases and the maximum height of the hump, h_{max}, decreases as capillary and Bond numbers increase. In Figure 4.8, two interface profiles are illustrated for two critical conditions: (a) Bo= 5.481 and Ca=0.448 (b) Bo=0.628 and Ca=0.197. One can observe that the interface in the first plot is sharper and shorter ($\kappa^{(a)}$=8.88 cm^{-1}, $h_{max}^{(a)}$=0.49 cm), while the other in the second plot is smoother with no evolution of a cusp ($\kappa^{(b)}$=4.85 cm^{-1}, $h_{max}^{(b)}$=0.54 cm). In other words, the critical condition does not necessarily mean the evolution of a cusp.

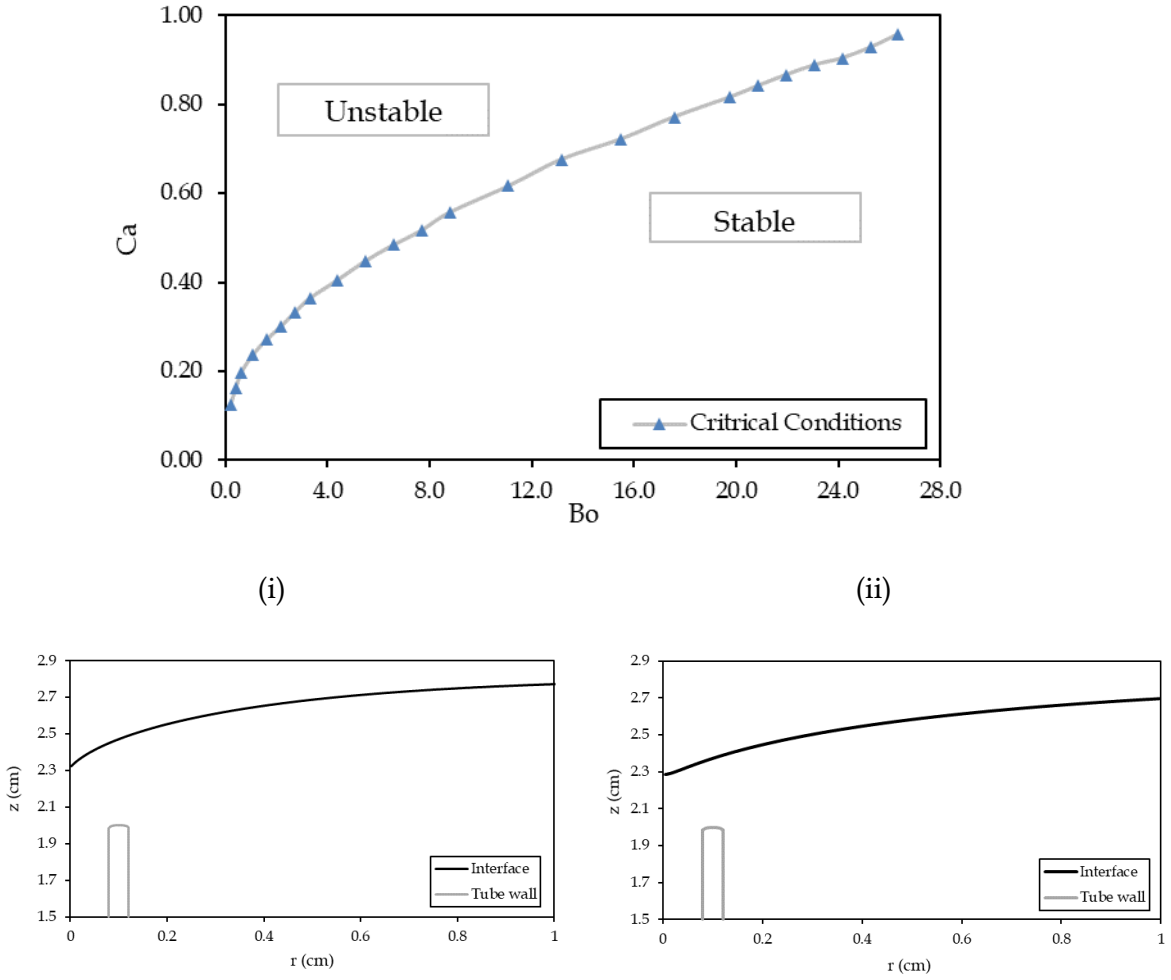

Figure 4.8 Stable and unstable FFI depending on the Ca and Bo number. Interface profiles for two critical conditions: (i) Bo= 5.481 and Ca=0.448 (ii) Bo=0.628 and Ca=0.197

4.4.3 Similarity analysis

Figure 4.9 (i) illustrates the maximum height of the hump, h_{max}, as a function of withdrawal flow rate, q, for different values of S. Increasing S causes the slope of the h_{max}-versus-q curves to become less sharp and moves the tip of the interface closer to the inlet of the withdrawal tube. Figure 4.9 (ii) shows the mean curvature at the interface tip, κ, as a function of withdrawal flow rate, q, for different values of S. As S decreases, the curves become steeper. The interface at steady state is shown in Figure 4.9 (iii). Figure 4.10 shows the time evolution of the disturbed FFI with S=0.5 cm and for q=0.325 ml/s.

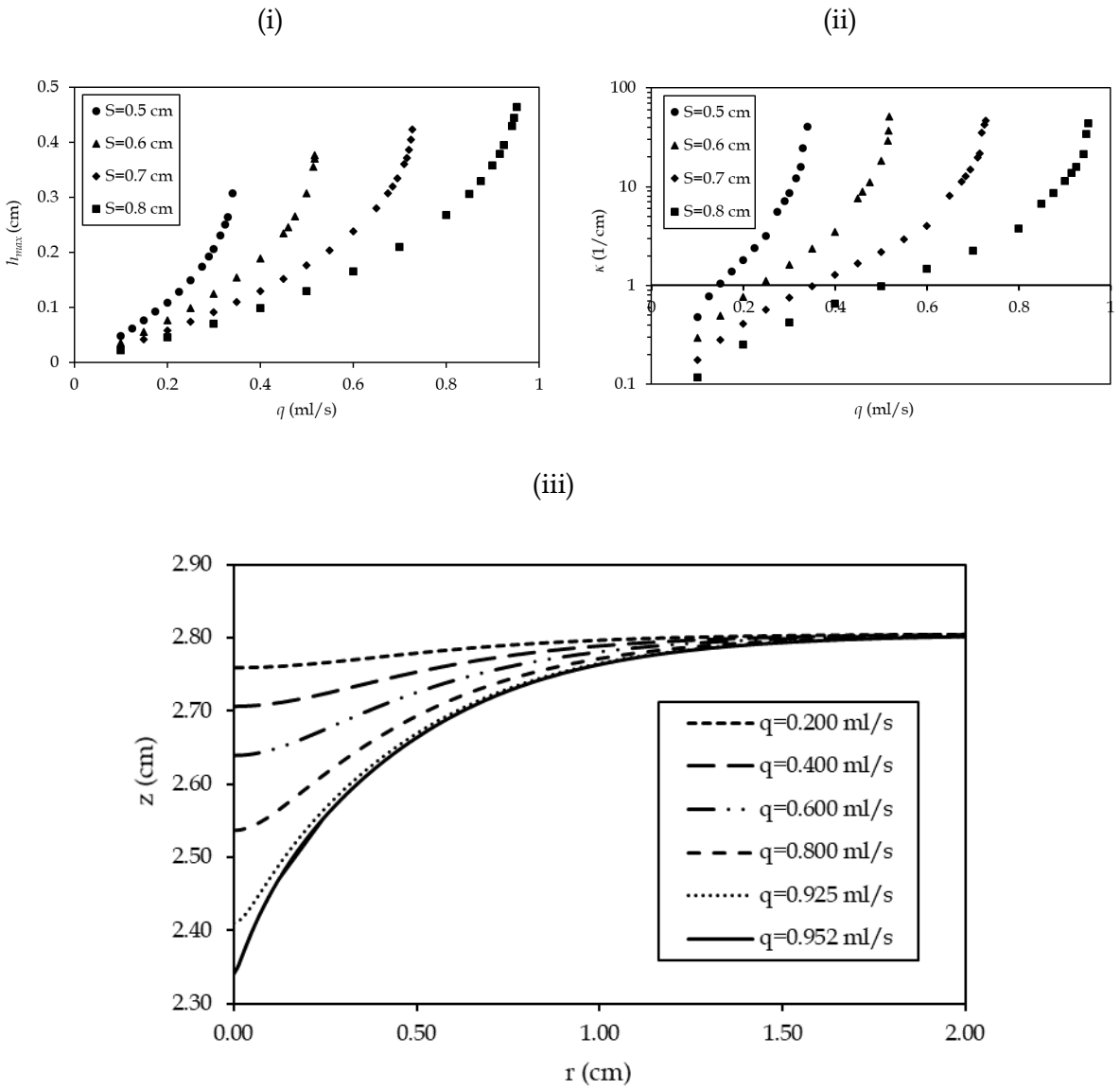

Figure 4.9 (i) Maximum height of the hump, h_{max}, as a function of withdrawal flow rate, q, (ii) Mean curvature at the interface tip, κ, as a function of withdrawal flow rate, q, (iii) Shape of the interface for varying q. S=0.8 cm in all cases.

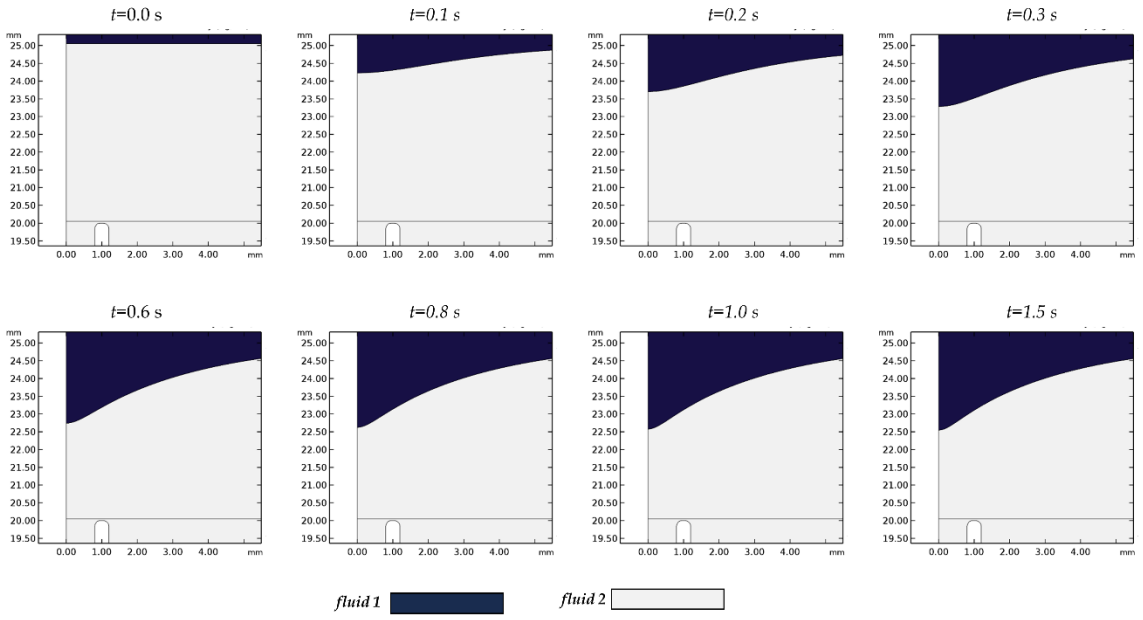

Figure 4.10 Time evolution of the disturbed interface for q=0.325 ml/s and S=0.5.

For any value of S, the h_{max}-versus-q and κ-versus-q curves display exponential-type behavior. The prefactors in the exponential expressions for both curves, c_h and c_κ, which vary slightly with S, can be used as scaling parameters. Similarly, for each value of S, a critical flow rate, Q_c, and a critical height, h_c, can be chosen as scaling parameters and the quantities $(h_c-h_{max})/(h_{max}\ c_h)$ and κ/c_κ can be plotted versus $(Q_c-q)/q$ in Figure 4.11 (i) and (ii), respectively. Q_c and h_c for each S are defined as the critical flow rate and the critical height when the transition from cusp to spout occurs. In these figures, all four data sets collapse on single curves and display a power-law divergence, as q approaches Q_c. Finally, $(h_c-h_{max})/(h_{max}\ c_h)$ versus κ/c_κ is plotted in Fig. 11, by combining the two scaling dependencies in Figure 4.11 (i) and (ii). Figure 4.12 indicates that the power law exponents are independent of S for this range of tube heights, even though the scaling parameters change slightly with S. Similar conclusions were reached by Cohen and Nagel [40].

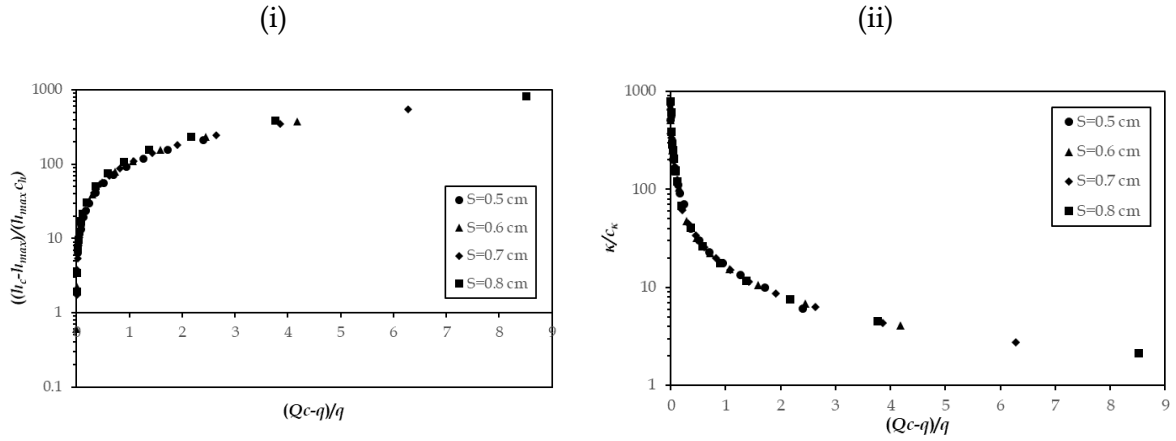

Figure 4.11 Scaling for the height h_{max} and for the hump mean curvature κ. (i) $(h_c-h_{max})/(h_{max}\, c_h)$ versus $(Q_c-q)/q$, (ii) κ/c_κ versus $(Q_c-q)/q$.

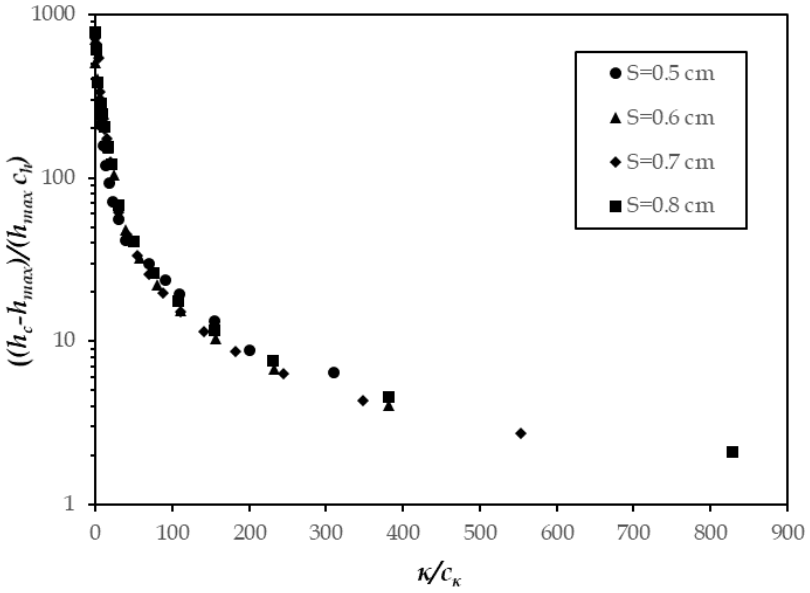

Figure 4.12 Combining the two scaling dependencies in Fig. 9a and 9b, results in a plot $(h_c-h_{max})/(h_{max}\cdot c_h)$ vs. κ/c_κ.

4.5 Summary and Conclusions

An axisymmetric laminar flow, generated by two vertical equal-dimension cylindrical tubes located on either side of and at an equal distance from the horizontal interface separating two immiscible viscous fluid layers contained in a circular container, is considered. The governing equations are solved numerically using a traditional FE method to resolve the flow and an ALE method to track the movement and deformation of the FFI.

The results of numerical simulations are presented below:

- When $L/R \geq 40$, the most important parameter is the ratio of tube wall thickness to radius, w/R. This hidden parameter was found to have a significant effect on the simulation results. This parameter describes two feeding situations, (a) $w/R < 1$, feeding directly through the tube in which case this parameter is the ratio of tube thickness to tube radius and (b) $w/R \geq 1$, feeding through a hole centered on a flat plate, in which case the parameter is the ratio of the radial distance of the outer edge of the flat plate to tube radius.
- The simulations show that, as the withdrawal flow rate q increases or the initial distance of the unperturbed interface from the tube inlet, S, decreases, the hump tip moves closer to the tube inlet and transitions to a cusp at a critical q or a critical S, depending on which of the two variables is changing. When transition from hump to cusp occurs, the maximum distance from the unperturbed interface, h_{max}, reaches a critical value and the curvature diverges.
- The simulations reveal that the curvature increases and the h_{max} decreases by increasing both capillary, Ca, and Bond, Bo, numbers. Furthermore, the transition from hump to cusp does not occur for every critical condition. The evolution of the cusp occurs only for a range of viscosity and density ratios and the transition from a hump to a cusp is dominated by gravitational and viscous forces. By increasing the capillary number and keeping the Bond number stable, the hump becomes sharper and the maximum distance from the undisturbed interface greater. By increasing the Bond number and keeping the capillary number stable, the hump becomes less sharp and h_{max} smaller. In a Bo-Ca plane, the boundary separating stable and unstable regions is fitted by $Ca=0.227Bo^{0.424}$. This mathematical formula can be used in the assessment of fluid candidates for experimental set-up.

- The mean curvature at the hump tip, κ, and the height of the hump tip, h_{max}, varies with the flow rate, q, for different distances from the unperturbed interface, S. All the h_{max}-versus-q and κ-versus-q curves display exponential-type behavior. The similarity analysis indicates that the scaled variables are independent of S for $0.5\text{cm} \leq S \leq 0.8\text{cm}$, even though the scaling parameters change slightly with S. The scaled maximum height and the curvature of the tip show divergence of power-law type as the withdrawal flow rate q approaches a critical Q_c value.

These results aim to shed light on the dependence of the shape of the interface on physical, geometry and flow parameters. The findings in this work can be used to appropriately shape the interface by controlling the phenomenon of selective withdrawal. Further insight into mechanisms related to selective withdrawal can be gained with laboratory measurements on an apparatus.

Chapter

5 Development of a 3D-printed apparatus for particle encapsulation

Synopsis

In this chapter, we report the development of an apparatus including a hydraulic pumping system by employing three-dimensional printing (3DP) technology. Despite the rapid expansion of 3DP, there is a limited number of reports in the literature demonstrating the potential contribution to encapsulation technology. By operating the 3D-printed apparatus, we experimentally investigate the encapsulation of spherical beads serving as islet surrogates.

5.1 Introduction

Various microfluidic-based medical devices have been proposed for cell manipulation, stem cell analysis, drug discovery and analysis among others [54][55]. For decades, the most preferred fabrication method was soft lithography using mainly polydimethylsiloxane (PDMS) because of its transparency and biocompatibility. Despite the advantages of PDMS, there are limitations such as its hydrophobicity and complicated fabrication process [56]. Recently, three-dimensional printing (3DP) or additive manufacturing have been applied as a promising alternative fabrication method in microfluidics. As a single step design-to-prototype process, 3DP offers the capability to accelerate the realization of a concept or even altering and redesigning any aspect of it. These technologies are offering many advantages over traditional methods regarding rapid production and non-traditional geometric structure. They particularly enable the fabrication of engineered porous structures, internal support structures and tortuous cavities. In addition, 3DP can reduce the costs associated with infrastructure, equipment and maintenance [57]. As a result, 3DP technologies have already penetrated almost every field, and is used in many chemical, pharmaceutical and biological applications [58]. Food and Drug Administration (FDA) responded to the fluorescence of 3DP in biomedical applications with guidelines regarding technical considerations for medical devices [59] made by additive manufacturing. Scientific and technological challenges of additive manufacturing is thoroughly described in a review by Tofail et al [60].

3DP refers to several technologies such as Fused Deposition Modeling (FDM), PolyJet, Stereolithography (STL), Digital Light Processing, etc. In FDM, a thermoplastic material is extruded through a high temperature nozzle on a printing platform to build a 3D structure layer-by-layer. Once the semi-fused material is solidified, the build table is lowered or the nozzle is elevated, and the next layer is deposited. FDM printers are low-cost, easy to use and compatible with a great range of thermoplastics. However, their dimensional accuracy and surface finish is compromised [61]. PolyJet technology involves spraying tiny droplets of liquid photopolymers from linearly arranged nozzles onto a build surface, where the material is immediately cured using an integrated UV light source [62]. Once the material is photopolymerized, the build platform is lowered, and the next layer is built. Its advantages include high resolution for smooth surface finish and simultaneous multi-material printing [63].

Diverse research groups have demonstrated the production of 3D-printed laboratory and analytical equipment, chemical and bioreactors, and microfluidic devices among others. Surface roughness, dimensional accuracy, build time, material and mechanical properties determine the selection of the appropriate technology. Despite the continuing improvement, the demanding expectations of microfluidic community for optical clarity and surface smoothness are not completely fulfilled [64]. Process optimization, printing orientation, post-printing surface refinement and modular design strategies [64][65] have been proposed to overcome these limitations. In addition, the need for highly biocompatible materials has triggered the development of new FDA approved materials (ISO 10993, USP Class VI). These kinds of developments and improvements will intensify the ubiquitous presence of 3DP-based microfluidics in biomedical applications.

5.2 Problem statement

Despite the rapid expansion of 3DP, there is a limited number of reports in the literature [66][67] demonstrating the potential contribution to cell encapsulation technology. In this Chapter, we report the development of a microencapsulation apparatus including a hydraulic pumping system by utilizing 3DP technology. A detailed description of the design of the apparatus is presented in Chapter 2.

In our apparatus, spherical particles serving as islet models are encapsulated by employing the hydrodynamics of selective withdrawal. The particles enter the encapsulation chamber in a file through a two-nozzle feeder with its outlet orifice above the interface of two immiscible fluids. A steady suction is applied throughout a withdrawal tube, at equal distance below the interface, so that the interface forms a steady-state cusp. Moving in the direction of the inlet to the withdrawal tube, every particle reaches the tip of the cusp, i.e., the point of the interface with the maximum depth. Depending on the physical properties and the inertia of the particle and the fluids, the particle may either float or move through the interface.

Particles passing through a fluid-fluid interface has been recently studied [68][58][69][70] as it is encountered in many engineering applications. Different behaviors of gravity-driven settling of spherical particles, moving toward a static steady-state interface, have been observed and classified. In our case, we investigate the condition for a particle to move through a dynamic steady-state interface. As the particle moves through the interface,

a volume of the upper fluid is entrained along with the particle. By controlling this fluid volume, we can control the capsule volume, hence, the thickness of the coating membrane.

By operating the 3D-printed apparatus, we experimentally investigate the encapsulation of spherical particles. We develop a hydraulic system, in order to pump the fluids and the particles into and out of the apparatus. Three inflows and one outflow are necessary to operate the apparatus. Two pumps can be used to drive the sample flow, Q_1, and sheath flow, Q_2, into the two-nozzle feeder. Hydrodynamic focusing of the particles necessitates control over the sheath-to-sample-flow ratio, $k=Q_2/Q_1$. Steady-state cusp requires a stable pulseless outflow, Q_3, that is generated from a third pump. A desired distance between the fluid-fluid interface and the tip of the withdrawal tube is maintained by activating an inflow, Q_4, equal to the withdrawal flow, Q_3.

5.3 Methodology

5.3.1 Experimental setup

The experimental setup is presented in Figure 5.1 (i-ii). The microencapsulation apparatus was placed on a horizontal platform. A two-nozzle hydrodynamic focusing is utilized to ensure feeding the individual particles in the direction to the inlet of a withdrawal tube. The encapsulation chamber is a vessel containing two horizontally stratified layers of two immiscible fluids. The particles enter the chamber in a file through a vertical tube with its outlet orifice above the interface of the two fluids. Photographs and videos were taken with a digital microscope (Dino-Lite Edge AM7115MZT; AnMo Electronics Corp., Taiwan) at 43x magnification. As regions of interest (ROIs) we define the outlet of the feed tube and the inlet of the withdrawal. The two ROIs are highlighted in Figure 5.1 (iii). In order to record them, the microscope was attached on an elevator stand that was driven by a stepper motor.

A hydraulic pumping system consisting of four pumps was fabricated to drive and control the flows. Syringe pumps were chosen as they generate more stable flows than peristaltic pumps. The pumps were equipped with disposable syringes of 10 and 20ml. Pump

1 (P1) and Pump 2 (P2) were used to drive the sample, Q_1, and the sheath flow, Q_2, into the feeder. The withdrawal flow, Q_3, was generated by Pump 3 (P3). In order to keep the interface stable, the same volume of fluid per time step was pushed back from Pump 4 (P4), i.e., $Q_4 = Q_3$. All the syringe pumps were connected to the apparatus through tubing made of a thermoplastic elastomer (PharmMed® BPT) or polyethylene. The experiments were performed in a cleanroom at steady temperature of 25 ± 1 °C. Fluids and syringes were replaced after the completion of each set of experiments.

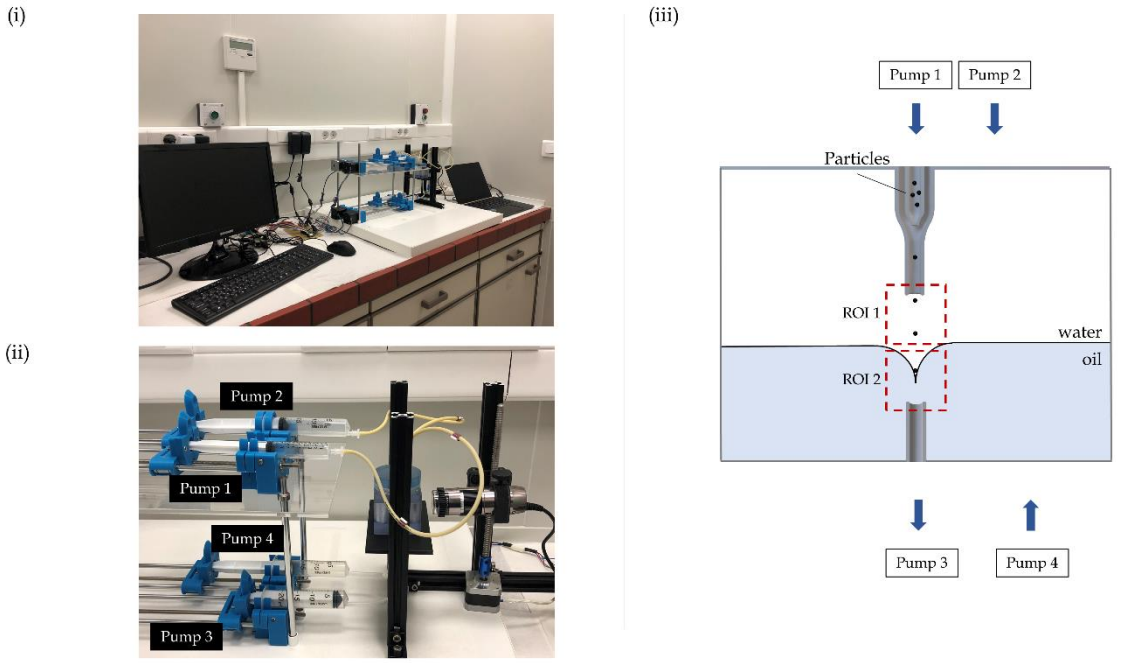

Figure 5.1 (i-ii) Experimental setup (iii) Regions of interest.

5.3.2 Design and fabrication

The Computer-aided design (CAD) drawings were made with use of Autocad™ (Autodesk Inc., CA, USA) and exported as STL files. The apparatus is designed as a construct composed of interlocking parts. Disassembling allows effectively removal of the supporting material and better surface treatment [64]. Moreover, a modular design strategy may allow the reuse of the apparatus in biomedical applications, despite repeating the sterilization process.

The main parts are the two-nozzle feeder, the encapsulation chamber, and the withdrawal tube. Figure 5.2 (ii) illustrates the interlocking parts of the apparatus. There is a

centrally located hole at the top and the bottom of the chamber acting as an inlet and an outlet, respectively. For security and sealing, three easy-to-use connection adapters were used to connect the pumps with the apparatus. The withdrawal tube is equipped with a same adapter, too. In order to prevent liquid leakage, the interlocking parts are connected by employing O-ring gaskets. Figure 5.2 (iii) shows the half cross-section of the two-nozzle feeder. As the shape of the nozzles, e.g., curvilinear or linear, has a moderate effect on hydrodynamic focusing [25], only linear-shape nozzles were designed. The internal angle of the inner and the outer nozzle are 169^{o} and 164^{o}, respectively. The inner and outer radius of the feed tube and the withdrawal tube are equal to 0.8 mm and 1.3 mm, respectively. All components were printed with Object 350 Connex 3 (Stratasys Ltd., USA). Six STL files in total were imported in GrabCAD software (Stratasys Ltd., USA) that was used to control the fabrication process. The printing orientation of the chamber was selected with the intent to enhance the transparency of the object. In addition, the printed chamber was photobleached and polished. Following the printing process, the support material was removed using a high-pressure water jet.

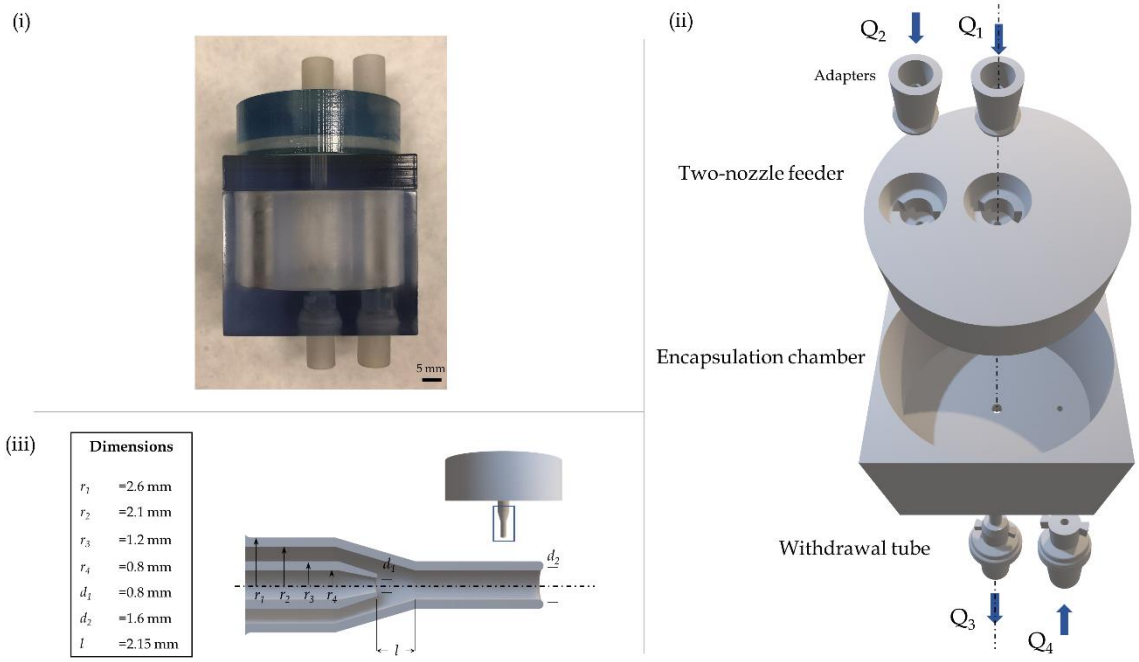

Figure 5.2 (i) The 3D-printed microencapsulation apparatus (ii) Exploded view of the apparatus as a construct composed of interlocking parts (iii) Half cross-section of the two-nozzle feeder.

The design of syringe pumps is based on an open-source design previously published [71] with minimal modifications. It has already been employed in microfluidic applications

demonstrating flow stability [72]. The plastic parts of the pumps and the setup were printed with an Ender 5 FDM-printer (Creality 3D Technology Co. Ltd, China). The printer was equipped with a 0.4 mm nozzle. Simplify3D was employed as a slicer software. The print speed was 40 mm/s and the layer height was 0.3 mm. The extruder and the build table were heated up to 210 ^{o}C and 70 ^{o}C, respectively. The interior fill percentage was 20% for the pumps and 100% for the slider and the platform. A detailed table with printing parameters is presented in Appendix B.1.

Every pump was driven by a stepper motor 42BYGHM809 with 0.9^{o} step angle, while the camera slider was driven by a stepper motor 42BYGHW208 with 1.8^{o} step angle (WanTai Motors Co., Ltd, China). Each motor was controlled by a DRV8825 stepper controller (Texas Instruments Inc, USA). All controllers were connected to two Raspberry Pi 3 single-board computers (Raspberry Pi Foundation, UK) and were driven by an open-source Python code [71] with appropriate modifications. The main loop of the code runs across the appropriate number of micro-steps for a user-input volume. At each iteration, the motor is activated for a properly calculated time interval during which a displacement of the syringe occurs. Functionality is achieved by generating a desired flow rate, i.e., a ratio of user specified volume to calculated time. The original code was designed to operate one syringe pump; thus, we merged the codes associated to (P1-P2) and (P3-P4) operation into two unified pieces of code, respectively. The first modification regarding the (P3-P4) operation, ensured that at each iteration the two pumps are activated simultaneously in reverse rotation direction. The second modification regarding the (P1-P2) operation, employed parallel threading in order to decouple the activation time of each pump. This requirement emerged from the introduction of a user-defined factor, k, which is the flow ratio Q_2/Q_1. For k>1, the flow rate of the two pumps will be different; hence, the corresponding activation time of each motor should be inversely proportional to flow rate. To this end, the main loop of each pump is run in two independent threads of the CPU of the board computer.

All pumps (1-4) were calibrated following the calibration sequence described in [71]. A specified volume of distilled water and paraffin was delivered onto an analytical balance ME204 (readability 0.1 mg) from Mettler TOLEDO (USA) in order to test the precision of the pumps. The sequence was repeated for three flow rates (0.1, 0.2 and 0.5 ml/s). In addition, we performed two tests in order to assess the performance of our pumping system and fulfil the requirements regarding the function of the apparatus. The objective of the first test is to guarantee that the volume of the oil phase does not change during the experiment. P3 and P4

were operated reversely, and we measured that the flow ratio generated from P3 is equal to the flow from P4 in terms of absolute value ($|Q_4|-|Q_3| = 0.00 \pm 0.01$ ml/s). The second test aims to ensure that the flow ratio, k= Q_2/Q_1, is kept stable during the experiment. By performing the test for different k, we observed that the flow rate slightly changes over time ($[\partial(Q_2/Q_1)/\partial t]/k = 1.00 \pm 0.05$). Small variations were identified only in low flow rates and are mainly associated with micro-stepping.

5.3.3 Materials

Three materials, two build and one support were used in the fabrication process of the apparatus. Transparent VeroClear™ resin and SUP705™ (Stratasys Ltd., USA) were used as a build and support material, respectively. VeroClear™ was selected as it enables visualization. O-ring gaskets were made out of rubber-like TangoPlus™ elastomer (Stratasys Ltd., USA). The plastic parts of the syringe pumps and the setup were fabricated of blue and black 1.75 mm polylactic acid (PLA) filament (PrimaSelect, Sweden). Al the metallic parts (screws, bolts, nuts, bearings, shafts) were made of anodized aluminium.

Two immiscible fluids were used during the experiments. In the encapsulation chamber, the upper layer was distilled water and the lower layer was a chlorinated paraffin (Paroil-152, Dover Chemical Corp., USA). Polystyrene (PS) beads (Polysciences Inc., USA) with a diameter range 106-125 μm and 200-300 μm served as islet surrogates. PS beads were dispersed in distilled water in a concertation range of 1000-10000 particles/ml.

5.4 Results and Discussion

The first set of experiments aims to identify critical conditions that form steady-state cusps. Initially, a layer of distilled water overlaid a layer of a paraffin oil into the apparatus chamber. Only P3 and P4 were operated for the first set. An outflow Q_3 was generated through the withdrawal tube the inlet orifice of which was at a fixed height below the interface of the two horizontally stratified layers. Simultaneously, an inflow Q_4 of the same magnitude was generated by P4. Experiments were performed for three initial positions of the interface, i.e., the initial distance of the unperturbed interface from the withdrawal tube inlet, S. The initial

and final distances were measured using DinoCapture 2.0. software (AnMo Electronics Corp., Taiwan). Each experiment was repeated three times and the standard deviation was calculated. We waited long enough in between two successive tests for the interface to return to its initial position.

Figure 5.3 (i) illustrates the maximum depth of the interface, h_{max}, as a function of withdrawal flow rate, Q_3, for different values of S. For any value of S, the h_{max}-versus-Q_3 curve displays exponential-type behavior. When the withdrawal flow was below a critical value, Qc, the interface was disturbed weakly and formed a steady-state smooth dent. This state is termed as hump by Cohen [41] and is shown in Figure 5.3 (ii). As the flow reached a critical value, the hump evolved dramatically and reached a cusp shape. In Figure 5.3 (iii) a steady-state cusp shape is presented.

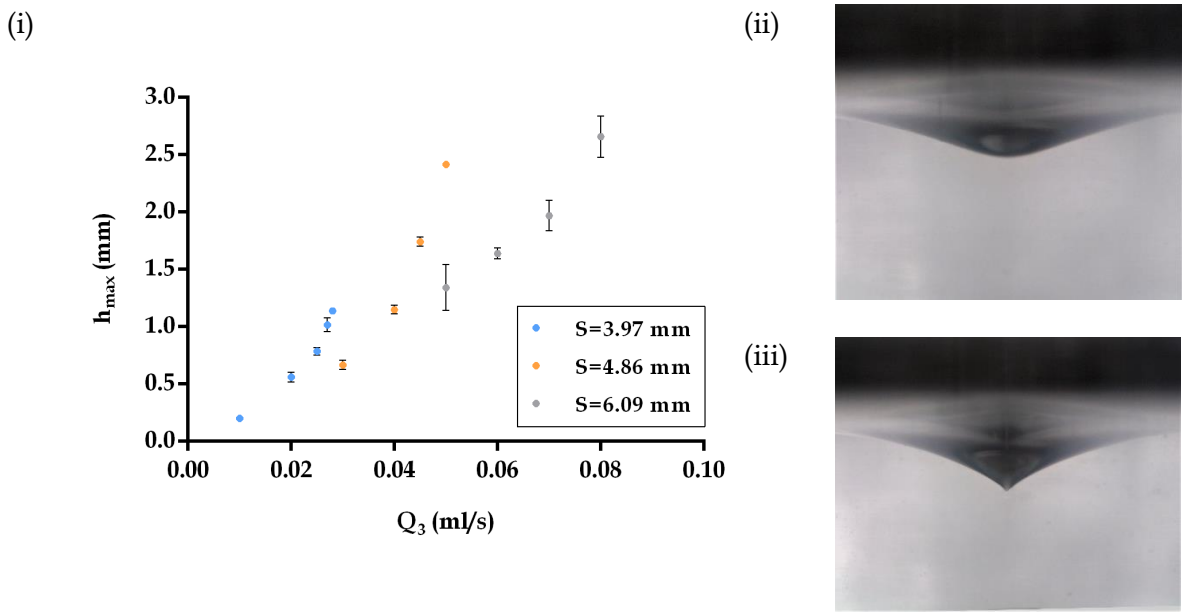

Figure 5.3 (i) The maximum depth of the interface, h_{max}, as a function of withdrawal flow rate, Q_3, for different values of S. For S= 4.86 ± 0.10 mm, the interface disturbance as a steady-state (ii) hump for Q_3= 0.045 ml/s and (iii) cusp for Q_3= 0.050 ml/s. Error bars represent the standard deviation.

The aim of the second set of experiments is to investigate the breakthrough of a particle through a dynamic steady-state interface. For this set, the hydraulic system was employed in its entirety. P1 and P2 were used to drive the sample flow, Q_1, and sheath flow, Q_2, into the apparatus. The flow rate Q_1 was set equal to 0.05 ml/s, while the flow ratio k was set equal to

10. P3 and P4 were operated as before. The withdrawal rate was equal to 0.02 ml/s. The initial distance of the unperturbed interface from the tube inlet was S= 3.52 ± 0.10 mm. A limited number of experiments were performed. Thus, a qualitative analysis of our most important observations is presented.

Figure 5.4 shows snapshots of a particle passing through a steady-state cusp. Initially, the particle moved on the symmetry axis and in the direction to the inlet of the withdrawal tube, until it reached the tip of the cusp, i.e., the point of the interface at maximum depth. Interface stretching occurred because of the movement of the particle. Subsequently, a tail, i.e., a fluid volume connecting the particle and the upper fluid layer, was formed above the particle. We observed three typical stages of its evolution, necking, elongation and breaking [58]. At the first stage, the radius of the tail became smaller forming a neck-shape volume. Afterwards, the neck elongated, evolving in a cylinder of a continuously decreasing radius. During the third stage, the tail was broken at a point close to the particle, leaving the smaller portion of fluid attached on the particle surface. Lastly, the particle was entrained along with the fluid volume.

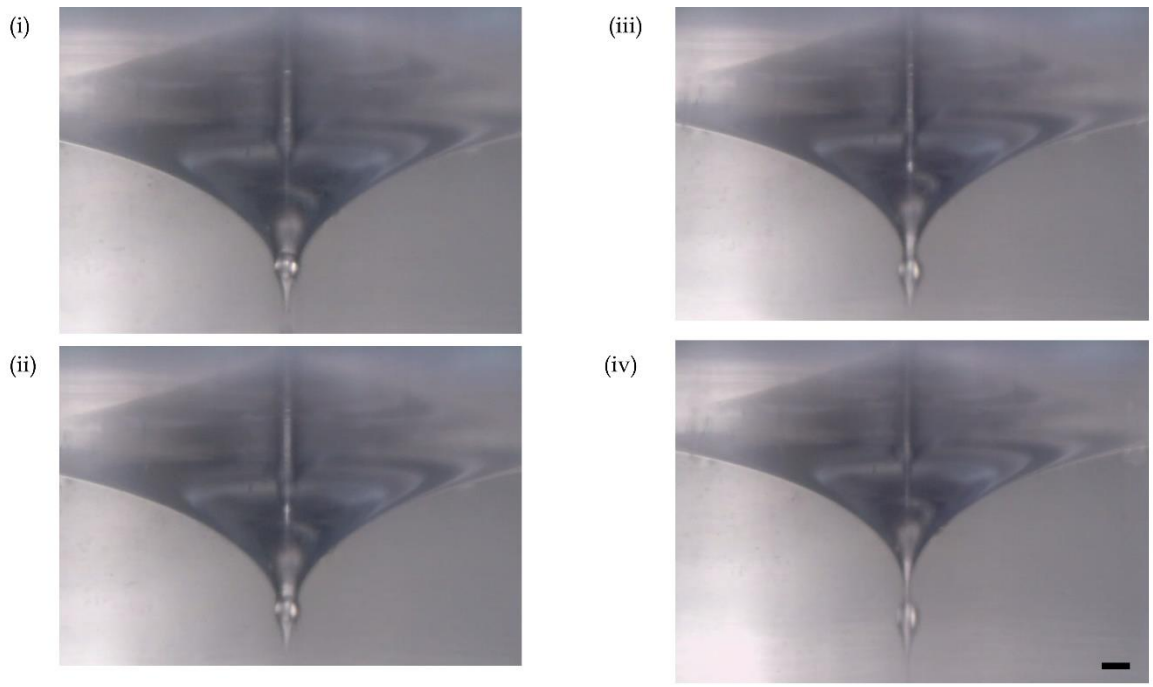

Figure 5.4 Snapshots of a particle passing through a steady-state cusp and being entrained with a fluid volume along for S= 3.5 ± 0.1 mm and Q_3=0.02 ml/s. (i) The interface stretching and the evolution of the tail: (ii) Necking (iii) Elongation (iv) Breaking. Scale bar, 200 μm.

Figure 5.5 (i) shows snapshots of a small particle passing through a steady-state cusp. The three stages of the evolution of the tail occurred as described above. Nevertheless, we observe that the fluid volume entrained along with the particle is significantly smaller than in the previous case. In both cases, as the particle moved through the interface, a volume of the upper fluid below, V_b, and above, V_a, was entrained along with the particle. In particular, the particle surface touched the interface forming a three-phase contact line (TPCL). Below the TPCL, a volume of the upper fluid, V_b, was trapped. By assuming the tip of the cusp as truncated conical volume, V_b can be estimated as a volume of a cone minus the volume of a spherical cap. By neglecting the film thickness at the flank, a second TPCL on the upper side of the particle occurred. The mean radius of the volume V_a was O(a), while the height depends on the breakthrough mode. The tail was broken after it has been stretched over a distance equal to multiple times the radius of the particle. Breaking happened closer to the particle and a second truncated conical volume attached above the particle. We conclude that the entrained fluid volume is determined mainly from the particle size for a given cusp. Further research is essential to quantify the effect of the particle size on the entrained fluid volume. Figure 5.5 (ii) illustrates an occasion where the breakthrough of a small particle was prevented. The particle moved in the direction to the inlet of the withdrawal tube; however, it was not close enough to the symmetry axis of the tube. As a result, the particle didn't reach directly the tip of the cusp, and eventually, it was trapped.

Figure 5.6 shows two particles approaching the steady-state cusp. Both particles moved on the symmetry axis and in the direction to the inlet of the withdrawal tube. There was a noticeable distance between the leading and the following particle. Both particles were encapsulated; the volume V_b was not the same for both particles, though. In particular, the following particle stretched the interface during the breaking stage of the leading particle. As a result, the fluid volume associated with tail elongation of the leading particle was trapped under the following particle. It is apparent that the separation distance of the particles can lead to a bigger or lesser fluid volume attached above each particle. These observations highlight the importance of proper feeding of the particles, i.e., focused and separated particles.

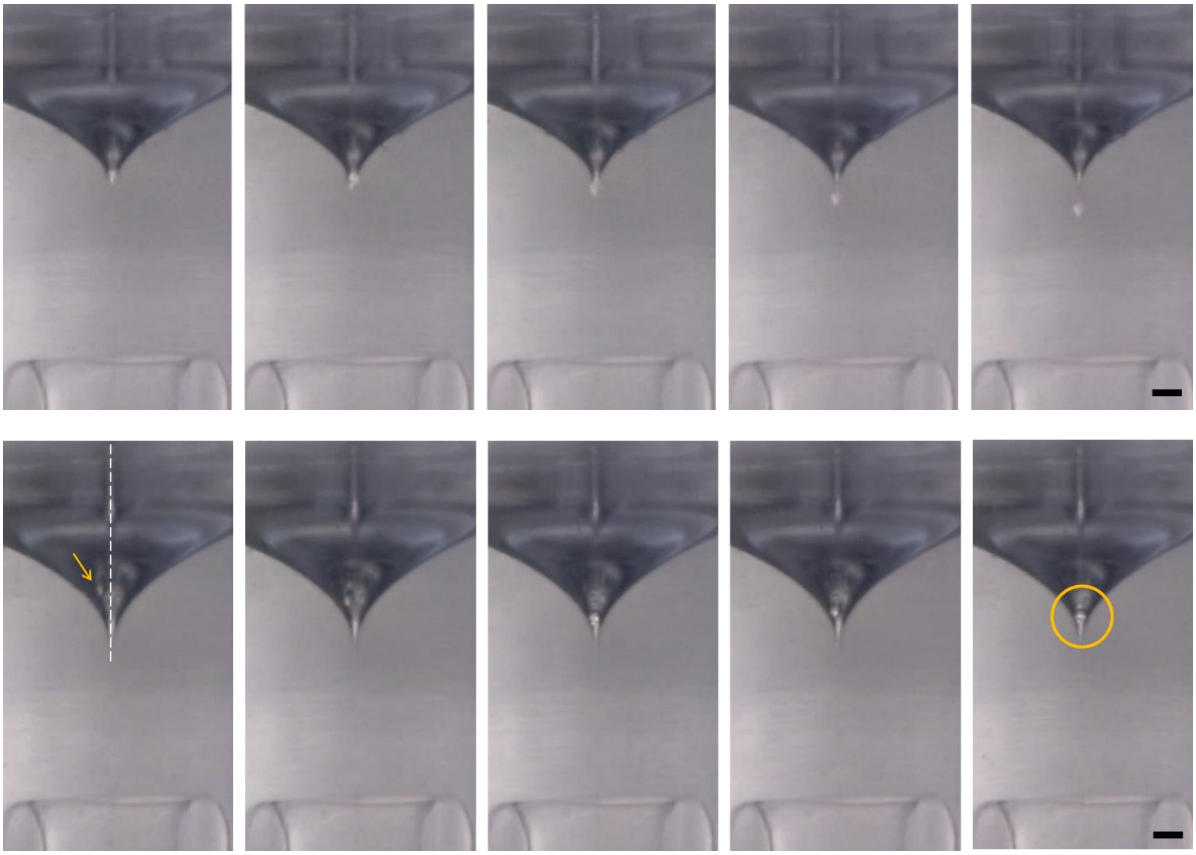

Figure 5.5 Snapshots of a small particle moving in the direction to the inlet of the withdrawal tube. (i) Aligned, passing through interface; (ii) not aligned, not passing though the interface. Scale bar, 200 µm.

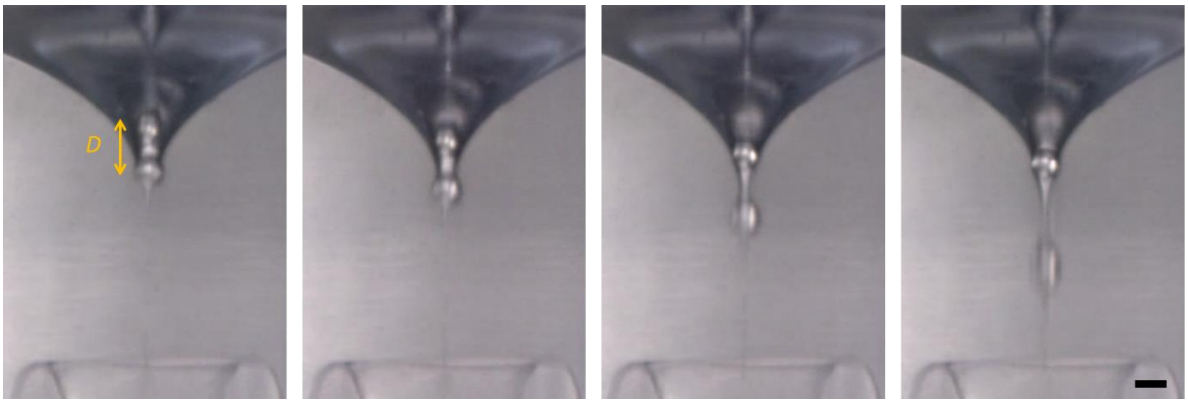

Figure 5.6 Snapshots of two particles approaching the steady-state cusp. The first and the last snapshot shows that the volume V_b is not the same for both particles. Scale bar, 200 µm.

5.5 Summary and Conclusions

By utilizing 3DP technology, the development of a microencapsulation apparatus including a hydraulic pumping system was carried out. The apparatus was designed as a contrast of interlocking parts. We followed a modular design strategy as it enables better surface treatment. PolyJet technology was employed to fabricate the apparatus. The hydraulic pumping system consisting of four syringe pumps was fabricated with an FDM printer. We modified appropriately an open-source code to drive the pumps. We experimentally investigated the encapsulation of spherical particles serving as islet surrogates by employing the hydrodynamics of selective withdrawal.

The results of our study are presented below:

- Experiments were performed for various distances of the tip of the withdrawal tube from the unperturbed interface, S, to identify critical conditions that lead to steady state cusps. As the withdrawal flow reached a critical value, Qc, the disturbed interface formed a cusp. In addition, the maximum depth of the interface, h_{max}, was measured as a function of withdrawal flow rate, Q_3. The results revealed an exponential-type behavior of h_{max}-versus-Q_3 curve.
- Evolution of the tail during the break of a particle through a dynamic steady-state cusp was observed. Three typical stages of the evolution of the tail, necking, elongation and breaking were observed. The tail was broken after it had been stretched over a distance equal to multiple times the radius of the particle. Breaking happened closer to the particle.
- As the particle moved through the interface, a volume of the upper fluid below, V_b, and above, V_a, was entrained along with the particle. For a given cusp, the entrained fluid volume is determined mainly by the particle size. By controlling this fluid volume, we can control the capsule volume, hence, the thickness of the coating membrane.
- A moving particle that was not close enough to the symmetry axis of the tube, did not reach directly the tip of the cusp, and eventually, it was trapped. Furthermore, the separation distance of the particles can lead to a bigger or lesser fluid volume, V_a, attached above each particle. Our observations highlight the importance of proper feeding of the particles, i.e., focused and separated particles.

References

[1] H. H. Hu, N. A. Patankar, and M. Y. Zhu, "Direct Numerical Simulations of Fluid – Solid Systems Using the Arbitrary Lagrangian – Eulerian Technique," *J. Comput. Phys.*, vol. 169, no. 2, pp. 427–462, 2001.

[2] H. H. Hu, D. D. Joseph, and M. J. Crochet, "Direct Simulation of Fluid Particle Motions," *Theor. Comput. Fluid Dyn.*, vol. 3, no. 5, pp. 285–306, 1992.

[3] H. H. Hu, "Direct simulation of flows of solid-liquid mixtures," *Int. J. Multiph. Flow*, vol. 22, no. 2, pp. 335–352, 1996.

[4] A. A. Johnson and T. E. Tezduyar, "Advanced mesh generation and update methods for 3D flow simulations," *Comput. Mech.*, vol. 23, pp. 130–143, 1999.

[5] J. Feng, H. H. Hu, and D. D. Joseph, "Direct Simulation of Initial Value Problems for the Motion of Solid Bodies in a Newtonian Fluid Part 1. Sedimentation," *J. Fluid Mech.*, vol. 261, pp. 95–134, 1994.

[6] J. Feng, H. H. Hu, and D. D. Joseph, "Direct Simulation of Initial Value Problems for the Motion of Solid Bodies in a Newtonian Fluid. Part 2. Couette adn Poiseuille Flows.," *J. Fluid Mech.*, vol. 277, pp. 271–301, 1994.

[7] P. Y. Huang, J. J. Feng, H. H. Hu, and D. D. Joseph, "Direct Simulation of the Motion of Solid Particles in Couette and," *J. Fluid Mech.*, vol. 343, pp. 73–94, 1997.

[8] G. D'Avino, T. Tuccillo, P. L. Maffettone, F. Greco, and M. A. Hulsen, "Computers & Fluids Numerical simulations of particle migration in a viscoelastic fluid subjected to shear flow," *Comput. Fluids*, vol. 39, no. 4, pp. 709–721, 2010.

[9] R. Glowinski, T. Pan, T. I. Hesla, and D. D. Joseph, "A distributed Lagrange multiplier/ frictious domain method for particulate flows," *Int. J. Multiph. Flow*, vol. 25, no. 5, pp. 755–794, 1999.

[10] R. Glowinski, T. W. Pan, T. I. Hesla, and D. D. Joseph, "A Fictitious Domain Approach to the Direct Numerical Simulation of Incompressible Viscous Flow past Moving Rigid Bodies: Application to Particulate Flow," *J. Comput. Phys.*, vol. 426, pp. 363–426, 2001.

[11] P. Singh, D. D. Joseph, T. I. Hesla, R. Glowinski, and T. Pan, "A distributed Lagrange multiplier/fictitious domain method for viscoelastic particulate flows," *J. Nonnewton. Fluid Mech.*, vol. 91, no. (2-3), pp. 165–188, 2000.

[12] J. Hao, T. Pan, R. Glowinski, and D. D. Joseph, "A fictitious domain/distributed Lagrange multiplier method for the particulate flow of Oldroyd-B fluids: A positive definiteness preserving approach," *J. Nonnewton. Fluid Mech.*, vol. 156, no. 1–2, pp. 95–111, 2009.

[13] M. Rahmani and A. Wachs, "Free falling and rising of spherical and angular particles," *Phys. fluids*, vol. 26, no. 8, p. 083301, 2014.

[14] S. Chen and G. D. Doolen, "Lattice Boltzmann method for fluid flows," *Annu. Rev. Fluid Mech.*, vol. 30, no. 1, pp. 329–364, 1998.

[15] A. Ladd, "Numerical simulations of particulate suspensions via a discretized Boltzmann equation. Part 1. Theoretical foundation," *J. Fluid Mech.*, vol. 271, pp. 285–309, 1994.

[16] D. Yu, R. Mei, and W. Shyy, "A multi-block lattice Boltzmann method for viscous uid ows," *Int. J. Numer. methods fluids*, vol. 39, no. 2, pp. 99–120, 2002.

[17] K. Han, Y. T. Feng, and D. R. J. Owen, "Coupled lattice Boltzmann and discrete element modelling of fluid – particle interaction problems," *Comput. Struct.*, vol. 85, no. 11–14, pp. 1080–1088, 2007.

[18] C. S. Peskin, "The immersed boundary method," *Acta Numer.*, vol. 11, pp. 479–517, 2002.

[19] Z. Feng and E. E. Michaelides, "The immersed boundary-lattice Boltzmann method for solving fluid – particles interaction problems," *J. Comput. Phys.*, vol. 195, no. 2, pp. 602–628, 2004.

[20] Z. Xia, K. Connington, S. Rapaka, and P. Yue, "Flow patterns in the sedimentation of an elliptical particle," *J. Fluid Mech.*, vol. 625, pp. 249–272, 2009.

[21] A. J. C. Ladd and R. Verberg, "Lattice-Boltzmann Simulations of Particle-Fluid Suspensions," *J. Stat. Phys.*, vol. 104, no. 5–6, pp. 1191–1251, 2001.

[22] H. Başağaoğlu, S. Succ, D. Wyrick, and J. Blount, "Particle Shape Influences Settling and Sorting Behavior in Microfluidic Domains," *Sci. Rep.*, vol. 8, no. 1, p. 8583, 2018.

[23] N. Q. Nguyen and A. J. C. Ladd, "Lubrication corrections for lattice-Boltzmann simulations of particle suspensions," *Phys. Rev. E*, vol. 66, no. 4, p. 046708, 2002.

[24] C. K. Aidun and J. R. Clausen, "Lattice-Boltzmann Method for Complex Flows," *Annu. Rev. Fluid Mech.*, vol. 52, pp. 439–472, 2010.

[25] I. Psychogios and D. Hatziavramidis, "Two-nozzle hydrodynamic focusing," *Chem. Eng. Sci.*, vol. 123, pp. 429–435, 2015.

[26] G. Lee, C. Chang, and S. Huang, "The hydrodynamic focusing effect inside rectangular microchannels," *J. Micromechanics Microengineering*, vol. 16, no. 5, p. 1024, 2006.

[27] G. Lee, C. Hung, B. Ke, G. Huang, and B. Hwei, "Hydrodynamic Focusing for a Micromachined Flow Cytometer," *J. Fluids Eng.*, vol. 123, no. 3, pp. 672–679, 2001.

[28] F. Wang *et al.*, "Microfluidic Delivery of Small Molecules Into Mammalian Cells Based on Hydrodynamic Focusing," *Biotechnol. Bioeng.*, vol. 100, no. 1, pp. 150–158, 2008.

[29] R. Karnik *et al.*, "Microfluidic Platform for Controlled Synthesis of Polymeric Nanoparticles," *Nano Lett.*, vol. 8, no. 9, pp. 2906–2912, 2008.

[30] C.-H. Yeh, P.-W. Lin, and Y.-C. Lin, "Chitosan microfiber fabrication using a microfluidic chip and its application to cell cultures," *Microfluid. Nanofluidics*, vol. 8, no. 1, pp. 115–121, 2010.

[31] M. Frankowski, J. Theisen, A. Kummrow, P. Simon, N. Bock, and M. Schmidt, "Microflow Cytometers with Integrated Hydrodynamic Focusing," *Sensors*, vol. 13, pp. 4674–4693, 2013.

[32] P. K. Shivhare, A. B. P. Sajeesh, and A. P. A. K. Sen, "Hydrodynamic focusing and interdistance control of particle-laden flow for microflow cytometry," *Microfluid. Nanofluidics*, vol. 20, no. 6, p. 86, 2016.

[33] A. Yang and W. Hsieh, "Hydrodynamic focusing investigation in a micro-flow cytometer," *Biomed. Microdevices*, vol. 9, no. 2, pp. 113–122, 2007.

[34] T. Kin, "Islet Isolation for Clinical Transplantation," in *The Islets ofLangerhans, Advances in Experimental Medicine and Biology*, 2nd ed., M. Islam, Ed. Dordrecht: Springer, 2010, pp. 683–710.

[35] P. In't Veld and S. Smeets, "Microscopic Anatomy of the Human Islet of Langerhans," in *Islets of Langerhans*, 2nd ed., M. Islam, Ed. Dordrecht: Springer, 2014, pp. 1–18.

[36] G. D. Fontane, W. J. Labadie, and B. Loftis, "Optimal Control of Reservoir Discharge Quality Through Selective Withdrawal," *Water Resour. Res.*, vol. 17, no. 6, pp. 1594–1602, 1981.

[37] J. R. Lister, "Selective withdrawal from a viscous two-layer system," *J. Fluid Mech.*, vol. 198, pp. 231–254, 1989.

[38] I. Cohen, H. Li, J. L. Hougland, M. Mrksich, and S. R. Nagel, "Using selective withdrawal to coat microparticles.," *Science (80-.).*, vol. 292, no. 5515, pp. 265–267, 2001.

[39] J. Psihogios, V. Benekis, and D. Hatziavramidis, "Selective withdrawal and draining of a viscous liquid under air from a cylindrical tank through a tube imbedded in the liquid," *Chem. Eng. Sci.*, vol. 138, pp. 516–523, 2015.

[40] I. Cohen and S. R. Nagel, "Scaling at the Selective Withdrawal Transition through a Tube Suspended above the Fluid Surface," *Phys. Rev. Lett.*, vol. 88, no. 7, p. 074501, 2002.

[41] I. Cohen, "Scaling and transition structure dependence on the fluid viscosity ratio in the selective withdrawal transition," *Phys. Rev. E*, vol. 70, no. 2, p. 026302, 2004.

[42] S. C. Case and S. R. Nagel, "Spout States in the Selective Withdrawal of Immiscible Fluids through a Nozzle Suspended above a Two-Fluid Interface," *Phys. Rev. Lett.*, vol. 98, no. 11, p. 114501, 2007.

[43] D. Hatziavramidis and C. Pozrikidis, "Hydrodynamic analysis of pancreatic islet micro-encapsulation by selective withdrawal," *Eng. Anal. Bound. Elem.*, vol. 32, no. 1, pp. 11–20, 2008.

[44] F. Duarte, R. Gormaz, and S. Natesan, "Arbitrary Lagrangian – Eulerian method for Navier – Stokes equations with moving boundaries l Gormaz," *Comput. Methods Appl. Mech. Eng.*, vol. 193, pp. 4819–4836, 2004.

[45] H. Braess and P. Wriggers, "Arbitrary Lagrangian Eulerian finite element analysis of free surface flow," *Comput. Methods Appl. Mech. Eng.*, vol. 190, no. 1–2, pp. 95–109, 2000.

[46] W. Dettmer and D. Peric, "A computational framework for free surface fluid flows accounting for surface tension," *Comput. Methods Appl. Mech. Eng.*, vol. 195, pp. 3038–3071, 2006.

[47] P. Yue, J. J. Feng, C. A. Bertelo, and H. H. Hu, "An arbitrary Lagrangian – Eulerian method for simulating bubble growth in polymer foaming," *J. Comput. Phys.*, vol. 226, pp. 2229–2249, 2007.

[48] D. Zhou and J. J. Feng, "Journal of Non-Newtonian Fluid Mechanics Selective withdrawal of polymer solutions: Computations," *J. Nonnewton. Fluid Mech.*, vol. 165, no. 15–16, pp. 839–851, 2010.

[49] K. Yang, F. Hong, and P. Cheng, "A fully coupled numerical simulation of sessile droplet evaporation using Arbitrary Lagrangian – Eulerian formulation," *HInternational J. Heat Mass Transf.*, vol. 70, pp. 409–420, 2014.

[50] S. Ganesan and L. Tobiska, "Arbitrary Lagrangian – Eulerian finite-element method for computation of two-phase flows with soluble surfactants," *J. Comput. Phys.*, vol. 231, no. 9, pp. 3685–3702, 2012.

[51] D. Ni, F. J. Hong, P. Cheng, and G. Chen, "Numerical study of liquid-gas and liquid-liquid Taylor flows using a two- phase flow model based on Arbitrary-Lagrangian – Eulerian (ALE) formulation," *Int. Commun. Heat Mass Transf.*, vol. 88, pp. 37–47, 2017.

[52] S. C. Pont and J. Eggers, "Sink Flow Deforms the Interface Between a Viscous Liquid and Air into a Tip Singularity," *Phys. Rev. Lett.*, vol. 96, no. 3, p. 034501, 2006.

[53] D. T. Hatziavramidis, "Apparatus and Method for Encapsulating Pancratic Cells," US Patent 8,093,038 B2, 2012.

[54] E. K. Sackmann, A. L. Fulton, and D. J. Beebe, "The present and future role of microfluidics in biomedical research," *Nature*, vol. 507, no. 7491, pp. 181–189, 2014.

[55] T. A. Duncombe, A. M. Tentori, and A. E. Herr, "Microfluidics: reframing biological enquiry," *Nat. Rev. Mol. Cell Biol.*, vol. 16, no. 9, pp. 554–567, 2015.

[56] S. K. Sia and G. M. Whitesides, "Microfluidic devices fabricated in poly(dimethylsiloxane) for biological studies," *Electrophoresis*, vol. 24, no. 21, pp. 3563–3576, 2003.

[57] R. Amin, S. Knowlton, A. Hart, B. Yenilmez, and F. Ghaderinezhad, "3D-printed microfluidic devices," *Biofabrication*, vol. 8, no. 2, p. 022001, 2016.

[58] H. Chen, Q. Xu, S. Liang, and J. Li, "Film coating on a small sphere crossing an oil-water interface," *Phys. Rev. Fluids*, vol. 3, no. 12, p. 124003, 2018.

[59] L. M. Ricles, J. C. Coburn, M. Di Prima, and S. S. Oh, "Regulating 3D-printed medical products," *Sci. Transl. Med.*, vol. 10, no. 461, p. eaan6521, 2018.

[60] S. A. M. Tofail, E. P. Koumoulos, A. Bandyopadhyay, S. Bose, L. O. Donoghue, and C. Charitidis, "Additive manufacturing: scientific and technological challenges, market uptake and opportunities," *Mater. Today*, vol. 21, no. 1, pp. 22–37, 2018.

[61] S. Waheed, J. M. Cabot, N. P. Macdonald, T. Lewis, R. M. Guijt, and M. C. Breadmore, "3D printed microfluidic devices: enablers and barriers," *Lab Chip*, vol. 16, no. 11, pp. 1993–2013, 2016.

[62] J. R. C. Dizon, E. H. J. Alejandro, Q. Chen, and R. C. Advincula, "Mechanical characterization of 3D-printed polymers," *Addit. Manuf.*, vol. 20, pp. 44–67, 2018.

[63] N. P. Macdonald, J. M. Cabot, P. Smejkal, R. M. Guijt, B. Paull, and M. C. Breadmore, "Comparing Microfluidic Performance of Three-Dimensional (3D) Printing Platforms," *Anal. Chem.*, vol. 89, no. 7, pp. 3858–3866, 2017.

[64] Q. Ji *et al.*, "A Modular Microfluidic Device via Multimaterial 3D Printing for Emulsion Generation," *Sci. Rep.*, vol. 8, no. 1, p. 4791, 2018.

[65] O. A. Mohamed, S. H. Masood, and J. L. Bhowmik, "Optimization of fused deposition modeling process parameters: a review of current research and future prospects," *Adv. Manuf.*, vol. 3, no. 1, pp. 42–53, 2015.

[66] A. J. L. Morgan *et al.*, "Simple and Versatile 3D Printed Microfluidics Using Fused Filament Fabrication," *PLoS One*, vol. 11, no. 4, p. e0152023, 2016.

[67] K. Alessandri *et al.*, "A 3D printed microfluidic device for production of functionalized hydrogel microcapsules for culture and differentiation of human Neuronal Stem Cells (hNSC)," *Lab Chip*, vol. 16, no. 9, pp. 1593–1604, 2016.

[68] B. C. Tan, J. H. A. Vlaskamp, and P. Denissenko, "Cavity formation in the wake of falling spheres submerging into a stratified two-layer system of immiscible liquids," *J. Fluid Mech.*, vol. 790, pp. 33–56, 2016.

[69] J. Pierson and J. Magnaudet, "Inertial settling of a sphere through an interface. Part 1. From sphere flotation to wake fragmentation," *J. Fluid Mech.*, vol. 835, pp. 762–807, 2018.

[70] P. A. Jarvis, H. M. Mader, H. E. Huppert, K. V. Cashman, and J. D. Blundy, "Experiments on the low-Reynolds-number settling of a sphere through a fluid interface," *Phys. Rev. Fluids*, vol. 4, no. 2, p. 024003, 2019.

[71] B. Wijnen, E. J. Hunt, G. C. Anzalone, and J. M. Pearce, "Open-Source Syringe Pump Library," *PLoS One*, vol. 9, no. 9, p. e107216, 2014.

[72] J. R. Lake, K. C. Heyde, and W. C. Ruder, "Low-cost feedback-controlled syringe pressure pumps for microfluidics applications," *PLoS One*, vol. 12, no. 4, p. e0175089, 2017.

PART III

Conclusions

Chapter

6 Conclusions and future perspectives

Synopsis

In this Chapter, we summarize the research presented in this Dissertation and discuss briefly our conclusions. Our endeavors brought us closer to understanding and fulfilling the requirements of an efficient apparatus for islet microencapsulation. Future research regarding the physical mechanisms occurring in the apparatus and the development of a high yield apparatus is proposed.

6.1 Summary of this Dissertation

Islet transplantation with immunosuppression, known as Edmonton protocol, has been proposed as a therapeutic modality for T1DM treatment [1]. Direct pancreatic islet transplantation cannot serve as a widespread therapeutic modality due to the need for lifelong immunosuppression. Therefore, several encapsulation techniques have been developed in order to enclose the islets in semipermeable vehicles that will allow oxygen and nutrients input as well as insulin, other metabolites and waste output, while also accomplishing immunoisolation at the same time [2]. In Chapter 1, we summarized the last five years' accomplishments in islet encapsulation technology for treatment of T1DM. Despite important advances, encapsulation technology continues to face significant obstacles for full clinical implementation. Conventional microencapsulation technologies fail to prevail, as they produce single-sized microcapsules and attain low efficiencies [3]. Given the fact of polydispersity in islets, a different manipulation is required in every occasion, in order to fabricate microcapsules of proper size efficiently. Efficiency here is defined as the ratio of the number of properly encapsulated islets to the total number of islets fed. By proper encapsulation it is meant one in which the encapsulated islets are viable and functional. In order to accomplish this goal, a uniform coating of thickness from 10 to 50 μm is required [3].

With the intent to contribute to eliminating some of the challenges, we propose an islet microencapsulation apparatus designed by the principles of Mechanics and Cytotechnology. The fundamental idea of our approach is that encapsulation is driven by islet motion and capsule size and shape are determined by the individual islet size and shape, respectively. In Chapter 2, we explained the conceptual design of the apparatus by introducing the functional parts of the apparatus. It consists of a feeder, an encapsulation chamber, a photopolymerization section and a sorting system. A hydrodynamic focusing configuration is utilized to ensure feeding the individual islets in the direction toward the inlet of a withdrawal tube. The encapsulation chamber is a vessel containing two horizontally stratified layers of two immiscible fluids. The islets enter the chamber in a file through a vertical tube with its outlet orifice above the interface of the two fluids. The islets enclosed in polymeric solution drops leave the channel through a withdrawal tube, a tube of cross section equal to the tube feeding the islets and at the same distance on the other side of the interface. The withdrawal tube begins with a straight vertical part and ends with a coiled part providing

enough time for polymer crosslinking and formation of a hydrogel membrane. Lastly, the encapsulated islets are sorted and recovered using a gravity-driven microfluidic sorting system. In this Dissertation, we focused specifically on two parts of the apparatus, the feeding system and the encapsulation chamber. The utilization of hydrodynamic focusing and selective withdrawal is proposed as a feeding system and a microencapsulation method, respectively.

In Chapter 3, we developed a computational model to simulate the motion of particles in a hydrodynamic focusing configuration. In all the earlier numerical studies of hydrodynamic focusing of microparticles, the equations of motion of the solid phase were not included into the formulation. In our case, the volumetric fraction of islets was significant, and thus, the sample fluid could not be assumed homogenous. To our knowledge, this is the first time that a numerical model can predict the motion of particles in a hydrodynamic focusing system. The equations of fluid flow and particle motion were solved by implementing the Finite Element (FE) formalism and utilizing the arbitrary Lagrangian-Eulerian (ALE) moving mesh technique. Having validated our methodology, we performed simulations with spherical and elliptical particles, individually released at the entrance of the main channel of a hydrodynamic focusing domain. Finally, we simulated the focusing and separation of two particles as well as a group of particles.

In Chapter 4, the flow generated by selective withdrawal in an apparatus for micro-encapsulation of pancreatic islets was studied through computational fluid dynamic simulations. Previous studies have simplified the problem by considering a tank of infinite size in the horizontal direction and approximating the tubes as a doublet of a point mass source and a sink of equal strength. The model presented here employed a detailed flow geometry of a finite-size tank with a withdrawal and a feeding tube of equal dimensions. The governing equations were solved numerically using a traditional FE method to resolve the flow and an ALE method to track the movement and deformation of the fluid-fluid interface. The effect of design and function parameters on the phenomenon of selective withdrawal was studied. Parameters included flow rates, geometric dimensions and physical characteristics of the fluids.

In Chapter 5, we reported the development of an apparatus including a hydraulic pumping system by employing three-dimensional printing (3DP) technology. Despite the rapid expansion of 3DP, there is a limited number of reports in the literature [4][5] demonstrating the potential contribution to encapsulation technology. The apparatus was

designed as a contrast of interlocking parts. We followed a modular design strategy as it enables better surface treatment. PolyJet technology was employed to fabricate the apparatus. The hydraulic pumping system consisting of four syringe pumps was fabricated with a Fused Deposition Modeling printer. An open-source code was modified to drive the pumps. In our apparatus, spherical particles serving as islet models were encapsulated by employing the hydrodynamics of selective withdrawal. Particles passing through a fluid-fluid interface have been recently studied as they are encountered in many engineering applications [6]. We investigated the condition for a particle to move through a dynamic steady-state interface.

6.2 Concluding remarks

This Dissertation brought us closer to understanding and fulfilling the requirements of an efficient apparatus for islet microencapsulation. We focused on two requirements; the accurate separation of loaded islets to encapsulate one islet per capsule and the uniform thickness of the capsule membrane to accommodate the heterogeneous morphology of islets. The first requirement was met by the utilization of hydrodynamic focusing as a feeding system in our device. The second requirement was met by the employment of selective withdrawal [7] as an encapsulation method. To that end, we developed two computation models regarding the hydrodynamic focusing of particles and the flow generated by selective withdrawal in the encapsulation chamber. The findings of the two computational studies shed light on the physical mechanisms occurring in the apparatus.

Our hydrodynamic focusing system aimed at feeding the pancreatic islets in a single file, thus, ensuring separate encapsulation of individual islets. The islets were simulated as spherical and elliptical particles initially released at random positions. In all cases, the effect of sheath-to-sample flow ratio on separation and focusing was investigated. At flow ratio equal to ten, individual particles were focused irrespective of their initial position and shape. The objective of separate encapsulation of individual islets can be jeopardized due to aggregation of islets. Our results indicate that two particles at a small initial distance between them can be separated by adjusting the flow ratio.

By knowing the effect of design parameters on selective withdrawal, we can appropriately shape the fluid-fluid interface. In order to eliminate the effect of chamber walls, the ratio of the chamber radius to the radius of the tube must be at least equal to 40. A hidden geometric parameter, the ratio of withdrawal tube wall thickness to tube radius, was found to have a significant effect on the simulation results. In addition, we investigated the flow and physical conditions affecting the evolution of a cusp. When transition from hump to cusp occurred, the maximum distance from the unperturbed interface reached a critical value and the curvature diverged. The cusp occurred only for a range of viscosity and density ratios and the transition from a hump to a cusp was dominated by gravitational and viscous forces. Our model can be used in the assessment of fluid candidates for encapsulation materials.

By operating the 3D-printed microencapsulation apparatus, we experimentally investigated the encapsulation of spherical beads serving as islet surrogates. The evolution of the tail during the breakthrough of a particle through a dynamic steady-state cusp was studied. Three typical stages of the evolution of the tail, necking, elongation and breaking were observed [6]. The tail was broken after it had been stretched over a distance equal to multiple times the radius of the particle. Breaking happened closer to the particle. For a given cusp, the entrained fluid volume was determined mainly by the particle size. A moving particle that was not close enough to the symmetry axis of the tube, did not reach directly the tip of the cusp, and eventually, it was trapped. Furthermore, the separation distance of the particles can lead to a bigger or smaller fluid volume attached above each particle. Our observations highlighted the importance of proper feeding of particles, i.e., focused and separated particles.

6.3 Directions for future research

Hydrodynamic focusing systems are encountered in different features and geometries. For, instance, the configuration can be either a cross-junction geometry with side channels perpendicular to a central channel or a two-nozzle system with one nozzle inside the other. By applying our model, we can optimize the geometry of any configuration and fulfill the requirement for proper feeding. As we demonstrated the capabilities of our model to simulate a group of particles, further research is essential to study grouping behavior [8]. In addition, the motion of particles in microfluidic platforms has gained increasing interest as it is

encountered in many applications [9][10][11]. For instance, engineered drug cargos are encountered in various shapes influencing their performance and motion in microflows [12][13]. The present model can be readily applied to various microfluidic configurations to study the dependence of the motion of entities, both biological and synthetic. In our case, the model can be employed to simulate the sorting of the encapsulated islets in a gravity-driven microfluidic sorting system [14].

In this Dissertation, we developed a computational model to simulate a fluid-fluid interface pertinent to efficient islet encapsulation. The next step should be the incorporation of the dynamics of a moving particle in our approach. New computational models have been recently developed to study the dynamics of a particle interacting with a static steady-state fluid-fluid interface [15], [16]. In our case, the main challenge is that the particle moves through a dynamic steady-state interface. The development of a computational model can assist us to gain an understanding of a complicated hydrodynamic phenomenon. Additionally, it can be applied to predict the effect of a particle size on the entrained fluid volume.

Experimental research is essential to study the effect of the particle size on the entrained fluid volume. By controlling this fluid volume, we can control the capsule volume, hence, the thickness of the coating membrane. Up to now, our experiments showed promising results. Our ongoing study aims to associate the cusp shape, i.e., height and curvature, and the particle size with the entrained fluid volume. Further research can clarify the effect of the physical characteristics of the fluids and the particle, as well as the dominant forces during a breakthrough. These experimental studies can lead us to operate the apparatus in order to finally encapsulate living cells, such as pancreatic islets.

From an engineering perspective, the apparatus is designed to deliver high yields and rates of encapsulation necessitated by the high number of islets required for TIDM therapy. This can be accomplished by optimizing the function of the apparatus, i.e., maximizing the encapsulation rate. Higher yields can be achieved by simultaneously operating multiple apparatuses. Beyond the research presented here, two issues need to be addressed, the controlled polymerization to produce a semipermeable membrane that ensures islet viability and function and the effective sorting and recovery of the encapsulated islets. In our apparatus, photopolymerization occurs inside the coiled part of the withdrawal tube by employing a 514 nm light of an argon-ion laser to excite Eosin-Y, an initiator of photopolymerization, on the surface of the islets. With the intent to control the degree of

polymerization and the porosity and permeability of the capsule, we must determine the optimum exposing time. Regarding the sorting of the encapsulated islets, the optimization of a gravity-driven microfluidic sorting system is proposed. Effective recovery requires a system that can perform continuous mass-dependent sorting. Flow rates and geometric dimensions need to be determined in order to design and develop such a system.

Due to numerous advantages of 3DP, two technologies were selected to fabricate our apparatus in a time efficient manner. As a next step, we must proceed by optimizing and standardizing the fabrication process in order to ensure repeatability, dimensional accuracy and biocompatibility. Medical-grade materials are now available, as 3DP technologies have already penetrated almost every field, and are used in many pharmaceutical and biological applications [17]. Lastly, we can explore the potential versatility of the apparatus by employing it for the treatment of other deceases [18] or for drug testing [19].

Ongoing research regarding islet encapsulation aims to remove obstacles such as limited source of cells, survival of transplanted cells, need for life-long immuno-suppression, capsule fibrosis and biocompatibility [20]. The choice of the material is of great importance in order to modulate the host response and avoid graft rejection. This material should meet certain criteria such as biocompatibility, immunoisolation and semipermeability for nutrients and secreted metabolites. Advances in immunomodulatory biomaterials and immunoisolation devices for islet transplantation were recently reviewed in [21]. Novel approaches have been proposed for the longevity and function of the graft by enhancing vascularization [22][23], modulating immune response [24][25] and addressing hypoxia. Fundamental aspects of islet physiology and emerging strategies to enhance oxygen delivery were thoroughly reviewed in [26]. Given the donor shortage, pseudo-islets [27] and stem-cell-derived islets [28] have the potential to be a replenishable source. With large-scale production of islets, the development and assessment of encapsulation strategies will be essentially accelerated. Nevertheless, further work is necessary to develop cells, that have all the necessary characteristics, in sufficient numbers and without a risk of teratogenicity. Future success requires close collaboration between partners from different fields, to deeply understand the current limitations and to employ current advances.

References

[1] A. M. J. Shapiro, M. Pokrywczynska, and C. Ricordi, "Clinical pancreatic islet transplantation," *Nat. Rev. Endocrinol.*, vol. 13, no. 5, p. 268, 2017.

[2] T. Desai and L. D. Shea, "Advances in islet encapsulation technologies," *Nat. Rev. Drug Discov.*, vol. 16, no. 5, p. 338, 2017.

[3] A. A. Tomei, V. Manzoli, C. A. Fraker, J. Giraldo, D. Velluto, and M. Najjar, "Device design and materials optimization of conformal coating for islets of Langerhans," *Proc. Natl. Acad. Sci.*, vol. 111, no. 29, pp. 10514–10519, 2014.

[4] A. J. L. Morgan *et al.*, "Simple and Versatile 3D Printed Microfluidics Using Fused Filament Fabrication," *PLoS One*, vol. 11, no. 4, p. e0152023, 2016.

[5] K. Alessandri *et al.*, "A 3D printed microfluidic device for production of functionalized hydrogel microcapsules for culture and differentiation of human Neuronal Stem Cells (hNSC)," *Lab Chip*, vol. 16, no. 9, pp. 1593–1604, 2016.

[6] J. Magnaudet and M. J. Mercier, "Particles, Drops, and Bubbles Moving Across Sharp Interfaces and Stratified Layers," *Annu. Rev. ofFluid Mech.*, vol. 52, pp. 61–91, 2020.

[7] I. Cohen and S. R. Nagel, "Scaling at the Selective Withdrawal Transition through a Tube Suspended above the Fluid Surface," *Phys. Rev. Lett.*, vol. 88, no. 7, p. 074501, 2002.

[8] D. Nie, J. Lin, and R. Chen, "Grouping behavior of coaxial settling particles in a narrow channel," *Phys. Rev. E*, vol. 93, no. 1, p. 013114, 2016.

[9] P. S. Ashis and K. Sen, "Particle separation and sorting in microfluidic devices: a review," *Microfluid. Nanofluidics*, vol. 17, no. 1, pp. 1–52, 2013.

[10] C. W. Shields IV, C. D. Reyes, and G. P. López, "Microfluidic Cell Sorting: A Review of the Advances in the Separation of Cells from Debulking to Rare Cell Isolation," *Lab Chip*, vol. 15, no. 5, pp. 1230–1249, 2015.

[11] A. Karimi, S. Yazdi, and A. M. Ardekani, "Hydrodynamic mechanisms of cell and particle trapping in microfluidics," *Biomicrofluidics*, vol. 7, no. 2, p. 021501, 2013.

[12] E. Blanco, H. Shen, and M. Ferrari, "Principles of nanoparticle design for overcoming biological barriers to drug delivery," *Nat. Biotechnol.*, vol. 33, no. 9, pp. 941–951, 2016.

[13] H. Başağaoğlu, S. Succ, D. Wyrick, and J. Blount, "Particle Shape Influences Settling and Sorting Behavior in Microfluidic Domains," *Sci. Rep.*, vol. 8, no. 1, p. 8583, 2018.

[14] D. Huh *et al.*, "Gravity-Driven Microfluidic Particle Sorting Device with Hydrodynamic Separation Amplification," *Anal. Chem.*, vol. 79, no. 4, pp. 1369–1376, 2007.

[15] N. O. Jaensson, M. A. Hulsen, and P. D. Anderson, "On the use of a diffuse-interface model for the simulation of rigid particles in two-phase Newtonian and viscoelastic fluids," *Comput. Fluids*, vol. 156, pp. 81–96, 2017.

[16] N. O. Jaensson, C. Mitrias, M. A. Hulsen, and P. D. Anderson, "Shear-Induced Migration of Rigid Particles near an Interface between a Newtonian and a Viscoelastic Fluid," *Langmuir*, vol. 34, no. 4, pp. 1795–1806, 2018.

[17] A. J. Capel, R. P. Rimington, M. P. Lewis, and S. D. R. Christie, "3D printing for chemical, pharmaceutical and biological applications," *Nat. Rev. Chem.*, vol. 2, pp. 422–436, 2018.

[18] M. Farina, J. F. Alexander, U. Thekkedath, and A. Grattoni, "Cell Encapsulation: Overcoming Barriers in Cell Transplantation in Diabetes and Beyond," *Adv. Drug Deliv. Rev.*, vol. 139, pp. 92–115, 2019.

[19] K. E. Samy, E. S. Levy, K. Phong, B. Demaree, A. R. Abate, and T. A. Desai, "Human intestinal spheroids cultured using Sacrificial Micromolding as a model system for studying drug transport," *Sci. Rep.*, vol. 9, no. 1, pp. 1–12, 2019.

[20] T. A. Desai and Q. Tang, "Islet encapsulation therapy — racing towards the finish line?," *Nat. Rev. Endocrinol.*, vol. 14, no. 11, pp. 630–632, 2018.

[21] C. L. Stabler, Y. Li, J. M. Stewart, and B. G. Keselowsky, "Engineering immunomodulatory biomaterials for type 1 diabetes," *Nat. Rev. Mater.*, vol. 4, pp. 429–450, 2019.

[22] A. E. Vlahos, N. Cober, and M. V Sefton, "Modular tissue engineering for the vascularization of subcutaneously transplanted pancreatic islets," *Proc. Natl. Acad. Sci.*, vol. 114, no. 35, pp. 9337–9342, 2017.

[23] W. Song *et al.*, "Engineering transferrable microvascular meshes for subcutaneous islet transplantation," *Nat. Commun.*, vol. 10, no. 1, pp. 1–12, 2019.

[24] A. E. Vlahos and M. V Sefton, "Muted fibrosis from protected islets," *Nat. Biomed. Eng.*, vol. 2, no. 11, pp. 791–792, 2018.

[25] Q. Liu *et al.*, "Developing mechanically robust , triazole-zwitterionic hydrogels to mitigate foreign body response (FBR) for islet encapsulation," *Biomaterials*, vol. 230, p. 119640, 2020.

[26] K. K. Papas, H. De Leon, T. M. Suszynski, and R. C. Johnson, "Oxygenation strategies for encapsulated islet and beta cell transplants," *Adv. Drug Deliv. Rev.*, vol. 139, pp. 139–156, 2019.

[27] A. E. Vlahos *et al.*, "Endothelialized collagen based pseudo-islets enables tuneable subcutaneous diabetes therapy," *Biomaterials*, p. 119710, 2020.

[28] A. A. Stock *et al.*, "Conformal Coating of Stem Cell-Derived Islets for b Cell Replacement in Type 1 Diabetes," *Stem Cell Reports*, vol. 14, pp. 1–14, 2020.

APPENDICES

Appendices

Appendix A

A.1 Estimation of the aspect ratio from microscopic images

We model the particles by determining the aspect ratio. Using MATLAB's image processing toolbox, the mean and the major axis of the particles is estimated from microscopic images. The images are retrieved from three publications in peer-reviewed journals [1-3] and one book chapter [4]. 57 islets are identified in total and the estimations regarding the aspect ratio are presented in Table A 1.

Table A 1 Image processing results

Islet	Max Diameter (μm)	Aspect ratio	Figure	Reference
1	190,07	1,17	4A	[1]
2	184,97	1,26	4B	[1]
3	105,71	1,86	4B	[1]
4	93,67	1,34	4B	[1]
5	92,09	1,10	4B	[1]
6	72,83	1,28	4B	[1]
7	65,90	1,36	4B	[1]
8	54,79	1,20	4B	[1]
9	49,79	1,10	4B	[1]
10	162,87	1,20	4C	[1]
11	98,01	1,54	4C	[1]
12	144,87	1,21	4D	[1]
13	94,26	1,25	4D	[1]
14	84,69	1,41	4D	[1]
15	67,99	1,80	4D	[1]
16	286,29	1,93	4E	[1]
17	90,89	1,09	4E	[1]
18	45,23	1,21	4E	[1]
19	36,22	1,28	4E	[1]
20	488,85	1,27	4F	[1]
21	183,07	1,18	1A	[2]
22	142,05	1,36	1A	[2]
23	105,65	1,38	1A	[2]

24	66,08	1,09	1A	[2]
25	251,25	1,48	1B	[2]
26	334,66	1,38	1C	[2]
27	75,90	1,22	1G	[2]
28	271,18	1,24	1H	[2]
29	488,85	1,61	1I	[2]
30	110,38	1,44	4G	[3]
31	203,37	1,47	1B	[4]
32	164,80	1,33	1B	[4]
33	156,92	1,24	1B	[4]
34	152,82	1,30	1B	[4]
35	141,11	1,24	1B	[4]
36	137,50	1,23	1B	[4]
37	131,39	1,13	1B	[4]
38	130,71	1,23	1B	[4]
39	130,54	1,32	1B	[4]
40	128,20	1,23	1B	[4]
41	122,73	1,50	1B	[4]
42	119,85	1,27	1B	[4]
43	118,16	1,50	1B	[4]
44	116,82	1,14	1B	[4]
45	110,77	1,10	1B	[4]
46	109,77	1,22	1B	[4]
47	109,42	1,17	1B	[4]
48	104,30	1,30	1B	[4]
49	100,99	1,19	1B	[4]
50	100,71	1,13	1B	[4]
51	93,57	1,09	1B	[4]
52	88,64	1,17	1B	[4]
53	88,52	1,36	1B	[4]
54	86,22	1,27	1B	[4]
55	78,88	1,11	1B	[4]
56	77,67	1,08	1B	[4]
57	77,10	1,20	1B	[4]

A.2 The effect of density ratio

Figure A 1 shows the trajectory and the orientation of two disks (α=1.00) with different densities released from two different initial positions. The sample-to-sheath-flow rate ratio is equal to 4. According to the results, the impact of the density ratio on the final position depends on the initial distance of the particle surface from the wall. Two disks with different

densities are released at different positions, with distance equal with $a/2$, will identically move and reach the outlet in the same way. However, if the initial distance is equal to $a/12$, the lighter particle will move closer to the axis. We assume that this behavior is due to gravity forces. Regardless of initial position, the density effect on the orientation of the disk is equally significant in both cases and the mode of rotation does not reverse. We conclude that the density ratio of range 1.059≤λ≤1250 has moderate effect on particle motion.

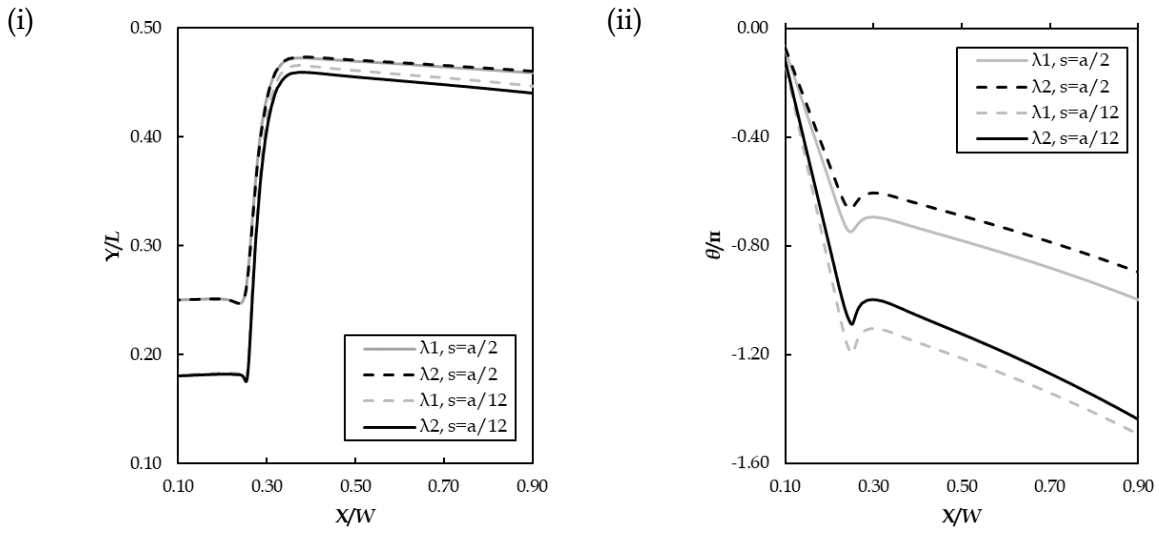

Figure A 1 The density effect on (i) the trajectory and (ii) the orientation of a circular particle released from two different positions. In all cases k=4.

A.3 Mesh independent study

The governing equations are solved by implementing the Finite Element (FE) formalism on a triangular mesh T_h, where h_{mesh} is the typical mesh size. Mesh refinement is performed mainly in regions in the vicinity of the particle and/or where solid surfaces approach each other. In order to obtain an accurate solution in a reasonable time, a convergence and mesh-independence test is made through preliminary numerical tests. By decreasing the mesh size until the solutions for two consecutive mesh sizes show no divergence, we ensure that the solution is independent of mesh size. Figure A 2 presents the results of the mesh independent study. Four meshes are tested. Finally, the maximum and minimum grid sizes are chosen to be a/3 and a/24, respectively.

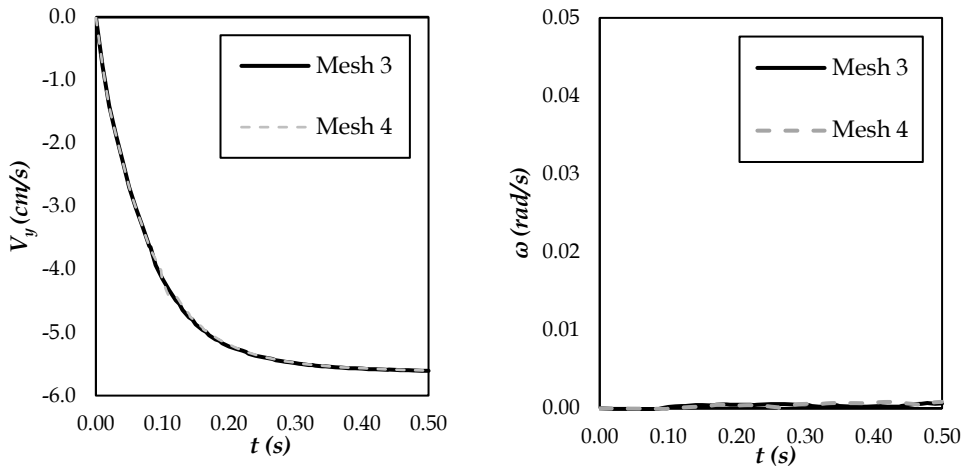

Figure A 2 The mesh independent study. The domain and the parameters are the same as in [5].

A.4 Configuration of multiple particles

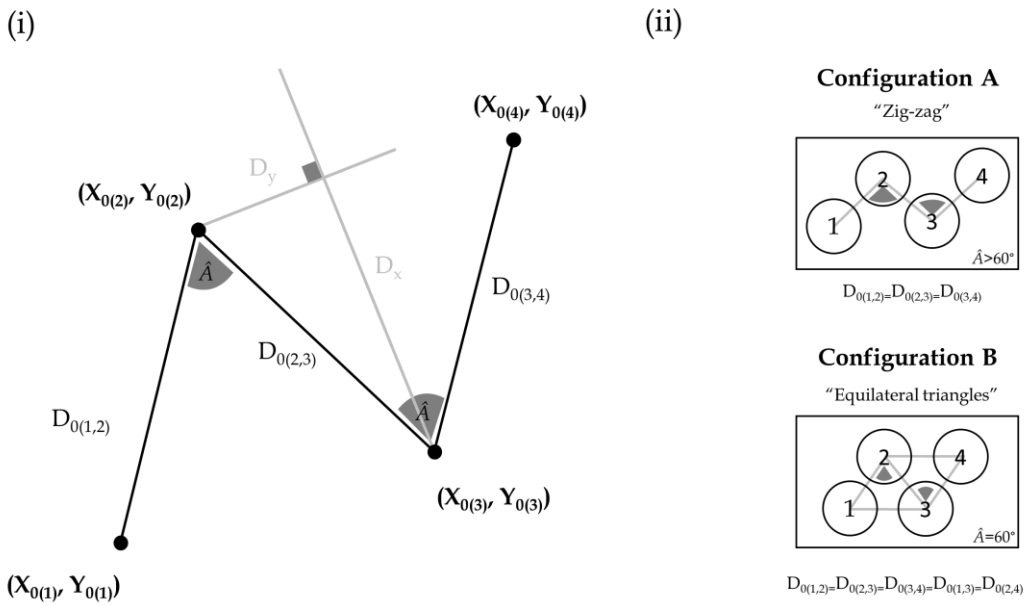

Figure A 3 (i)The configuration of four disks and the initial distance of the centers (ii) Schematic explanation of the two configurations used in this study.

Figure A 3 shows the configuration of four particles and the initial distance of the centers. The initial distance between the centers of the neighboring disks is denoted as $D_{0(i,\, i+1)}$. We model

the density of the sample fluid, i.e., number of islets per fluid volume, by spacing the particles in two configurations. Configuration A and B correspond respectively to lower and higher density. Figure A 3 (ii) shows the two configurations used in the present work. By decreasing angle Â, the particles come closer and the density of the sample fluid increases. In configuration A, the initial distance of the centers of the neighboring particles are equal, i.e., $D_{0(1,\ 2)} = D_{0(2,\ 3)} = D_{0(3,\ 4)}$. In configuration B, the particles (1-3) and (2,4) are equally spaced as well, i.e., $D_{0(1,\ 2)} = D_{0(2,\ 3)} = D_{0(3,\ 4)} = D_{0(1,\ 3)} = D_{0(2,\ 4)}$.

In configuration A, the disks are released at

$$(X_{0(1)}, Y_{0(1))=} (2W\text{-}3Dx/2\ ,W/2\text{-}\ Dy/2),$$

$$(X_{0(2)}, Y_{0(2)})=(2W\text{-}\ Dx/2, W/2+\ Dy/2),$$

$$(X_{0(3)}, Y_{0(3)})=(2W+\ Dx/2, W/2\text{-}\ Dy/2),$$

$$(X_{0(4)}, Y_{0(4)})=(2W+\ 3Dx/2, W/2+\ Dy/2),$$

where $Dx = (D_{0(i,\ i+1)}{}^2\text{-}Dy^2)^{1/2}$ and $Dy=4a/3$.

In configuration B, the disks are released at

$$(X_{0(1)}, Y_{0(1))=} (W/2+Dx/2, 2W\text{-}Dy/2),$$

$$(X_{0(2)}, Y_{0(2)})=(W/2\text{-}Dx/2, 2W\text{-}Dy/2),$$

$$(X_{0(3)}, Y_{0(3)})=(W/2\text{-}\sqrt{3}Dy/2, 2W+\sqrt{3}Dx/2),$$

$$(X_{0(4)}, Y_{0(4)})=(W/2+\sqrt{3}Dy/2, 2W\text{-}\sqrt{3}Dx/2),$$

where $Dx = (D_{0(i,\ i+1)}{}^2\text{-}Dy^2)^{1/2}$ and $Dy=2a/5$.

Appendix B

B.1 Printing parameters

The plastic parts of the pumps and the setup were printed with an Ender 5 FDM-printer (Creality 3D Technology Co. Ltd, China). The printer was equipped with a 0.4 mm nozzle. Simplify3D was employed as a slicer software. The interior fill percentage was 20% for the pumps and 100% for the slider and the platform. The most important parameters are presented in Table B 1.

Table B 1 FDM-Printing Parameters

Parameter	Value
Extrusion multiplier	1
Retraction distance	6.5 mm
Primary layer height	0.3 mm
Outline shells	2
First layer speed	30%
Outline overlap	30%
Infill percentage	20% or 100%
Infill angle	45 deg
Support infill	15%
Extruder temperature	210 °C
Build table temperature	70 °C
Fan speed	60%
Printing speed	40 mm/s
Outline under-speed	90%

References

[1] R. Lehmann et al., "Superiority of Small Islets in Human Islet Transplantation," Diabetes, vol. 56, pp. 594–603, 2007.

[2] D. Bosco et al., "Unique Arrangement of α- and β-Cells in Human Islets of Langerhans," Diabetes, vol. 59, no. 5, pp. 1202–1210, 2010.

[3] C. Dai, M. Brissova, Y. Hang, and C. Thompson, "Islet-enriched gene expression and glucose-induced insulin secretion in human and mouse islets," Diabetologia, vol. 55, no. 3, pp. 707–718, 2012.

[4] R. S. Heller, "The comparative anatomy of islets," in Islets of Langerhans, 2013, pp. 1–16.

[5] R. Glowinski, T. W. Pan, T. I. Hesla, and D. D. Joseph, "A Fictitious Domain Approach to the Direct Numerical Simulation of Incompressible Viscous Flow past Moving Rigid Bodies: Application to Particulate Flow," *J. Comput. Phys.*, vol. 426, pp. 363–426, 2001.